INVESTIGATIONS OF BOUNDARY-LAYER TRANSITION AND AIRLOADS ON ROTATING BLADES

Von der Fakultät für Maschinenbau
der Gottfried Wilhelm Leibniz Universität Hannover
zur Erlangung des akademischen Grades
Doktor-Ingenieur
genehmigte Dissertation

von
Armin Weiss, M.Sc.

2018

1. Referent: Prof. Dr.-Ing. Markus Raffel
2. Referent: Prof. Dr.-Ing. Christoph Brücker

Tag der Promotion: 20. August 2018

Preface

The presented work is a result of a four year employment (06/2014 - 06/2018) as research associate in the *Experimental Methods* department at the *Institute of Aerodynamics and Flow Technology* of the *German Aerospace Center (DLR)* in Göttingen and has been conducted in the framework of an *Airbus*-funded partnership. The content of this thesis has been established in close collaboration with the *Helicopter* department of the same institute at the *DLR* in Göttingen.

The presented material has not been submitted, either in whole or in part, for a degree at any university. Parts of the presented work, including text and illustrations, have been published in both reviewed and unreviewed literature, as indicated at the beginning of the respective chapters.

A full list of my scientific contributions can be found after the bibliography. The relevant publications for this thesis are:

1. A. Weiss, R. Geisler, T. Schwermer, D. Yorita, U. Henne, C. Klein, and M. Raffel. Single-shot pressure-sensitive paint lifetime measurements on fast rotating blades using an optimized double-shutter technique. *Experiments in Fluids*, 58(9):120–140, August 2017. doi: 10.1007/s00348-017-2400-4.

2. A. Weiss, A. D. Gardner, C. Klein, and M. Raffel. Boundary-layer transition measurements on Mach-scaled helicopter rotor blades in climb. *CEAS Aeronautical Journal*, 8(4):613–623, December 2017. doi: 10.1007/s13272-017-0263-2.

3. A. Weiss, A. D. Gardner, T. Schwermer, C. Klein, and M. Raffel. On the effect of rotational forces on rotor blade boundary-layer transition. In *2018 AIAA Aerospace Sciences Meeting*, number AIAA 2018-0309, Kissimmee, FL, USA, January 8-12 2018. doi: 10.2514/6.2018-0309, submitted to *AIAA Journal*.

For each of the papers presented in this thesis, I was the primary author. This involved the planning, design, management and execution of the experiments, and the completion of all of the computations presented in this work, as well as the analysis of the experimental and numerical data and writing of each of the papers presented.

Abstract

In this thesis airloads and boundary-layer transition were investigated on a Mach-scaled helicopter rotor blade configuration in climb. Surface pressures and boundary-layer transition positions were measured on the suction side of the outer 60 % of the DSA-9A equipped rotor blades by means of advanced optical measurement techniques providing data at high spatial resolution. The experiments were conducted in the rotor test facility of the DLR Göttingen (RTG) and were complemented by pressure tap measurements on blade sections at two different radii as well as by integral thrust measurements. The investigated parameter range comprises extensive variations of the collective root pitch angle at three different rotating speeds spanning tip chord Reynolds and Mach numbers of $Re_\text{tip} = 4.6 - 9.3 \times 10^5$ and $M_\text{tip} = 0.29 - 0.57$, respectively.

An optimized pressure-sensitive paint (PSP) system for global surface pressure measurements on fast rotating blades is presented. It comprises an optimized image acquisition technique and allows omitting error-prone post-processing routines or laborious setups to eliminate artifacts originating from rotational image blur. The PSP system was successfully applied to the investigated configuration. A comparison between ensemble averaged PSP data and fast-response pressure tap readings on the same blade reveals a RMS level of residual deltas of ~250 Pa. Application of the single-shot PSP lifetime technique allowed the identification of stall related and spatially confined flow regions on the blade, comprising increased low-frequency pressure fluctuations, thus proving the capability to measure instationary phenomena. PSP results further reveal flow features such as the footprint of the tip vortex, the suction peak parallel to the leading edge and also a chordwise pressure discontinuity indicative of laminar-turbulent boundary-layer transition. The latter was confirmed by the results of the separately conducted transition experiment and underlined the ability of the optimized PSP system to capture spatial gradients in a precise manner.

Boundary-layer transition was measured by means of temperature-sensitive paint (TSP) and for comparison also via infrared thermography. Transition positions were detected for all data points and for various radial locations at a precision of better than 1 % chord (i.e. $\approx 0.7\,\text{mm}$). A data base was established, which is complemented by corresponding pressure tap readings as well as integral thrust measurements, and ready to use for validation purposes of numerical codes. The effect of rotational forces on boundary-layer transition was specifically analyzed at resulting Reynolds and Mach numbers of $Re_\text{res} = 3.74 \times 10^5$ and $M_\text{res} = 0.22$ under exclusive variation of the contribution of rotational forces, expressed by the variation of Rossby number between the two values $Ro = 6.95$ and $Ro = 4.76$. A hypothesized stabilizing effect of rotational forces on boundary-layer transition appears to be insignificant for the investigated configuration. Measured surface pressures at 77 % span are compared to solutions of a coupled two-dimensional (2D) Euler/ boundary-layer solver and numerical results are used to obtain transition N-factors, based on two different approaches to the e^N-method. Calculated pressures agree with experimental data to within a difference of $\Delta c_p \approx 0.02$. Employing 2D local compressible linear stability theory (LST) and considering measured non-adiabatic wall temperatures, transition N-factors are correlated in the range of $N_\text{cr} = 8.4 \pm 0.5$, independent of Reynolds number based on rotating speed. The findings translate to a prediction capability of the transition position of better than ± 5 % of the chord assuming that the pressure distribution or effective angle of attack is known.

Kurzfassung

Untersuchungen von Grenzschichttransition und Luftkräften an rotierenden Blättern

In der vorliegenden Arbeit wurden Luftkräfte und Grenzschichttransitionslagen auf Mach-skalierten Hubschrauberrotorblättern in Steigflugkonfiguration untersucht. Oberflächendrücke und laminar-turbulente Umschlagslagen wurden auf den äußeren $60\,\%$ der Saugseite eines mit einem DSA-9A Profil ausgestatteten Rotorblattes gemessen. Hierfür wurden örtlich hochauflösende optische Messtechniken eingesetzt und durch integrale Schub- sowie Oberflächendruckmessungen mittels einzelnen Druckanbohrungen ergänzt. Die Experimente wurden am Zweiblattrotor der Rotor-Testanlage des DLR in Göttingen (RTG) durchgeführt. Der untersuchte Parameterraum umfasst eine Variation des kollektiven Blattanstellwinkels bei jeweils drei unterschiedlichen Drehzahlen. Die auf die Blattspitzengeschwindigkeit und die Sehnenlänge bezogenen Mach- und Reynoldszahlen ergeben sich zu $M_{\text{tip}} = 0.29 - 0.57$ und $Re_{\text{tip}} = 4.6 - 9.3 \times 10^5$.

Es wird ein für den Einsatz an schnell drehenden Rotorblättern optimiertes *pressure-sensitive paint* (PSP) Messsystem vorgestellt. Eine hierfür optimierte Bilderfassung verhindert Messartefakte, die durch Bildunschärfe infolge von Rotation entstehen. Das System wurde erfolgreich an der untersuchten Konfiguration angewendet. Ein Vergleich zwischen PSP-Ergebnissen und Daten herkömmlicher Drucksensoren ergibt einen Effektivwert der Unterschiede von ca. $250\,\text{Pa}$. Durch die Verwendung der *single-shot lifetime* PSP-Methode konnten Bereiche partieller Strömungs-ablösung auf dem Blatt identifiziert werden, in denen vergleichsweise hohe niederfrequente Druckschwankungen gemessen wurden. Die PSP-Resultate offenbaren charakteristische Strukturen, wie den "Fußabdruck" des Randwirbels, die Saugspitze parallel zur Blattvorderkante oder gar den abrupten Druckanstieg als Folge des laminar-turbulenten Grenzschichtumschlags. Der letztgenannte Zusammenhang konnte durch die separaten Transitionsmessungen verifiziert werden und unterstreicht die Fähigkeit des Messsystems, räumliche Gradienten präzise zu erfassen.

Grenzschichttransition wurde mittels *temperature-sensitive paint* (TSP) und vergleichsweise via Infrarot-Thermografie gemessen. Die Umschlagslagen wurden für alle Datenpunkte entlang der Blattspannweite über eine Auswertesystematik und mit einer Präzision von ca. $1\,\%$ der Sehnenlänge ($\approx 0.7\,\text{mm}$) ermittelt. Zusammen mit integralen Schubwerten und Druckanbohrungsergebnissen wurde eine Datenbasis erstellt, die für die Validierung von numerischen Methoden zur Verfügung steht. Der Einfluss rotierender Kräfte auf den Grenzschichtumschlag wurde durch einen Vergleich der Transitionslagen bei gleichem effektiven Anstellwinkel, resultierenden Reynolds- und Machzahlen von $Re_{\text{res}} = 3.74 \times 10^5$ und $M_{\text{res}} = 0.22$ und ausschließlich unter Variation der Rossbyzahl Ro, als Maß für Rotationskräfte, untersucht. Ein stabilisierender Effekt von Rotations-kräften wurde bei Variation von $Ro = 6.95$ auf $Ro = 4.76$ für die untersuchte Konfiguration nicht festgestellt. Druckmessdaten bei $77\,\%$ des Blattradius wurden mit Lösungen eines gekoppelten zweidimensionalen (2D) Euler-/ Grenzschichtlösers verglichen und verwendet, um kritische N-faktoren auf Basis unterschiedlicher Versionen der e^N-Methode zu bestimmen. Berechnete und gemessene Oberflächendrücke stimmen innerhalb von $\Delta c_p \approx 0.02$ überein. Auf Basis von 2D lokaler kompressibler linearer Stabilitätstheorie und unter Berücksichtigung der gemessenen nicht-adiabaten Wandtemperatur wurden kritische N-faktoren von $N_{\text{cr}} = 8.4 \pm 0.5$ ermittelt, die keine signifikante Abhängigkeit der Reynolds- bzw. Drehzahl zeigen. Demnach kann bei Kenntnis der Druckverteilung die Transitionslage bis auf $\pm 5\,\%$ der Sehnenlänge vorhergesagt werden.

Stichwörter: Rotorblätter, druck-/ temperaturempfindliche Beschichtung (PSP / TSP), Grenz-schichttransition, Rotationseffekt, e^{N}-Methode

Acknowledgments

Contents

List of figures

List of tables

Nomenclature

Latin symbols

a	Polynomial coefficient
A	Amplitude of Tollmien-Schlichting waves
A_{blades}	Blade planform area, $A_{\text{blades}} = c \cdot R$
c	Chord length, c = 0.072 m
c_f	Skin friction coefficient, $c_f = \tau_w / \left(0.5\rho_\infty u_{\text{res}}^2\right)$
c_p	Pressure coefficient, $c_p = (p_x - p_\infty) / \left(0.5\rho_\infty u_{\text{res}}^2\right)$
$\Delta c_{p,\text{RMS}}$	Effective difference between pressure transducer readings and calculations
C_T/σ	Blade loading coefficient, $C_T/\sigma = F_{\text{thrust}} / \left[\rho_\infty A_{\text{blades}}(2\pi f_{\text{rotor}}R)^2\right]$
$\frac{\text{D}}{\text{D}t}$	Total differential operator , $\frac{\text{D}}{\text{D}t} = \frac{\delta}{\delta t} + \vec{u}\nabla$
e	Euler number, $e = 2.718...$
f_{acq}	Data acquisition frequency, (double) frames per second
f_{rotor}	Rotation rate of the rotor, Hz
f_{TS}	Tollmien-Schlichting frequency, Hz
F_{thrust}	Thrust force, N
$G1$	First time interval for integration of luminescent light ("gate 1"), s
$G2$	Second time interval for integration of luminescent light ("gate 2"), s
h	Specific enthalpy, J/(kg K)
H_{12}	Boundary-layer shape factor, $H_{12} = \delta_1/\delta_2$
$H_{12,\text{MSES}}$	Compressible shape factor, from MSES at calculated $(x/c)_{\text{tr,onset}}$
$H_{12i,\text{COCO}}$	Incompressible shape factor, from COCO at measured $(x/c)_{\text{tr,onset}}$
i	Imaginary unit, $\sqrt{-1}$
I	Luminescence intensity, counts
J	Advance ratio, $J = u_\infty / (2\pi f_{\text{rotor}}R)$
$\tilde{J}$	Advance ratio, $\tilde{J} = u_\infty / (2\pi f_{\text{rotor}}\tilde{r})$
k	Thermal conductivity, W/(m K)
$\tilde{l}$	Characteristic length, m
M	Mach number based on u_{res}
n_{sensors}	Number of pressure sensors
N	Natural logarithm of integral growth rate
N_{cr}	(Critical) transition N-factor
p	Pressure, Pa
q	Generalized flow variable, can be u, v, p, T or ρ
r	Radial coordinate, m

$\tilde{r}$	Radius for investigation of rotational effect, m
$r(Pr)$	Recovery factor as a function of Prandtl number Pr
R	Tip radius of rotor blade, $R = 0.65\,\mathrm{m}$
R_{air}	Specific gas constant for air, J/(kg K)
R_{z}	Mean roughness depth, μm
Re	Reynolds number (based on c and u_{res} if not otherwise noted)
Ro	Rossby number, $Ro = (\tilde{J}^2 + 1) \cdot (\tilde{r}/c)$
RoR	Ratio of ratios, signal expressing pressure and/or temperature
s_P	Pressure sensitivity, %/100 kPa
s_T	Temperature sensitivity, %/K
St	Stanton number, $St = \dfrac{\eta}{\rho_\infty \kappa_P u_\infty}$
t	Time, s
$\Delta t_{\mathrm{G1} \to \mathrm{laser}}$	Time delay between end of $G1$ and start of laser pulse, s
T	Temperature, K
Tu	Turbulence intensity, %
u, v, w	Velocity components in streamwise, wall-normal and radial direction, m/s
$\vec{u}$	Velocity vector, $\vec{u} = [u, v, w]$
x, y	Stream- or chordwise and wall-normal coordinate, m
v_∞	Axial inflow velocity, m/s

Greek symbols

α	(Effective) angle of attack, °; complex wave number in streamwise direction
α_{I}	Disturbance growth rate
β_{root}	Collective pitch at blade root (at $r = 0.125\,\mathrm{m}$), °
γ	Ratio of specific heats
δ	Boundary-layer thickness, m
δ_1	Boundary-layer displacement thickness, m, $\delta_1(x) = \int_0^\infty \left(1 - \dfrac{\rho u}{\rho_e u_e}\right) dy$
δ_2	Boundary-layer momentum thickness, m, $\delta_2(x) = \int_0^\infty \left[\dfrac{\rho u}{\rho_e u_e}\left(1 - \dfrac{u}{u_e}\right)\right] dy$
Δ	Difference or increment
Δ_{offset}	Mean (corrected) difference between pressure transducers and PSP data
η	Heat transfer coefficient, W/(m^2 K)
λ	Wavelength, nm
μ	Dynamic viscosity, kg/(m s)
ν	Kinematic viscosity, m^2/s
κ_P	Specific heat capacity at constant pressure, J/(kg K)
ρ	Density, kg/m^3
σ	Standard deviation or solidity
$\tau_{0.1 I_{\mathrm{max}}}$	Luminescent lifetime until 10 % of maximum emitted light intensity is reached
τ_{w}	Wall shear-stress, Pa
Φ	Angle between axes of rotor and rotating mirror, °
ψ	Propagation angle of disturbances with respect to potential streamline, °

ψ_p Inclination of potential stream line with respect to tangential direction, $^\circ$
ω Complex angular frequency of Tollmien-Schlichting waves
ω_R Real angular frequency of Tollmien-Schlichting waves, Hz
Ω Angular frequency, $\Omega = 2\pi f$

Subscripts

0	Referring to indifference point
0.53 R	Quantity at $r = 0.53\,R$
0.77 R	Quantity at $r = 0.77\,R$
aw	Adiabatic condition at wall
best	Best fit of simulation to experiment
cr	Critical or threshold value for N leading to transition
e	Boundary-layer edge
end	Transition end position
em	Emission
ex	Excitation
exp	Quantity obtained from experiment
i	Counter
k	Counter
Ku−on	Pressure transducers (Kulites) switched on
Ku−off	Pressure transducers (Kulites) switched off
max	Maximum value
MSES	Quantity from MSES computation
onset	Transition onset position
ref	(Adiabatic) reference condition
res	(Based on) resulting velocity $u_{\text{res}} = \sqrt{u_\infty^2 + (2\pi r f_{\text{rotor}})^2}$
RMS	Root of the mean squared value
tip	Blade tip at $r = R$
tr	Transition position
tr,end	Transition end position
tr,onset	Transition onset position
TSP	Quantity from TSP measurement
w	Condition at the wall or non-adiabatic, heated wall
wind-off	Conditions with rotor at rest
wind-on	Desired rotor condition
x	Based on chordwise coordinate
∞	(Axial) inflow condition

Superscripts

$^-$	Mean value or ensemble averaged quantity

$'$	Fluctuating component
$\rightarrow$	Vector
$\sim$	Characteristic quantity
$\hat{}$	Amplitude

Abbreviations

2D	Two-dimensional
3D	Three-dimensional
A/D	Analog to digital
CCD	Charge-coupled device
CFD	Computational fluid dynamics
CMOS	Complementary metal-oxide semiconductors
COCO	Name of boundary-layer equation solver
DLR	Deutsches Zentrum für Luft- und Raumfahrt
DNS	Direct numerical simulation
DSA-9A	Name of airfoil on investigated rotor blades
FOX	Framing-optimized exposure
fps	(Double) frames per second
IR	Infrared thermography
LILO	Name of boundary-layer stability analysis tool
LED	Light emitting diode
LSB	Laminar separation bubble
LST	Linear stability theory
MSES	Name of 2D coupled Euler-/ boundary-layer equation solver
Nd:YAG	Neodymium-doped yttrium-aluminium-garnet
ONERA	Office National d'Études et de Recherches Aérospatiales
PIV	Particle image velocimetry
PMT	Photo-multiplier tube
poly(4-TBS)	Poly-(4-tert-butyl-styrene)
PSP	Pressure-sensitive paint
PtTFPP	Platinum tetra(pentafluorophenyl) porphyrin
PU	Poly urethane
rev	Revolutions
RMS	Root of the mean squared value
rpm	Rotations per minute
RTG	Rotor test facility of DLR Göttingen
Ru(phen)	Ruthenium phenanthroline
SNR	Signal to noise ratio
TS	Tollmien-Schlichting (wave)
TSP	Temperature-sensitive paint
∇	Gradient operator, $\nabla = \left[\frac{\delta}{\delta x} \; \frac{\delta}{\delta y} \; \frac{\delta}{\delta r} \right]$

1 Introduction

Aerodynamic measurements on rotating blades are vital in order to understand inherent flow phenomena, for the characterization of aerodynamic loads and performance data and due to their inevitable use for the validation of computational fluid dynamics (CFD) codes used for prediction purposes. In this regard, the surface pressure distribution and laminar-turbulent boundary-layer transition are of special interest. Usually, benchmark experiments in rotorcraft research used for CFD validation either provide integral balance data exclusively [6] or employ sensors at only discrete pointwise locations, for instance wall tappings for surface pressure measurements [89, 154] or heat flux sensors for the characterization of the boundary layer [140]. Pressure or heat flux transducers installed in rotating blades introduce heavy centrifugal loads. The need to transfer data outside the rotating frame demands a costly telemetric solution. Due to limited space for the installation of sensors, the spatial resolution is usually quite scarce and characteristic flow features such as the suction peak, the footprints of the tip vortex or boundary-layer transition can hardly be resolved, which complicates numerical validation [169]. Hence, optical measurement techniques like pressure-sensitive paint (PSP) or temperature-sensitive paint (TSP) and infrared thermography (IR) are powerful techniques, as they non-intrusively provide global information on surface pressure and on the boundary layer at high spatial resolution.

Boundary-layer transition has significant impact on the aerodynamics of helicopter main rotors. For laminar boundary layers generate less friction drag than turbulent boundary layers, increased amounts of laminar flow reduce the power required by the rotor and enhance its efficiency. Therefore, knowledge of the boundary-layer transition position is an important parameter in the design phase of modern rotor blades. Because the extent of laminar flow is in principle larger at smaller Reynolds numbers [136], the phenomenon needs to be understood especially when performing tests at model scale ($Re < 10^6$) to eventually overcome issues when scaling to full scale [8]. For instance, recent experimental and numerical analyses showed significant effect of laminar flow on the performance of a Mach-scaled helicopter rotor in hover. A comparison between the rotor efficiency of fully-turbulent and free-transition cases revealed differences in the range of 6 - 10 % with higher discrepancies at low thrust levels [105, 106]. However, accurate numerical prediction of the aerodynamic performance of a helicopter rotor remains a challenging task, also for axisymmetric flow conditions as hover or climbing flight. To date, modeling of boundary-layer transition on helicopter rotor blades is based either on empirical correlations from studies on purely translating wings or on theories employing solely two-dimensional flow assumptions. In this respect, the effects of rotational forces are ignored, although it is known that rotational effects on boundary-layer flows around rotating blades in principal exist. A common problem with previous studies on boundary-layer transition on helicopter rotor blades is the lack of experimental transition data for validation purposes of advanced numerical tools, including transition prediction.

1.1 Surface pressure measurements on fast rotating blades using pressure-sensitive paint (PSP)

1.1.1 PSP principles

The PSP technique relies on photo-kinetic interactions between the airflow and a luminescent coating applied to the surface of interest. A detailed description and application examples of the technique are described by Vollan and Alati [158], Engler et al. [33] and Klein [68]. Being excited by light of a certain wavelength, the luminescent dye molecules emit light at a longer wavelength. This radiative process can be quenched by oxygen, depending on the local air pressure [67]. For instance, higher local pressures reduce both the amount of light emitted and the luminescent lifetime decay time. The emitted light does not only depend on pressure. In this regard, possible sources of uncertainty include spatially inhomogeneous excitation light and dye concentration as well as thermal quenching of luminescence and photo degradation of the dye [85]. The luminescence is usually captured by a scientific grade camera using optical filters to separate the emitted signal from the excitation light. Using the "gated intensity ratio method" [85], also referred to as the "lifetime method", the lifetime is measured as a function of the ratio of two images I_{G1}/I_{G2}. As sketched in Fig. 1.1 they are subsequently recorded during the integration "gates" $G1$ and $G2$. If
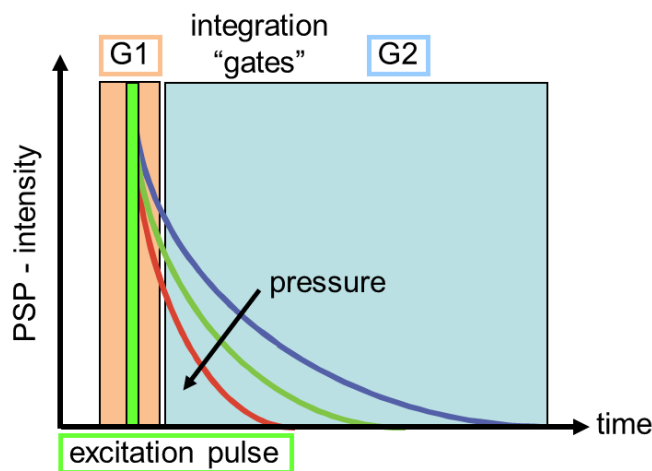
Figure 1.1: Schematic of PSP lifetime method with pulsed excitation.

both frames are acquired from a single excitation pulse, the method is referred to as the "single-shot lifetime technique" [50, 63]. With this approach any uncertainty originating from inhomogeneous or unstable pulsed excitation light is eliminated as the resulting pattern is the same in both images used for division. However, a residual spatial non-uniformity in the lifetime distribution persists also at uniform pressure [126, 171]. This in turn is accounted for by dividing the gated intensity ratio at any pressure p and temperature T ("wind-on" condition) by the ratio under known reference (ref) conditions, also referred to as "wind-off" conditions. The resulting "ratio of ratios" (RoR)

can then be related to pressure, for instance by

$$RoR = \frac{\frac{I_{G1}}{I_{G2}}}{\frac{I_{G1}}{I_{G2}\,\text{ref}}} = \frac{\frac{I_{G1}}{I_{G2}\,\text{wind-on}}}{\frac{I_{G1}}{I_{G2}\,\text{wind-off}}} = \sum_{i,k=0}^{m,n=2} a_{ik} \left(\frac{T}{T_{\text{ref}}}\right)^i \left(\frac{p}{p_{\text{ref}}}\right)^k \tag{1.1}$$

where $a_{i,k}$ are calibration coefficients to be obtained.

1.1.2 PSP on rotating blades

A particular challenge related to PSP measurements on fast rotating blades is to capture sharp images at sufficient signal-to-noise ratio (SNR). A common approach is to accumulate up to several hundreds of phase-locked exposures on the image sensor using a pulsed excitation synced to the rotation speed of the investigated blade. This phase-averaging technique has previously been applied to measure surface pressure on blades of a scaled model fan [11], a turbocharger compressor [49], a turbine rotor [148] or on fast rotating propellers [70]. The technique provides reproducible results if the position of the rotating blade in the image and the excitation pulses are perfectly stable. However, Wong et al. [165, 166] for instance reported significant smear in result images, due to cycle-to-cycle lead-lag and flapping motion when testing helicopter rotor blades being susceptible to aero-elastic effects. Moreover, if pressure fluctuations are of interest the phase-averaging accumulation technique is inherently limited to capture transient phenomena occurring in phase with the rotating frequency. The problem of image blur due to phase-locked accumulation of several exposures is illustrated in Fig. 1.2. Both images show the blade tip of a model helicopter rotor blade of 1.7 m radius and at a tip speed of $\approx 200\,\text{m/s}$. The image on the left comprises significant blur. It was accumulated from approximately 750 blade revolutions using pulsed LED excitation. In contrast, the sharp image on the right is acquired from a single excitation pulse of 5 ns duration using laser light.

These limitations are overcome by using the single-shot lifetime technique as employed by Juliano et al. [63], where both gated intensities are acquired from a single excitation pulse. To get sufficient signal, a high energy light source, for instance a laser, is required for PSP excitation. Due to its self-referencing character, the single-shot lifetime technique is insensitive to errors originating from model movement within inhomogeneous illumination as laser speckles, for instance. Disotell et al. [21] applied the method for unsteady PSP measurements on a small-scale fully articulated helicopter blade in forward flight. They employed a fast responding PSP and took advantage of the single-shot technique to resolve unsteady pressure footprints of flow structures on the blade. Most recently, Peng et al. [113] presented a successful application of the single-shot lifetime technique to real turbomachinery experiments. They obtained surface pressure results on turbocharger compressor blades with rotation speeds up to 150,000 rpm. The technique has also recently matured to be used on the entire upper surface of large-scale helicopter blades (with ~1.7 m blade radius) in forward flight condition [162]. A sample result out of the study from Watkins et al. [162] on the "PSP rotor" is shown in Fig. 1.3. The pressure topology on the suction side of the blade is depicted in part a) of the figure. Rotation is counter-clockwise. The main flow features which can be distinguished are increased suction areas (in blue) close to the leading edge, followed by a pressure increase further downstream. PSP data is compared to pressure transducer readings on the right hand side. The
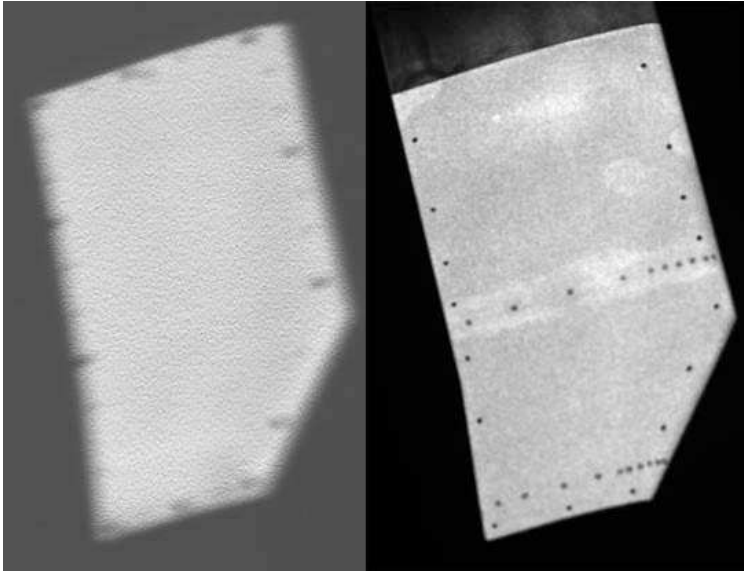
Figure 1.2: Demonstration of image blur due to phase-locked accumulation of several exposures to an image (from Wong et al. [167]).

shaded area denotes the standard deviation from a series of 15 PSP measurements and is mostly $\pm 10\,\text{kPa} - 15\,\text{kPa}$ wide. Deviations between pressure transducers and PSP data are reported to be in the order of 1 % with maximum deviations of about 10 %. In this case an error of 1 % corresponds to approximately 850 Pa.

So far, charge-coupled device (CCD) image sensors are used for single-shot lifetime measurements. As known from particle-image velocimetry (PIV) applications, the use of interline transfer CCD sensors enables the acquisition of two images in fast succession. The corresponding image readout scheme is also known as "double shutter" mode. However, in state-of-the art scientific grade CCD cameras the second exposure is several milliseconds long. The resulting image is therefore susceptible to blur due to the captured luminescence being emitted by the moving blade. In this case, the extent of blur depends on the rotating speed of the blade and the lifetime of the dye employed. Juliano et al. [63] used a sensor with a limited lifetime to reduce blur yet compromised signal intensity and the principal ability for applications on non-axisymmetric flows [64], where fast responding paints (see [52]) are preferred. It is obvious that any blur of this kind leads to a faulty recovered pressure signal. Gregory et al. [51] demonstrated the resulting bias due to image blur in the second exposure in a principle experiment, where a PSP signal was measured on a rotating-disc section. In Fig. 1.4a the result is illustrated in terms of ratio of ratios RoR which expresses levels of pressure and temperature (see Eq. 1.1). The blurred pattern is clearly visible in the bright areas in the vicinity of the black dot markers and at the trailing edge of the coated section. Although the pressure is expected to be constant along a disc section of constant radius, denoted by "S" in Fig. 1.4b , the resulting under- and overestimation of pressure at the blade leading- and trailing edges are clearly distinguishable in Fig. 1.4c.
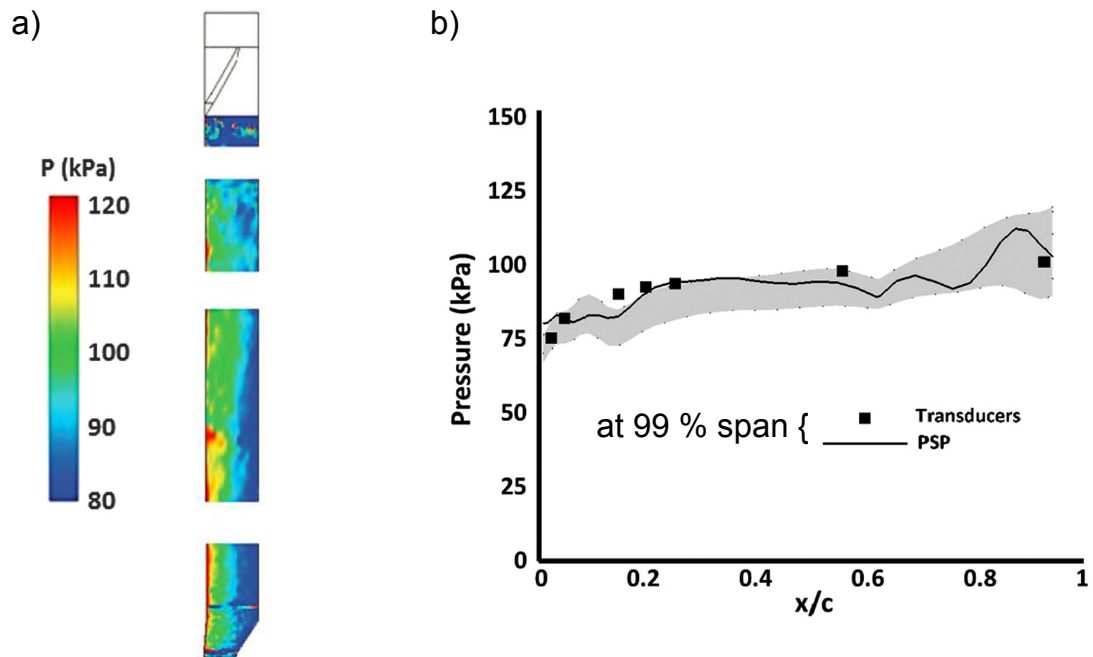
Figure 1.3: *a)* Surface-pressure result of the "PSP rotor" obtained using the single-shot lifetime technique *b)* Comparison between PSP data and pressure-transducer measurements (both figures are from [162]).

1.1.3 Blur elimination techniques

Up to now, two principles exist countering the problem of rotational image blur in aerodynamic testing. On the one hand, Juliano et al. [64] presented an image de-blurring algorithm, which was further developed by Gregory et al. [51]. The effect of the algorithm is illustrated in Fig. 1.4b and Fig. 1.4c. The post-processing routine employs a spatially invariant point spread function based on the rotation rate of the blade and the luminescent lifetime of the PSP. Because the latter depends on the pressures to be solved for, the method biases regions exhibiting large pressure gradients. Moreover, the routine amplifies noise inherent to the raw images (see Fig. 1.4c) for how the noise propagates to the resulting *RoR*) and it additionally introduces artificial ringing patterns (*Gibbs ringing*, see Fig. 1.5) in regions with sharp contrast levels debasing the quality of the final results especially near the blade trailing edge [51, 162].

On the other hand, Raffel and Heineck [117] demonstrated a technique to mechanically de-rotate images using a rotating mirror setup for image acquisition. It is useful in applications where low signal levels are expected as it allows to increase the exposure time significantly [77]. However, good optical access and sufficient space are required. If the rotor is tested in propeller configuration with an axial inflow, the mirror has to be installed preferably in *off-axis* configuration [119] causing additional challenges in order to synchronize the rotation rates of the mirror setup and the rotor. The sketches in Fig. 1.6 illustrate the possible rotating mirror setups for rotor tests (rotation rates are denoted as ω in the figure). Both methods, image deblurring during post-processing and the rotating mirror technique, have recently been compared in more detail by Pandey et al. [109].
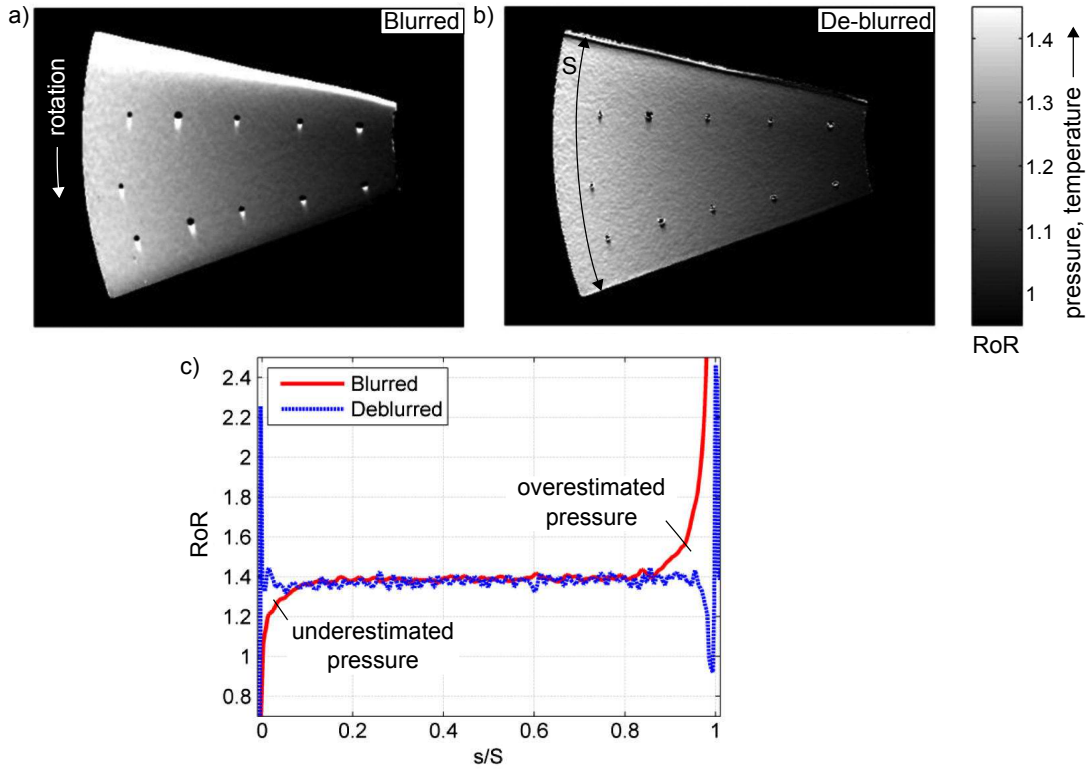
Figure 1.4: PSP results of a rotating-disc section in terms of ratio of ratios *RoR* (see Eq. 1.1). *a)* Before and *b)* after application of the image de-blurring algorithm from [51, 64]. *c)* Chordwise profiles of *RoR* expressing biased result due to blur and increased noise level after application of de-blurring algorithm (figures are modified from [51]).

1.2 Boundary-layer transition on rotating blades

For flows over aerodynamic surfaces two main categories can be distinguished with respect to boundary-layer transition from the laminar to the turbulent state [65]. The first category is connected with the growth of small initial disturbances inside the boundary layer and the associated amplification of instabilities finally causing transition to turbulence. The second category, often referred to as "bypass" transition, is associated with immediate and non-linear laminar-flow breakdown. The latter usually occurs at high levels of external disturbances like increased free-stream turbulence levels or surface roughness. For instance, bypass transition was observed near the blade tip of a full scale BO105 helicopter in hovering flight [55, 124]. In these studies the wake comprising the tip vortex and slipstream of the preceding blade directly interferes with the boundary-layer flow and causes immediate transition to turbulence. A review on bypass transition is provided for instance by Morkovin [102].

An overview on possible transition mechanisms for helicopter rotor blades is given by Heister [57]. In addition to bypass transition, previous studies (see Sec. 1.2.3) identified Tollmien-Schlichting instabilities and transition over laminar separation bubbles to be the dominant mechanisms for boundary-layer transition on helicopter rotor blades in hover. Both of these phenomena are
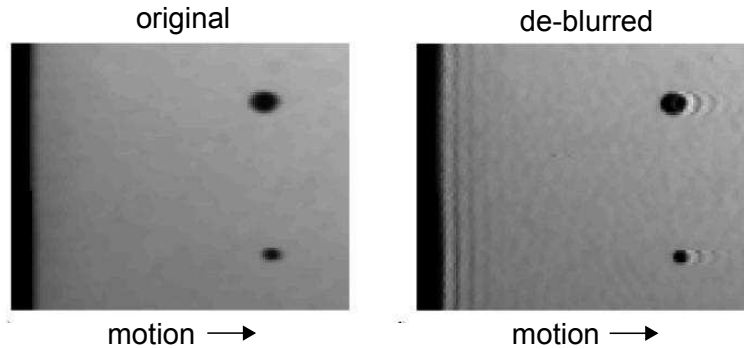
Figure 1.5: Demonstration of *Gibbs ringing* as an artifact of the image de-blurring algorithm (modified from [51]).
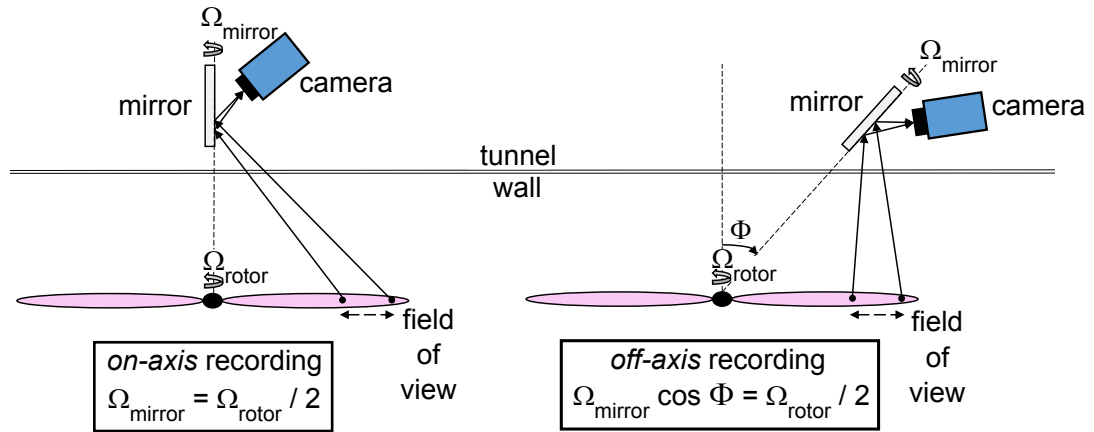
Figure 1.6: Sketches of *on-axis* and *off-axis* rotating mirror setups (modified from [109]).

characteristic for predominantly two-dimensional (2D) flows. However, the boundary layer on rotating blades is not necessarily 2D. Both swept blade geometries and rotational forces could in principle cause transverse flow components which are prone to cross-flow instabilities eventually causing laminar-turbulent transition. Cross-flow instabilities appear as co-rotating vortices and are usually observed close to the leading edge of stationary and highly swept wings (see e.g. [48]) or on rotating disks where cross flow is due to centrifugal forces [71]. For purely rotating helicopter rotors no evidence of cross-flow induced transition has been reported. In contrast, Heister's numerical study [57] on the flow around the ONERA 7AD rotor in forward flight has shown that cross-flow instabilities do play a role. This is the case on the blade pressure side and especially when the cross-flow velocity imposed by the forward motion of the rotor is large.

The investigated rotor blades in this study do not comprise a sweep angle and the flow is investigated on the blade suction side as well as in pure rotation with a superposed axial inflow, which prevents blade-vortex interaction. The resulting configuration is similar to a helicopter rotor in climb (see Sec. 2.2.1) and therefore, neither cross-flow instabilities nor bypass transition are a priori expected. Furthermore, effects due to cross-flow components originating from rotational forces are implicitly investigated in Sec. 3.3.4. It is further an aim of this study to compare measured transition

data to results of numerical tools employing 2D theories and flow assumptions only. Hence, in the following section the fundamentals on boundary-layer theory and transition to turbulence are described for 2D flows focusing on Tollmien-Schlichting transition.

1.2.1 Fundamentals on 2D boundary-layers and laminar-turbulent transition

Boundary-layer equations and properties Viscous flows are characterized by the Reynolds number which expresses the ratio between inertial forces and viscous forces according to

$$Re = \frac{\nu \tilde{l}}{\tilde{u}} \tag{1.2}$$

where $\tilde{l}$ and $\tilde{u}$ denote a characteristic length- and velocity scale of the investigated flow. For viscous flows on an airfoil typical characteristic quantities are the chord length c and the resulting inflow velocity u_{res}.

The governing equations for boundary-layer flows are a simplified form of the Navier-Stokes equations for the conservation of mass (continuity), momentum and energy, under consideration of the boundary-layer assumptions of Prandtl [115]. Prandtl's boundary-layer concept in principle divides the flow over a surface into a thin viscous boundary-layer region of thickness δ (see Fig. 1.7) and an inviscid outer flow, where the viscous terms in the Navier-Stokes equations can be neglected [129]. Inside the boundary layer the velocity components are zero right at the wall while approaching the velocity of the outer flow at the boundary-layer edge δ asymptotically. One of the inherent assumptions to Prandtl's approach is that the characteristic length scale of the boundary layer is small in comparison with the scale of the aerodynamic body investigated, i.e. $\delta << c$. This hypothesis generally implies large Reynolds numbers, being in the order of $Re \geq O(1/\delta^2)$, which poses the second important assumption to boundary-layer theory.
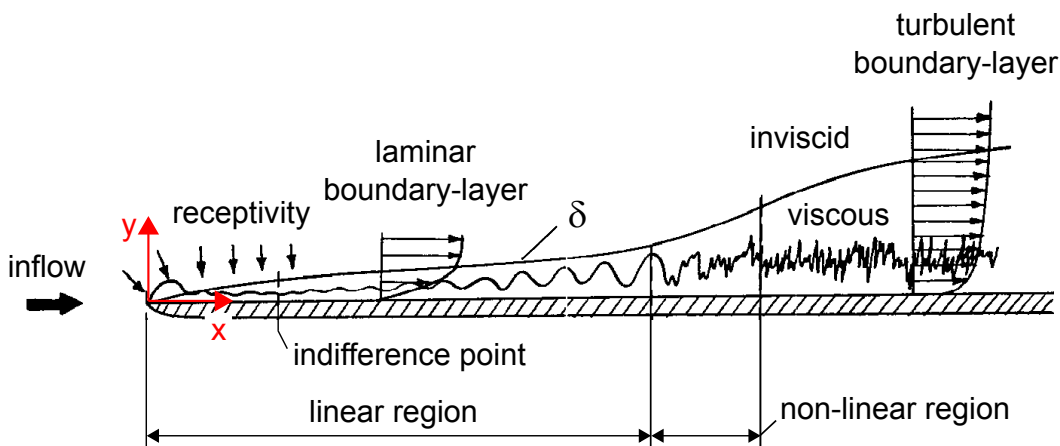
Figure 1.7: Qualitative sketch of the transition process from a laminar to a turbulent boundary layer for the flow over a flat plate (modified from [66]).

A detailed derivation of the Navier-Stokes equations and the application of Prandtl's order-of-magnitude analysis to obtain the boundary-layer equations is provided e.g. by Anderson [1]. For

two-dimensional, steady and compressible flows the equations for the velocity components $[u, v]$ in streamwise and wall-normal directions $[x, y]$ as well as for pressure p and temperature T in a laminar boundary layer are:

$$\text{continuity:} \qquad \frac{\partial (\rho u)}{\partial x} + \frac{\partial (\rho v)}{\partial y} = 0 \qquad (1.3)$$

$$\text{x-momentum:} \qquad \rho u \frac{\partial u}{\partial x} + \rho v \frac{\partial u}{\partial y} = -\frac{\mathrm{d}p_e}{\mathrm{d}x} + \frac{\partial}{\partial y}\left(\mu \frac{\partial u}{\partial y}\right) \qquad (1.4)$$

$$\text{y-momentum:} \qquad \frac{\mathrm{d}p}{\mathrm{d}y} = 0 \qquad (1.5)$$

$$\text{energy:} \qquad \rho u \frac{\partial h}{\partial x} + \rho v \frac{\partial h}{\partial y} = \frac{\partial}{\partial y}\left(k \frac{\partial T}{\partial y}\right) + u \frac{\mathrm{d}p_e}{\mathrm{d}x} + \mu \left(\frac{\partial u}{\partial y}\right)^2 \qquad (1.6)$$

In the above relations both the dynamic viscosity $\mu(T)$ and the thermal conductivity $k(T)$ denote temperature dependent fluid characteristics. The specific enthalpy h is related to temperature via the specific heat capacity at constant pressure κ_p according to:

$$h = \kappa_p T \qquad (1.7)$$

The system of equations is completed by considering the ideal gas law

$$p = \rho R_{\text{air}} T \qquad (1.8)$$

with R_{air} being the gas constant for air. A result of Prandtl's boundary-layer assumptions is that the pressure gradient disappears in wall-normal direction (see Eq. 1.5). It means that the pressure inside the boundary layer and on the wall is practically imposed by the inviscid condition at the boundary-layer edge, denoted by the subscript $_e$. Assuming that the pressure distribution $p(x) = p_e(x)$ is known from measurements or numerical solutions, the equations 1.3, 1.4, 1.6, 1.7 and 1.8 pose a system of five equations for the five unknowns u, v, ρ, T and h. A solution to these equations in principle yields the boundary-layer profiles necessary to perform a stability analysis. Solutions can either be obtained by solving the stated set of differential equations using a finite difference method to obtain velocity and temperature profiles directly or by using an integral approach where the system of equations is integrated in wall normal direction [129]. In this thesis boundary-layer solutions are obtained by the boundary-layer solver COCO from Schrauf [133], in which the first approach is implemented, as well as by the coupled Euler-/ boundary-layer code MSES from Drela [25], which solves the above stated equations in an integral form (see Sec. 3.4 for more details on the codes). Integral boundary-layer solutions utilize the displacement thickness δ_1, the momentum thickness δ_2 and the shape parameter H_{12} as characteristic boundary-layer quantities. They are defined as follows.

$$\delta_1(x) = \int_0^\infty \left(1 - \frac{\rho u}{\rho_e u_e}\right) dy \qquad (1.9)$$

$$\delta_2(x) = \int_0^\infty \left[\frac{\rho u}{\rho_e u_e}\left(1 - \frac{u}{u_e}\right)\right] dy \qquad (1.10)$$

$$H_{12} = \frac{\delta_1}{\delta_2} \qquad (1.11)$$

Both δ_1 and δ_2 are related to decrements in the flow which are due to the presence of the boundary layer. Whereas δ_2 can be regarded as a measure for the lack of momentum flow inside the boundary layer, the displacement thickness δ_1 expresses the mass-flow defect. In other words, "δ_1 is the distance away from the body surface through which the outer inviscid flow is displaced due to the boundary layer" [1]. The shape factor H_{12} is sensitive to the streamwise pressure gradient in the flow. The value of $H_{12} = 2.59$ corresponds to the analytical Blasius solution at zero streamwise pressure gradient ($\mathrm{d}p_e/\mathrm{d}x = 0$), higher and lower values correspond to decelerated and accelerated flows, respectively [129]. Saric [127] notes that for a given pressure gradient the change in H_{12} is more sensitive than a corresponding change in pressure coefficient c_p (see Eq.2.5). For this reason the shape factor H_{12} is often used to characterize the streamwise pressure gradient a boundary layer is exposed to.

A comprehensive overview on boundary-layer theory and approaches to obtain solutions of the boundary-layer flow is provided by Schlichting and Gersten [129].

Phenomenology of laminar-turbulent transition   The transition process is schematically sketched in Fig. 1.7 for the simple case of a two-dimensional boundary layer on a flat plate. According to Kachanov [65] the phenomenon can be divided into three stages known as *receptivity*, *linear stability* and *non-linear* breakdown to turbulence.

Assuming a low level of external disturbances, the flow downstream of the stagnation point is initially laminar. External disturbances comprise for instance acoustic waves, surface roughness, free-stream vortical, temperature or vibrational fluctuations. The process of how these external perturbations are transformed into oscillations inside the laminar boundary layer, the Tollmien-Schlichting waves, is called receptivity and has first been studied by Morkovin [101, 102]. Up to a certain point downstream, the indifference point, any oscillations inside the boundary layer are damped. As the boundary-layer thickness increases and disturbances pass this point, the flow becomes unstable against small disturbances which are amplified as they convect downstream. The indifference point is therefore also called point of primary instability. The initial growth of disturbances can be described by linear stability theory which is outlined in the next paragraph. In the corresponding linear regime the flow is 2D and instabilities are small enough to coexist. If oscillations are amplified high enough, the 2D waves start to interact non-linearly with three-dimensional disturbances. The original 2D base-flow starts to deform three-dimensionally and is subject to secondary instabilities. The stimulation of secondary instabilities in the non-linear regime is significantly higher than in the linear regime. Hence, the extent of the non-linear flow regime is much smaller [3, 168]. The eventual breakdown to turbulence is accompanied by the initial occurrence of turbulent spots [32] which is often associated with transition onset [3]. The spots are spatially confined, appear randomly and grow in size as they are convected downstream. Turbulent flow is therefore initially intermittent until the spots combine to form a fully turbulent flow. Experimental studies by van Hest [155] showed that both growth rate and lateral spreading of these spots are favored by streamwise increasing pressures. The growing velocity fluctuations in a transitional boundary-layer are connected to increased momentum transfer in wall normal direction. In terms of the statistical mean the resulting velocity profile of a turbulent boundary layer is "fuller" and has a larger velocity gradient at the wall when compared to a laminar boundary-

layer (see Fig. 1.7). According to Newton's friction law [129] an increased velocity gradient at the wall relates to a higher wall shear-stress τ_w via the flow medium's dynamic viscosity μ:

$$\tau_\mathrm{w} = \mu \left(\frac{\partial u}{\partial y} \right)_{y=0} \tag{1.12}$$

The corresponding skin friction coefficient c_f is defined as:

$$c_f = \frac{\tau_\mathrm{w}}{\frac{\rho_\infty}{2} u_\infty^2} \tag{1.13}$$

Linear stability theory   In principle, linear stability theory (LST) describes the stimulation behavior of small, wave-like two- or three dimensional disturbances in a laminar boundary-layer. A comprehensive overview and detailed explanations along with underlying equations for both compressible and incompressible LST are provided by e.g. Mack [93]. The basic ideas are briefly described hereafter focusing on the concepts of two-dimensional (2D) local LST.

In the frame of LST the flow variables inherent to the governing equations, in a generalized form denoted as q, are divided into steady mean flow terms $\overline{q}$ and unsteady, superposed disturbance terms, q':

$$q(x, y, t) = \overline{q}(x, y) + q'(x, y, t) \tag{1.14}$$

The generalized variable q can represent a velocity component $[u, v]$ in streamwise- or wall normal direction $[x, y]$, pressure p, density ρ or temperature T. In doing so, a parallel flow assumption forces the wall normal component of the mean flow to be zero, i.e. $\overline{v} = 0$. This also eliminates the dependency of $\overline{q}$ in x-direction and enforces a *local* approach to the problem. Assuming that the mean flow poses a solution to the system of equations, the relations are reduced to a system of differential equations describing the dynamics of the perturbations only. These equations are then linearized by neglecting all higher order disturbance terms. Linearization reflects the key assumption inherent to LST, meaning that disturbance quantities are small with respect to the mean flow. In order to solve the linearized system of equations the perturbation quantities are approximated by a superposition of harmonic waves with small amplitude according to the following approach:

$$q'(x, y, t) = \widehat{q}(y) e^{i(\alpha x - \omega t)} + c.c. \tag{1.15}$$

In this expression $\widehat{q}(y)$ is the complex amplitude function dependent on the wall normal coordinate, α denotes a wave number in x-direction and ω is the angular frequency of the disturbance, respectively. The complex conjugate (c.c.) needs to be considered in order to obtain real values for the disturbance quantity. Both Squire's theorem [146] and also Mack [93] state that for subsonic 2D boundary-layers it is sufficient to allow waves in streamwise direction only. Note also that in the frame of local theory the wave number α is independent of the streamwise coordinate. The wave number α and the frequency ω are in general complex numbers.

Experimental studies have shown that, in the linear regime, the propagation of Tollmien-Schlichting waves is a spatial process and that e.g. disturbance velocity amplitudes at fixed streamwise positions are time-independent [93]. Hence, boundary-layer transition is described by "spatial theory". In this context only the real part of the angular frequency is considered, i.e. $\omega_\mathrm{R} = 2\pi f_\mathrm{TS}$ with f_TS

denoting the frequency of the Tollmien-Schlichting wave in Hertz. In contrast, the wave number α remains complex and the imaginary part α_{I} represents the growth rate, where $\alpha_{\mathrm{I}} < 0$ denotes spatial amplification and $\alpha_{\mathrm{I}} > 0$ corresponds to attenuation of the disturbance wave.

Using the above stated assumptions, a resulting linearized differential perturbation equation can be formulated for the complex amplitude function $\widehat{q}(y)$, which describes the stimulation of two-dimensional waves in streamwise direction and in time. For compressible flow, the resulting system of differential equations is given (for three-dimensional flow) for instance by Schrauf [130–132]. For parallel, two-dimensional and incompressible boundary layers the governing differential equation for the disturbance growth rates is the Orr-Sommerfeld relation [104, 145]. First theoretical solutions of the latter were independently obtained for a Blasius boundary-layer by Tollmien in 1929 [152] and by Schlichting in 1933 [128]. It lasted until the 1940's when their findings and thus the concept of linear stability theory were experimentally corroborated by Schubauer and Skramstad [136].

e^N-method for transition prediction   A prerequisite for the stability analysis according to LST and the application of the e^N-method is a solution for the laminar boundary-layer flow at a given Reynolds and Mach number condition. Assuming that the laminar boundary-layer profiles are known along the streamwise coordinate x, a local stability analysis gives the growth rates of the locally unstable disturbances with frequency f_{TS}. Using the disturbance approach (Eq. 1.15) according to spatial theory, the growth rate α_{I} is the streamwise derivative of the logarithmic disturbance amplitude A:

$$\alpha_{\mathrm{I}} = -\frac{1}{A}\frac{dA}{dx} = -\frac{d\,\ln A}{dx} \tag{1.16}$$

Solutions of the stability analysis can be summarized in a stability diagram as depicted in Fig. 1.8a. It shows the range of amplified Tollmien-Schlichting frequencies f_{TS} along the streamwise coordinate. The amplified range is confined by the neutral stability curve which represents the solutions corresponding to zero growth rate ($\alpha_{\mathrm{I}} = 0$). Note the indifference point x_0, downstream of which the first waves with initial amplitude A_0 are amplified. According to the e^N-method, the growth rates for each amplified frequency are integrated along the streamwise direction. This way, one obtains a ratio of the disturbance amplitude A at any position x with respect to some initial amplitude A_0 at the indifference point x_0. The integrated growth rates are called "N-factor" and defined as:

$$N(f_{\mathrm{TS}}, x) = \ln\frac{A}{A_0} = \ln\frac{A\,(f_{\mathrm{TS}}, x)}{A_0\,(f_{\mathrm{TS}}, x_0)} = -\int_{x_0}^{x}\alpha_{\mathrm{I}}\,(f_{\mathrm{TS}})\,dx \tag{1.17}$$

Examples of integrated N-factors are schematically shown for three amplified frequencies in Fig. 1.8b. The curves correspond to the frequencies sketched in the stability diagram in part a) of the figure. Note that the integrated growth rates decrease as waves with constant f_{TS} propagate into streamwise regimes where they are attenuated. The red line connects the maximum values of all N-factor curves and is denoted as envelope. The resulting envelope therefore corresponds to the maximum amplification factor of the disturbances. In other words, the N-factor envelope expresses the increase of the amplitude ratio $\ln A/A_0$ for the wave which is amplified the most as it passes the indifference point.
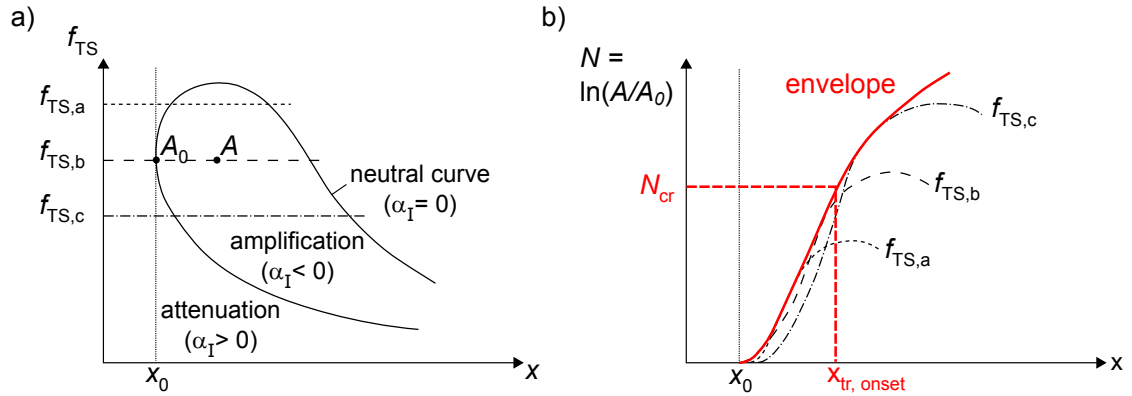
Figure 1.8: *a)* Sketch of stability diagram for three amplified Tollmien-Schlichting waves *b)* Correlation of transition N-factor in the framework of the e^N-method.

The use of this concept for the prediction of boundary-layer transition was independently developed by van Ingen [60] as well as by Smith and Gamberoni [143]. According to their findings, transition to turbulence commences if a threshold value for the maximum integral growth rate, N_{cr} is reached. In practical applications, the critical N-factor is found by correlating the measured position for the onset of boundary-layer transition with the corresponding N-factor maximum. See Sec. 1.2.2 on how transition onset is found in general and Sec. 3.3.1 for the definition used in this study.

Application of the e^N-method yields a critical amplification ratio. In other words, the initial disturbance amplitudes A_0 are ignored (see Eq. 1.17). A first approach to counteract this deficiency was made by Mack [92], who found that the critical N-factor depends on the turbulence intensity Tu of the incident flow, which in turn reflects the level of initial disturbance amplitudes. The turbulence intensity Tu is usually determined by the root-mean-squared (RMS) value of the velocity disturbances relative to the resultant incident flow u_{res}. The turbulence of the incident flow is often assumed to be isotropic.

$$Tu = \frac{\sqrt{\frac{1}{3}\left(\overline{u'^2} + \overline{v'^2} + \overline{w'^2}\right)}}{u_{res}} \approx \frac{\sqrt{\overline{u'^2}}}{u_{res}}. \tag{1.18}$$

Based on transition experiments on a flat plate without pressure gradients Mack [92] found the following correlation between the critical N-factor and the turbulence intensity which is valid in the range $7 \times 10^{-4} < Tu < 3 \times 10^{-2}$:

$$N_{cr} = -8.43 - 2.4 \ln Tu \tag{1.19}$$

Since Tu is characteristic for the facility where transition experiments are carried out the critical N-factor needs to be calibrated accordingly. For this reason the e^N-method is often referred to as being "semi-empirical".

Another assumption inherent to the e^N-method is that all waves being prone to instability have the same initial amplitudes. This is a rather crude hypothesis, as it neglects that for instance different modes could in principle be excited by the same disturbance, e.g. by acoustic waves, at different efficiency before or as they are coupled into the boundary layer. A more comprehensive discussion of the shortcomings of the outlined method is provided by Arnal [3].

Since the presented method is based on linear theory, while neglecting the non-linear amplification of disturbances, the use as prediction tool is only justified if the non-linear regime is comparatively small. For two-dimensional incompressible boundary-layers with zero pressure gradient Arnal [3] reports that the extent of linear amplification of disturbances covers between 75 to 80 % of the distance between the leading edge and the beginning of transition, i.e. the onset of turbulent spots. The spatial fraction of non-linear amplification is even smaller if the boundary layer faces adverse pressure gradients [155]. Despite the stated simplifications and assumptions, the method is state of the art and has been employed successfully in many different applications [61].

According to Arnal [3] and summing up the aspects mentioned above, the following steps are involved in order to obtain the transition N-factor N_{cr} when using the e^N-method:

1. Calculation/description of laminar velocity profiles along the boundary-layer flow to be investigated

2. Calculation of stability characteristics, i.e. growth rates, for the velocity profiles according to LST

3. Calculation of the integral of local growth rates along a defined propagation direction of disturbances to obtain curves denoting the maximum amplification factor of all amplified waves

4. Correlation of measured transition data with maximum amplification curves to obtain the threshold value N_{cr}

In turn, if N_{cr} and the stability characteristics of the boundary layer are known, the method allows to predict the streamwise position where transition to turbulence sets in.

Stability modifiers   There are numerous conditions which in principle influence the stability characteristics of a laminar boundary layer. A detailed view into the subject is provided by Arnal [3], who identified the following aspects as driving parameters for the stability characteristics of a laminar boundary layer according to linear stability theory:

- Pressure gradient (dp_e/dx): Positive "adverse" streamwise pressure gradients destabilize the boundary layer, whereas negative "favorable" gradients have a stabilizing effect.

- Wall heating/cooling: For boundary-layer flows in air, wall heating destabilizes the boundary layer, whereas wall cooling has a stabilizing effect (see also [37, 129]).

- Compressibility: For free stream Mach numbers of $M \leq 2$, compressibility has a damping effect on amplified disturbances and therefore stabilizes the boundary layer (see also [2, 91]).

Transition over laminar separation bubbles   Laminar separation bubbles (LSB) are a typical phenomenon of flows over airfoils especially at low Reynolds numbers. An instantaneous visualization of a typical LSB is provided in Fig. 1.9a. If a laminar boundary layer is decelerated enough
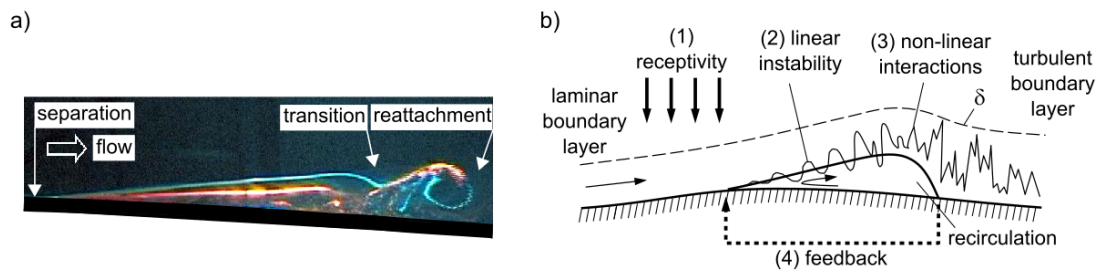
Figure 1.9: *a)* Instantaneous visualization of a laminar separation bubble by hydrogen bubbles and rhodamine in water (modified from [76]) *b)* Instability and transition mechanisms in a laminar separation bubble (modified from [22]).

by a streamwise increasing pressure, the flow separates as it is forced to reverse its direction in the near wall region. Downstream of the separated laminar shear layer transition to turbulence sets in. If a LSB is formed, the increased momentum transfer in wall-normal direction, as a result of the transition process, eventually causes the flow to re-attach and to form a confined region similar to a *bubble* with recirculating flow inside. It should be noted that the phenomenon is instationary and, as depicted in Fig. 1.9a, transition to turbulence is accompanied with formation and shedding of coherent structures in the shear layer. Thus, the momentum increase in wall normal direction leading to re-attachment has to be regarded in a time averaged sense and the characteristic locations corresponding to separation, transition and reattachment are driven by the dominant instabilities as well as by external disturbances inherent to the boundary-layer flow. The instability and transition mechanisms in a LSB are reviewed in detail by Dovgal et al. [22], studied more comprehensively by means of direct numerical simulations (DNS) by Rist [123] and summarized briefly in the sketch in Fig. 1.9b. Similar to the Tollmien-Schlichting transition process described above, initial disturbances are coupled into the boundary layer via receptivity (1) before they are amplified in the evolving boundary-layer prior to separation. The amplification process along the separating laminar boundary layer can be described by linear stability theory (2) until disturbance amplitudes are high enough to cause non-linear interactions (3), which eventually lead to laminar-turbulent transition, followed by re-attachment. It is further believed that, due to the reverse flow near the wall an upstream *feedback* (4) of disturbances exists inside the LSB. The amplification of disturbances is significantly stronger in laminar separated regions than under attached flow conditions, such is the streamwise portion of non-linear growth. Rist [123] showed that transition over a laminar separation bubble is predominantly due to 2D Tollmien-Schlichting transition. His DNS computations further showed excellent agreement to disturbance growth rates approximated by LST. This finding was verified experimentally by Würz [168].

Examples of boundary-layer transition over LSBs on helicopter rotor blades in hover are reported for instance in [96, 156, 160] and discussed in Sec. 1.2.3. In these studies the laminar separated regions were detected either by ammonium traces or oil films on the blade surfaces, both experiencing a predominant centrifugal force in the separated flow region.

1.2.2   Measurement of boundary-layer transition on rotating blades

In general "the beginning of transition is often taken at the point of initial measurable deviation of a characteristic parameter from its laminar evolution" [2]. The detection of the transition region therefore depends on the capability of the technique used. Experimental methods for the investigation of laminar-turbulent boundary-layer transition rely on the changing nature of the wall-bounded velocity profile in the transition region.

Increased velocity fluctuations inside the boundary layer can be captured by fast-responding hot films or hot wires, mounted directly on or slightly above the investigated model surface [10]. In this way the "intermittency factor" can be obtained. It is defined as the time fraction related to the passage of turbulent spots. The intermittency factor is equal to zero in laminar flow and equal to one in the fully turbulent boundary-layer. Significant increases of the RMS reading of a hot film signal or measurable deviations of the intermittency factor from zero are often attributed to the onset of boundary-layer transition as in the studies of Schubauer and Klebanoff [135] or Owen [107], for instance. The use of hot wires and hot films to determine the boundary-layer state of full scale and model scale helicopter rotor blades has been demonstrated for instance by McCroskey [96] and Raffel et al. [118]. However, these techniques are only feasible at very limited spatial resolution and demand high effort with respect to model instrumentation and data transfer from the rotating to the stationary system. Other techniques rely on a detectable variation of parameters due to the changing shape of the statistically averaged velocity profile in transitional boundary-layers. For instance, a streamwise minimum in Pitot pressures [136] or a sudden increase in skin friction can both be attributed to the onset of transition. Both are related to the relatively fuller velocity profile in turbulent boundary layers and the resulting increased gradient at the wall. Sublimation of acenaphthene coatings was used to visualize the effect of boundary-layer transition on hovering rotors at full scale [9, 124, 151] and on model scale rotors [96, 156]. Sample results from the study of Tanner and Yaggy [151] are provided in Fig. 1.10a. The images were acquired on the upper and lower surface of a UH-1B main rotor in hover. The change from laminar to turbulent boundary-layer flow appears as the change from bright to dark. Note also the turbulent wedges emanating from the leading edge due to single elements with increased roughness.

Gardner and Richter [39] identified laminar-turbulent boundary-layer transition on static and dynamically pitching 2D airfoils by analyzing the standard deviation of the surface pressure distribution, denoted as σ_{c_p}. They found that σ_{c_p} peaks in the transition region and close to the point of 50 % turbulence intermittency. In contrast to microphone measurements (see e.g. [82]), which capture increased levels of high frequency fluctuations ($\sim$ kHz) in the transition region, the σ_{c_p} method proposed in [39] also works for 1 Hz-low-pass filtered pressure signals. The increased level of low frequency pressure fluctuations originates from the alternating position of the pressure rise at transition to turbulence, which is in turn due to the thickening of the boundary layer [114]. To date only Schwermer et al. [142] applied the σ_{c_p}-method on rotating blades, identifying boundary-layer transition on a dynamically pitching Mach-scaled rotor configuration.

The change in skin friction resulting from transition to turbulence can also be measured using oil film interferometry. When illuminated with a monochromatic light source, the oil film reflects an interferometric pattern which is characteristic of the oil film thickness and therefore a function of
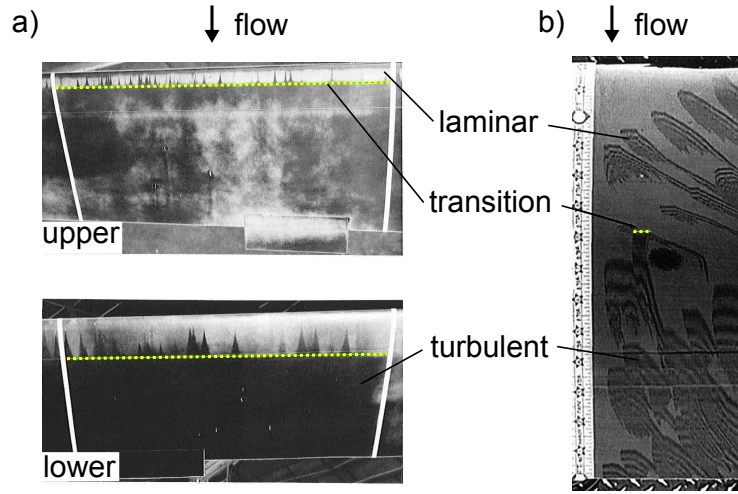
Figure 1.10: *a)* Boundary-layer transition visualization on the upper and lower side of a full scale UH-1B main rotor by Tanner and Yaggy [151] *b)* Interferometric oil patterns from skin-friction measurements indicating transition to turbulence on the suction side of a full-scale XV-15 tilt rotor blade by Wadcock et al. [160].

the shear stress acting on it [150]. The technique was successfully applied on hovering tilt rotors by Wadcock et al. [160] and on fast rotating propellers by Schülein [138]. A sample result from [160] acquired on a hovering XV-15 tilt rotor is depicted in Fig. 1.10b, where laminar and turbulent regions correspond to areas with small or large spacing of interferometric oil pattern lines.

The change from laminar to turbulent flow on surfaces also results in different heat transfer characteristics which can basically be used in two different ways, when investigating the phenomenon with thermography methods. The first approach employs the natural increase of the adiabatic wall recovery temperature T_{aw} in turbulent as compared to laminar flows and the second method makes use of higher convective heat transfer in turbulent boundary-layers. The adiabatic wall recovery temperature can be expressed as

$$T_{aw} = T_\infty \left(1 + r(Pr)\frac{\gamma - 1}{2}M_\infty^2 \right) \tag{1.20}$$

where T_∞ is the ambient temperature, M_∞ is the inflow flow Mach number ($u_\infty/\sqrt{\gamma R_{air}T_\infty}$) with κ and R_{air} being the ratio of specific heats and the ideal gas constant. The recovery factor $r(Pr)$ is a function of the Prandtl number and can be interpreted as the conversion factor of the kinetic energy to thermal energy, as the flow is adiabatically decelerated to rest. At a Prandtl number of $Pr = 0.72$ in air the recovery factor was found to be $r(Pr) = 0.85$ and $r(Pr) = 0.90$ for laminar and turbulent boundary-layers, respectively [30]. Measuring transition via differences in T_{aw} works in flows at high Mach numbers and high temperatures. For instance, Peake et al. [110] used this approach on a flat plate at $M_\infty = 3.85$ using an infrared (IR) camera.

The increased heat convection of boundary layers, when changing from laminar to turbulent, can be expressed by an increase of the dimensionless wall heat flux also denoted as Stanton number St. St is a function of the heat transfer coefficient η and according to Reynolds analogy proportional
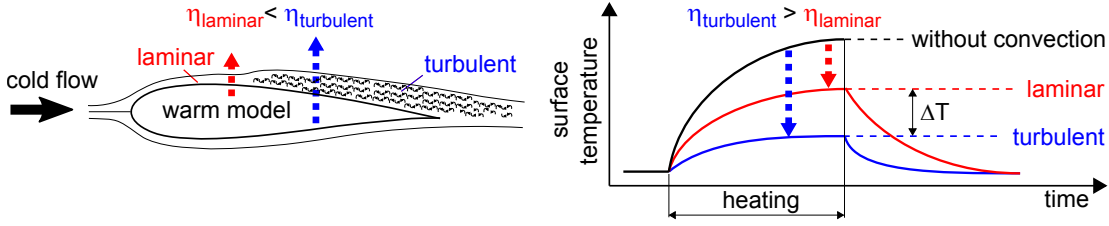
Figure 1.11: Working principle for thermography measurements of boundary-layer transition. Model surface is heated to enhance temperature difference between laminar and turbulent regions due to different heat transfer coefficients η, respectively.

to the local skin friction coefficient c_f (see Eckert and Drake [31] for more details):

$$St = \frac{\eta}{\rho_\infty \kappa_p u_\infty} \sim \frac{c_f}{2} \tag{1.21}$$

In this relation κ_p is the specific heat capacity at constant pressure. The analogy is practically used by creating a temperature difference between the model surface and the flow, for instance by heating the model surface as sketched in Fig. 1.11. This way the temperature difference between laminar and turbulent wetted areas is amplified and therefore measurable at higher SNR than when relying on differences in the recovery temperature.

Thermography methods have been used frequently to detect boundary-layer transition as they are non-intrusive, due to their capability to obtain data at high spatial resolution and because of the possibility to systematically detect distinct points in the transition region by automated post-processing of digitized data. Promising results were obtained via high-speed infrared (IR) imaging of model scale rotors in hover by Heineck et al. [54] as well as by Overmeyer and Martin [105]. The technique was also applied by Richter and Schülein [121] to investigate transition on Eurocopter's BO105 and EC135 full scale rotor blades and by Richter et al. [122] for measurements on a full scale BK117-type rotor (see Fig. 1.12 for a sample result). Richter and Schülein [121] reported a scatter in the detected transition onset and end of $\Delta = 6 - 12\,\%$ chord depending on the blade tip speed of 94 - 189 m/s. The distinct points were detected using an automatized post-processing procedure as proposed by Schülein [137]. The positions corresponding to transition onset and end were estimated by intersecting a straight line in the transition region with the signal corresponding to laminar and turbulent flow, respectively.

In addition to using IR, transition can also be measured by means of temperature-sensitive paint (TSP) [36]. Whereas the IR signal benefits from a higher temperature resolution ($\sim 0.02\,\mathrm{K}$ as opposed to $\sim 0.1\,\mathrm{K}$ for TSP [153]), TSP data is usually provided at significantly higher spatial resolution. This is due to the use of e.g. scientific grade CCD-sensors for the TSP technique as compared to IR cameras for imaging the temperature-dependent information on the investigated surface. Though the IR technique does not rely on a special surface coating as TSP, IR measurements often suffer from unwanted reflections of IR rays on the model surface [121, 122].

Similar to the PSP technique (see Sec. 1.1.1) TSP relies on photokinetic interactions between the airflow and a luminescent coating being applied on a model surface of interest [85]. When excited by light of a certain wavelength, the luminescent dye molecules emit light at a longer
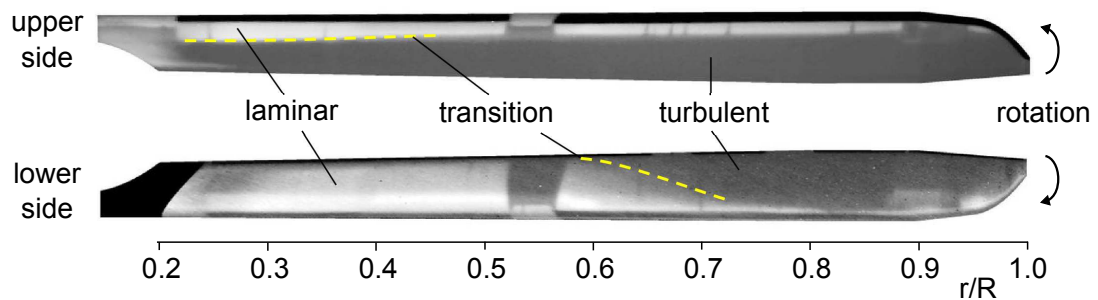
Figure 1.12: Boundary-layer transition measurements on the upper and lower side of a full-scale BK117-type rotor obtained via high-speed infrared thermography by Richter et al. [122].

wavelength. The difference to PSP is that the TSP luminophores are embedded inside an oxygen impermeable binder material. For this reason, the amount of light emitted is mainly quenched by thermal energy inside the TSP sensor and therefore inversely proportional to the temperature of the sensor, i.e. on the model surface. The technique has recently been used for transition measurements on fast rotating propellers by Yorita et al. [170] and on model rotor blades equipped with a modified NACA0015 airfoil by Lang et al. [77]. In [77], boundary-layer transition was found to be triggered by a laminar separation bubble after correlating TSP data with high resolution particle-image velocimetry (PIV) results. The TSP signal was therefore evaluated with respect to points associated with laminar separation and turbulent reattachment which could be detected with a statistical error of $\pm 2\%$ chord.

In this study, boundary-layer transition is measured via both IR and TSP. When using changes in macroscopic quantities for transition detection, e.g. differences in heat transfer, one should be aware that a measurable deviation from the laminar state can only be detected when the flow is already intermittent. This hypothesis is supported by the findings from Schubauer and Klebanoff [135], who discovered only minor changes in a time averaged velocity profile from the fully laminar state at a position where already 16% intermittency was measured. In this respect, Owen and Horstmann [108] showed that the transition onset detected by heat transfer measurements and defined as the beginning deviation from the laminar evolution occurs further downstream of the position where turbulent fluctuations could already be detected with hot-wire anemometers.

1.2.3 Previous findings on rotating blade boundary layers and effect of rotational forces

Centrifugal and Coriolis forces in rotating blade aerodynamics The significance of rotational forces on rotating blade aerodynamics first became apparent in 1947 with Himmelskamp's investigations on the aerodynamic characteristics of propeller blade sections and the comparison to data obtained in a stationary reference frame (see [59]). He found that rotation postpones stall onset to higher lift coefficients than it would be expected from non-rotating, two-dimensional tests with the same airfoil. Based on the sectional lift polars as depicted in Fig. 1.13, it was concluded that the airfoil performance was systematically augmented when observing blade sections closer to the propeller hub. Himmelskamp supposed that the observed effect can only be explained by
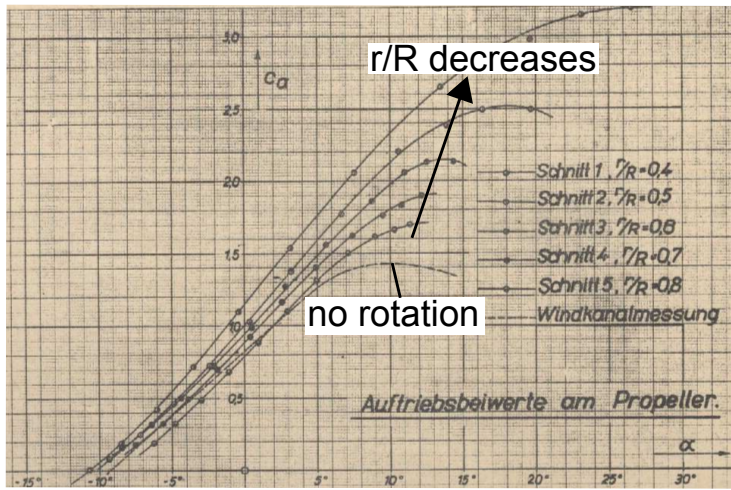
Figure 1.13: Sectional lift polars (c_a vs. α) from the study of Himmelskamp [59] showing increased maximum lift coefficients of rotating blade sections when compared to non-rotating data.

a physical mechanism acting on the viscous boundary-layer at the wall. Although supporting theoretical studies on the effect of rotational forces did not exist at the time, his physical reasoning for the observed "rotational augmentation" is in line with later findings. For illustration purposes the boundary layer on a blade rotating at constant angular velocity Ω is qualitatively sketched in Fig. 1.14 along with the individual components of the force field acting on it. Himmelskamp argues that as the boundary layer passes the rotating blade, the portion adherent to the surface actually "participates" in the rotation. The wall-bounded fluid is therefore directly exposed to the centrifugal force causing a velocity component w directed radially outward as the momentum is transferred through the viscous boundary-layer. In literature this process is often referred to as "centrifugal pumping" (e.g. in [28, 151]) which, according to Himmelskamp, causes in principle two effects.
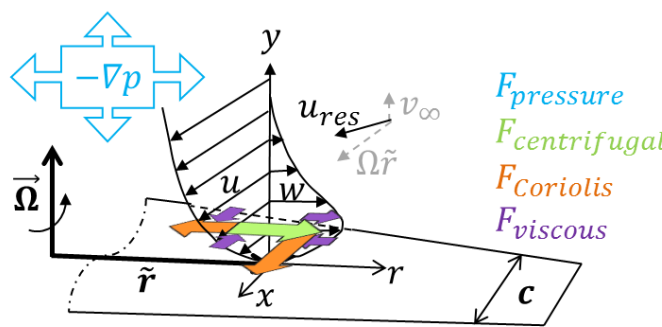
Figure 1.14: Boundary-layer profile at a characteristic radius $\tilde{r}$ on a blade rotating at constant angular velocity Ω and being exposed to an axial inflow perpendicular to the rotating plane. Velocity components in tangential x- and radial r direction are qualitatively sketched as u and w while being exposed to the denoted forces inherent to the rotating reference frame.

The first effect is related to the scaling of the centrifugal force field with the radius ($F_{\text{centrifugal}} \propto \Omega^2 r$)

meaning that the radial velocity increases with r. Hence, for a blade section at a specific radius more fluid is forced radially outboard than provided from an adjacent section further inboard. This eventually leads to a thinner boundary-layer as compared to equivalent conditions on a fixed wing. The second effect is due to the Coriolis force which acts in the rotating reference frame and on the velocity components relative to the rotating motion. If the wall-bounded fluid is directed radially outboard into regions with higher rotational speed, the Coriolis force accelerates the flow in tangential direction against the direction of blade rotation. In other words, the Coriolis force acts as a favorable tangential pressure gradient on the fluid moving radially outboard by adding kinetic energy to the wall nearest sections and therefore favoring attached flow conditions.

Scaling of rotational forces   Lentink and Dickinson [80] formulated the Navier-Stokes equations in a rotating reference frame, describing the relevant accelerations and stresses on a fluid particle close to a rotating wing surface (as sketched in Fig. 1.14). When applied to a blade at constant rotating speed, they identified the inverse Rossby number Ro^{-1} as the relevant dimensionless parameter to scale the relative contribution of Coriolis and centrifugal forces with respect to pressure and viscous forces.

$$\frac{D\vec{u}}{Dt} + \underbrace{\frac{c}{\tilde{r}} \cdot \frac{1}{\tilde{J}^2 + 1}}_{Ro^{-1}} \cdot \left[\underbrace{\vec{\Omega} \times \left(\vec{\Omega} \times \vec{r} \right)}_{\text{centrifugal}} + \underbrace{2\vec{\Omega} \times \vec{u}}_{\text{Coriolis}} \right] = \underbrace{-\frac{p_\infty}{\rho_\infty u_{res}^2} \cdot \nabla p}_{\text{pressure}} + \underbrace{\frac{1}{Re} \cdot \nabla^2 \vec{u}}_{\text{viscous}} \qquad (1.22)$$

In the above relation, $\tilde{r}$ is the characteristic radial position where rotational forces are investigated and $\tilde{J}$ is the (propeller) advance ratio based on the corresponding rotation speed, i.e. $\tilde{J} = u_\infty / (\Omega \tilde{r})$. The expression implies that rotational effects are more dominant at small radial distances from the hub and in hovering flight where minimum axial inflow is present, i.e. at $\tilde{J} = 0$. This scaling parameter is in line with previous theoretical studies [27, 28]. Fogarty [38] was the first to analyze a rotating laminar boundary-layer by investigating the Navier-Stokes equations under boundary-layer assumptions for an incompressible fluid at constant rotating speed and in proximity of $r/c \to \infty$. He showed that in this case the flow behaves predominantly two-dimensional, comprising only negligible radial flow. In fact, he showed that the tangential and radial velocity components become independent of each other as $r/c \to \infty$. Based on the same set of equations, the study was complemented by Rott and Smith [125] who additionally considered the influence of positive and negative pressure gradients. They confirmed that the radial outflow is in principle small as $r/c \to \infty$ and added that the existing radial flow would be stronger as the adverse pressure gradient is larger when compared to the situation at lower or favorable tangential pressure gradients. This was also confirmed by McCroskey and Yaggy [97].

Effect on delayed separation of laminar boundary-layers   In 1957, Liu [84] confirmed Himmelskamp's reasoning theoretically by showing that the delay of laminar separation is due to the Coriolis force acting on the flow directed radially outboard and that the effect occurs rather close to the hub than far away from it. Further insight into the effect of rotational forces on the delay of

laminar separation was shed by Banks and Gadd [7] as well as by Dumitrescu and Cardos [28]. They studied the effect for academic cases where the tangential flow was linearly retarded, seeking to simulate the flow over a rotating airfoil at adverse pressure gradients. It was found that the relative delay of laminar separation is increased if adverse pressure gradients are low. In view of the findings in [125] and [97], this means that an absolute increase of the radial flow component due to centrifugal pumping at comparatively higher adverse pressure gradients does not immediately delay flow separation further downstream. However, the findings are not contradicting. They simply show that a resultant effect of rotational forces, with respect to the delay of laminar separation, always has to be regarded in view of and relative to the acting pressure forces and that it cannot be judged simply by the amount of radial flow.

In more applied studies Dwyer and McCroskey [29] as well as Blaser and Velkoff [13] studied the influence of rotational forces on the boundary layer of a rotating blade in hover equipped with a NACA0012 airfoil. Dwyer and McCroskey found delayed separation as a consequence of rotational forces for $r/c < 6$ with an increasing effect as r/c is further decreased. The finding is depicted in Fig. 1.15, where flow separation obtained under consideration of rotational forces is indicated as "flow reversal line" and compared to the non-rotating case denoted as "2-D separation line". The radial distance r/c is expressed as z/c in the figure.
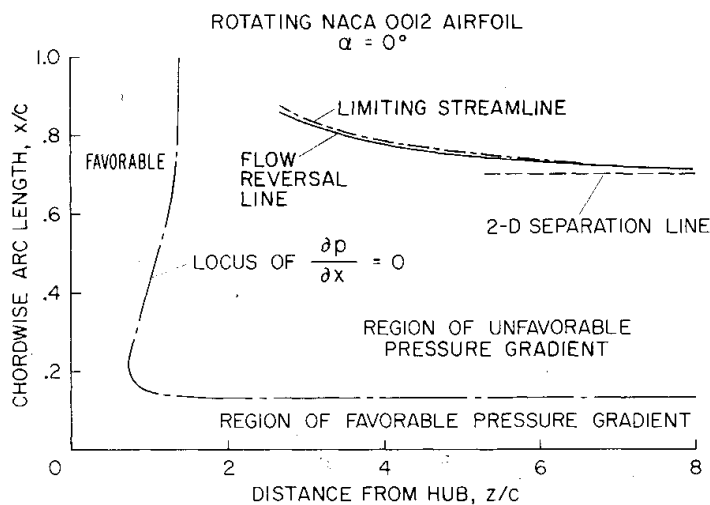
Figure 1.15: Effect of rotation on the position of laminar separation on a NACA 0012 airfoil (from Dwyer and McCroskey [29]).

The trend of increasingly delayed laminar separation at lower r/c ratios was confirmed by Blaser and Velkoff [13] as well as by Dumitrescu and Cardos [28] who studied the effect on the more academic linearly retarded flow as previously investigated by Banks and Gadd [7]. Other studies with respect to rotational effects on boundary-layer separation were performed on a theoretical basis by Du and Selig [27] as well as experimentally on wind turbine rotors by Tangler [149] and on full-scale tilt rotors by Felker et al. [35]. Though the literature shows that the effect of rotational forces, as prescribed by Himmelskamp, does exist, it has been commonly stated that the rotational effect has to be regarded as being of second order when compared to the influence of varying

pressure gradients on the separation of laminar boundary-layers. This is especially the case under high adverse pressure gradient conditions as at high angles of attack on airfoil suction sides [29]. A detailed quantification of the pressure gradients in the studies mentioned is missing.

In [29, 97] and [13], radial and tangential boundary-layer profiles were calculated and it was shown that in accordance with the scaling parameter r/c the tangential profiles were fuller especially closer to the hub. This observation was attributed to the favorable pressure gradient induced by the Coriolis force as mentioned above. The theoretical boundary-layer profiles on a rotating NACA0012 airfoil calculated by Blaser and Velkoff [13] showed good agreement to those obtained by Dwyer and McCroskey [29]. In the former study, theoretical tangential boundary-layer profiles were compared against hot-wire measurements on the corresponding rotating blade. The measured profiles were fuller than those obtained by the theoretical approach which suggests that the employed integral momentum theory tends to underestimate the accelerating effect of the Coriolis force.

Boundary-layer transition studies on hovering rotors   Few works exist where the effect of rotational forces on laminar-turbulent boundary-layer transition was investigated. To the author's knowledge the only experimental studies in this respect were performed by Tanner and Yaggy [151] and McCroskey [96]. In both studies, transition was measured on hovering rotors and on the corresponding stationary wings via sublimating acenaphthene coatings. Comparability between detected transition positions on the rotating versus the stationary wing was enabled by correcting the geometric pitch angle of the rotating blade by means of the standard blade-element momentum theory which for instance does not include the contraction effect of the rotor flow [151].

Tanner and Yaggy [151] measured boundary-layer transition on a rotating NACA 0015 airfoil at $Re_{\text{tip}} = 1.1 - 1.3 \times 10^6$ and several collective pitch settings. They found no significant differences of the measured transition positions between the rotating and non-rotating configuration. A radial position from where transition data was extracted for this comparison is not provided. Though not stated explicitly in [151], the experiments by Velkoff et al. [156] and McCroskey [96] on the same airfoil suggest that transition was triggered by a laminar separation bubble. In these studies, laminar separation bubbles were identified using ammonia traces and hot-wire measurements over a wide range of angles of attack but at lower blade tip Reynolds numbers ($Re_{\text{tip}} = 2.6 \times 10^4 - 1.9 \times 10^5$). The lower Reynolds numbers in those studies leave some uncertainty with respect to the transition mechanism in [151]. Near the blade tip, Tanner and Yaggy found transition positions further upstream on the blade suction side and further downstream on the corresponding pressure side when compared to radial positions further inboard. The finding persisted at higher collective pitch angles. The effect was attributed to the contraction of the tip vortex behind the blade, as sketched in Fig. 1.16a, causing a change in the radial lift distribution as evidenced by the measured sectional lift which is shown in Fig. 1.16b.

McCroskey's results from Ref. [96] are summarized in Fig. 1.17a. Measured chordwise positions of laminar separation and transition in the rotating frame are compared against results obtained from non-rotating measurements and theoretical calculations from [29] for different angles of attack. At $Re_{\text{tip}} = 5 \times 10^4 - 2 \times 10^5$, boundary-layer transition on the NACA 0012 rotor blade suction sides, referred to as "series 1", was triggered by laminar separation bubbles. This was
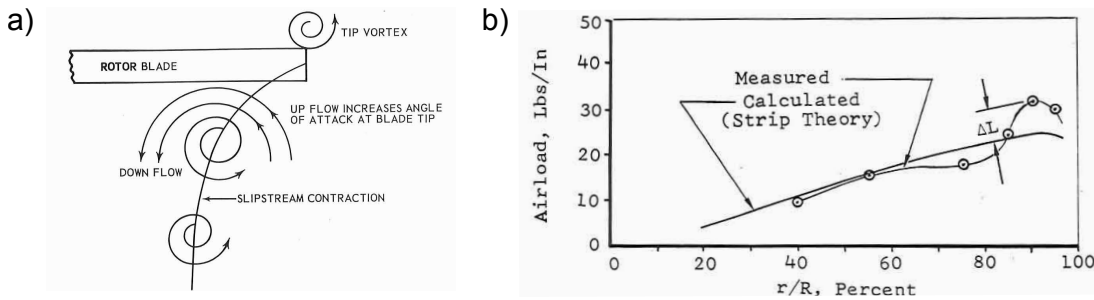
Figure 1.16: Figures from Tanner and Yaggy [151] explaining radial change of measured transition positions close to the blade tip: *a)* Sketch of rotor blade slipstream showing wake contraction and vortices *b)* Comparison of measured and calculated radial lift distribution.

inferred experimentally from ammonia trace separation patterns as well as hot wire measurements and theoretically from the agreement to results from Dwyer and McCroskey [29]. The results from [29] are depicted by the lines corresponding to "Ref. 7" in Fig. 1.17a. The measured data was averaged between 60 - 80 % radius as the change in between was negligible. This corresponds to Rossby numbers of $Ro = r/c = 4.3 - 5.8$, with Ro being identical to r/c in hover (see Eq. 1.22).

McCroskey [96] also studied boundary-layer transition on the "series 3" blades, which comprise a NACA 0012 - type leading edge but with a relatively thinner and flatter downstream part. According to McCroskey [96], the results depicted by the shaded band in Fig. 1.17 include data from both rotating and non-rotating experiments. He therefore precludes that rotational forces have an influence on the measured transition locations for this geometry as well. It is further concluded that at $\alpha < 6°$ transition on the "series 3" blades occurs naturally, not being triggered by a separation bubble, since the measured transition positions are significantly upstream of the theoretical separation lines in the same graph which however correspond to the (different) original NACA 0012 airfoil. In turn, the separation characteristics of the "series 3" blades are not explicitly stated. It should also be noted that detailed analysis of the non-rotating "series 3" data from the same study (see Fig. 1.17b) reveals transition positions of 10 - 15 % upstream of the positions detected on the corresponding rotating blades expressed by the shaded band in Fig. 1.17a. This is in contrast to what is stated in [96]. For these reasons, an ambiguity with respect to the "series 3" results persists on both, the transition mechanism and on an asserted exclusion of a rotational effect on the transition position.

Nevertheless, for the cases where transition was triggered by laminar separation bubbles close to the leading edge on the NACA 0012 and NACA 0015 airfoils it was shown in [151] and [96] that measured transition positions are comparable to the two-dimensional case and mostly driven by alternating pressure gradients at varying angles of attack. This is in line with the results from Banks and Gadd [7] or Dumitrescu and Cardos [28] who found that rotational effects with respect to laminar separation are lowest in regions of strong adverse pressure gradients.

The other experimental studies mentioned above in Sec. 1.2.2 did not explicitly tackle the effect of rotational forces. Rohardt [124] and Beaumier et al. [9] measured boundary-layer transition on the upper and lower side of a BO105 and on a Dauphin helicopter rotor, both at full scale and in
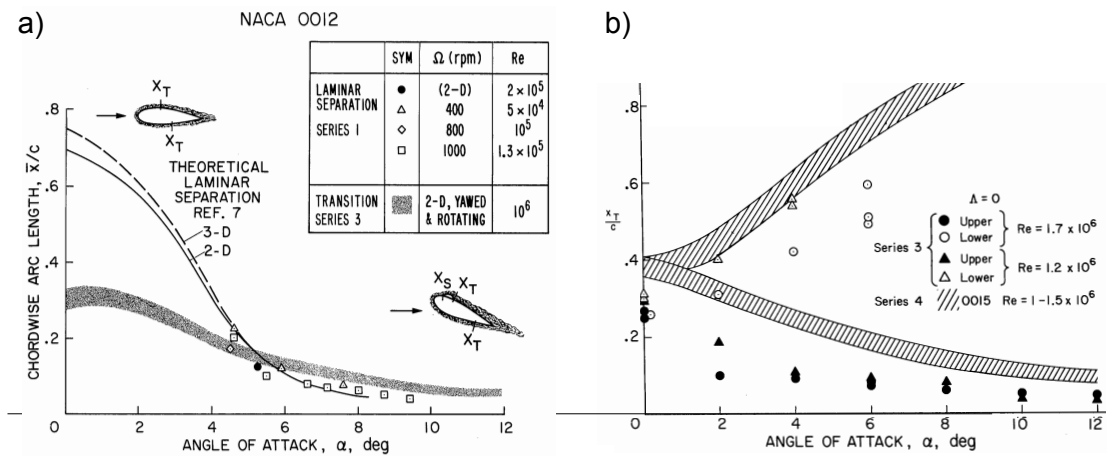
Figure 1.17: Figures from McCroskey [96]: *a)* Summary of separation and transition results on rotating blades. The shaded band is noted to comprise rotating transition data of "series 3" blade (modified NACA0012) and non-rotating data as depicted on the right handed graph. *b)* Chordwise transition positions on non-rotating "series 3" blade in symbols.

hover. They found $\sim 20 - 25\,\%$ laminar flow on the blade suction sides and $\sim 70 - 75\,\%$ on the corresponding pressure sides. It was reported in both studies, similarly as in [121] and [122], that laminarity slightly decreased when observing radial positions further outboard. The decrease of laminar flow at locations further outboard was especially observed for moderately twisted blades at comparatively low collective pitch angles. The effect was be attributed to an increased relative chord Reynolds number. The main parameter influencing the transition position was the collective pitch angle. Due to the resulting change of the pressure distribution boundary-layer transition moved upstream on the suction side and downstream on the pressure side as the collective pitch was increased.

Transition data, obtained via acenaphtene coatings in a flight test with a full scale hovering BO105 helicopter [124], was used in [55] for validation purposes of the transition prediction tool developed by Heister [57]. The tool uses transition criteria, which are based on empirical correlations obtained from transition experiments on purely translating aerodynamic surfaces. In this respect approximate equations relate local integral boundary-layer quantities, which are for example based on δ_2 and obtained from the numeric solution, to empirically found transition positions. Empirical criteria have been formulated for different transition mechanisms and implemented by Heister into a 3D Navier Stokes solver. For the data point investigated in [55], Heister achieved overall close agreement to the measured positions at $r/R > 0.6$. He further identified laminar separation and Tollmien-Schlichting instabilities as the most dominant transition mechanism especially on the blade suction side. Areas close to the blade root and tip were identified to be affected by bypass transition due to blade-vortex interactions with the preceding wakes. Heister also found that if laminar-turbulent boundary-layer transition was considered for the rotor in hovering flight, the required power would decrease by $4\,\%$ compared to calculations with a fully turbulent boundary-layer.

Richter and Schülein [121] complemented their transition measurements via IR on the suction side

of a Mach-scaled BO105 rotor by 2D computations obtained from MSES and the implemented approximate e^N-method for transition prediction. Comparisons of qualitative surface temperatures and the detected transition region to the respectively calculated c_f-distributions and the predicted transition positions showed good agreement supporting the validity of the data and methods used. The comparison was provided for six data points obtained at varying rotating frequency and constant collective pitch.

Richter et al. [122] simultaneously measured boundary-layer transition on the upper and lower sides of a full scale BK-117 helicopter rotor (see Fig. 1.12). The measurements were complemented by state of the art numerical simulations including empirical criteria for different transition mechanisms using the method developed by Heister [55, 56]. Good qualitative agreement in the radial development of boundary-layer transition was obtained between measured and calculated results. In the simulations, transition was mainly attributed to 2D Tollmien-Schlichting- and or laminar separation induced transition. Despite the qualitative agreement, significant quantitative deviations were observed, showing that both experimental transition detection and the numeric technique for transition prediction can be improved. The main causes for the observed deviations were attributed to the overestimated sensitivity of the predicted transition onset with respect to angle of attack and the limited spatial resolution of the transition region as captured by the IR camera.

Recently, Overmeyer and Martin [105] performed comprehensive measurements on the Mach-scaled "PSP rotor", named according to its previous use for validation purposes of PSP measurements [162, 166] (see Fig. 1.3). They measured boundary-layer transition via IR simultaneously on the blade suction and pressure sides along with rotor thrust and torque. In addition to providing a data base for numerical validation, one of the main purposes of the campaign was to experimentally demonstrate the effect of laminar flow on rotor efficiency in hover. This was attempted by comparing the measured performance at natural transition against the fully turbulent case where the boundary layer was artificially "tripped" by transition dots applied to the leading edge. However, difficulties were encountered due to "over-tripping", meaning that excessive drag and premature turbulent separation were introduced. This complicated the comparability of the respectively measured data to fully turbulent simulations and stresses the importance for measurements of natural transition data points for the validation of numeric tools.

Overmeyer and Martin's campaign [105] has been subject to validation of advanced numerical tools, employing transition criteria embedded in transport equations which are either based on Langtry-Menter's empirical model [78] or on the approximate e^N-method [15, 16]. For instance, Jain [62] used a version of the former and the latter was applied by Vieira et al. [157]. Both were capable of qualitatively reproducing most of the measured transition locations with room for improvement of the predicted rotor performance. For the investigated cases, the findings suggest predominantly two-dimensional flow behavior with transition due to Tollmien-Schlichting instabilities and/or laminar separation. In both studies increased deviations to measured data were reported where bypass transition is triggered by incoming flow with increased vorticity and turbulence levels from the wake of the preceding blade.

Boundary-layer stability analysis on rotating blades   Hardly any studies exist where the problem of boundary-layer stability was analyzed in view of the action of rotating forces. In 2012, Martinez-Hernandez [95] performed stability analysis on boundary layers of wind turbine rotor blades under consideration of the rotational terms in the underlying stability equations. The e^N-method was employed for transition prediction, allowing wave propagation in potential streamline direction ψ_p an perpendicular to it. Lacking experimental data for correlation, a critical N-factor of 9 was assumed. His results show that system rotation can have a stabilizing effect on boundary-layer transition, especially at low adverse and favorable pressure gradients close to the hub and at low Reynolds numbers. His findings are reflected for instance in Fig. 1.18a showing the results obtained on the suction side of a NACA 0015 airfoil. Relative streamwise transition positions are plotted against the propagation angle of disturbances for four Reynolds numbers and three relative radial positions expressed as c/r. As defined in the sketch on the right in Fig. 1.18b, the propagation angle gives the direction of the vector whose components correspond to the disturbance wavenumber in streamwise direction, denoted as α_r, and perpendicular to it, denoted as β_r.

In a more recent work, Dechamps and Hein [18] extended the numerical code NOLOT [53] to enable stability analysis of boundary-layer flows in rotating reference frames. The examined cases were a Blasius boundary layer, rotating around its transverse axis, a Görtler flow over concave rotating surfaces and the flow on a rotating disc exposed to varying axial inflow. The code was successfully validated for these academic examples, as the results converged to the analytic solutions. However, it has not been applied yet to a realistic configuration like a helicopter rotor in hover. This would allow the isolation of the effect of rotational forces on the stability of the boundary layer and a detailed investigation of the underlying transition mechanisms.
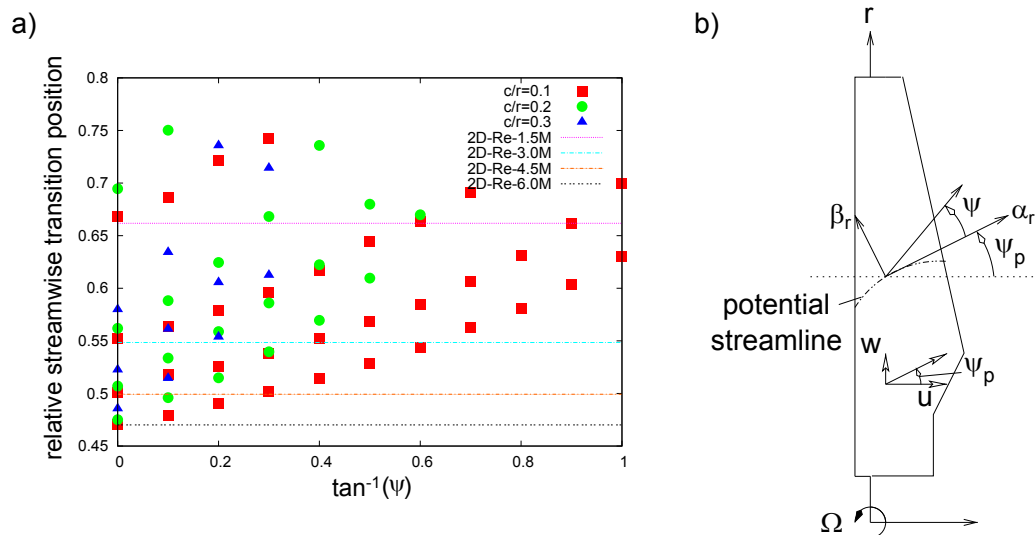
Figure 1.18: *a)* Streamwise transition position against propagation angle of disturbances Ψ on a rotating NACA 0015 airfoil *b)* Definition of Ψ (mod. from Martinez Hernandez et al. [95]).

1.3   Scope of work and thesis objectives

In this thesis, integral and surface air-loads as well as boundary-layer transition are investigated on a Mach-scaled helicopter blade configuration in climb.

The work comprises two parts:

i) The presentation of an optimized pressure-sensitive paint (PSP) system for global surface pressure measurements on fast rotating blades and its application to the investigated configuration with the following goals:

   a) Reduce error sources originating from rotational image blur and from possible cycle-to-cycle variations of inhomogeneous excitation light sources

   b) Identify characteristic aerodynamic flow features by analysis of global surface pressure maps on the rotor blades

   c) Assess the capability of the technique to measure instationary flow phenomena, for instance due to stall

ii) Boundary-layer transition measurements via temperature-sensitive paint (TSP) (and for comparison via infrared (IR) thermography) on the same configuration as for the PSP campaign with the following goals:

   a) Establish an experimental data base for validation purposes of advanced numerical codes employing transition prediction capabilities

   b) Investigate the effect of rotational forces on measured boundary-layer transition positions

   c) Compare experimental data to two-dimensional (2D) numerical simulations in order to evaluate the prediction capabilities of 2D local linear stability theory (LST) methods, by correlating critical N-factors with measured boundary-layer transition data

2 Surface pressure investigations[1]

The following chapter presents the application of an advanced pressure-sensitive paint measurement system to a model scale helicopter blade configuration. An optimized image acquisition technique to reduce image blur in single-shot PSP lifetime measurements on fast rotating blades is presented. After demonstrating the working principle and the characteristics of the measurement system, its capability to efficiently reduce blur is presented. The system is then applied to measure surface pressures on the suction side of a Mach-scaled helicopter blade in climb. Following a description of the experimental setup the post-processing procedures are presented, including measures to correct for temperature effects in the PSP data. Surface pressure results are presented and discussed for different rotating speeds and at various collective pitch settings before the measurement uncertainty is assessed.

2.1 Pressure-sensitive paint measurement system

The measurement system components used in this work are sketched as a principle test setup in Fig. 2.1.
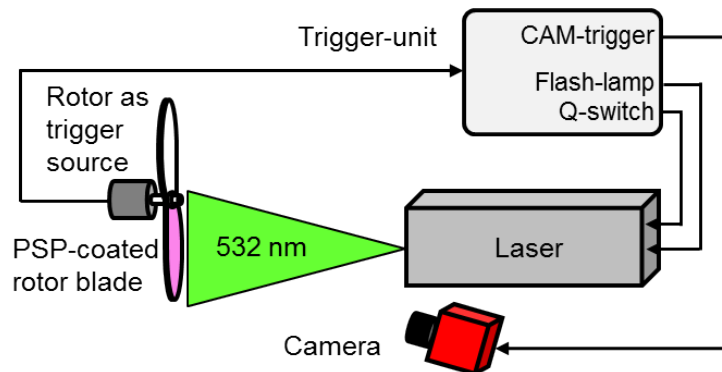
Figure 2.1: Sketch of PSP-lifetime system components

The pressure-sensitive paint employed is platinum tetra(pentafluorophenyl) porphyrin (PtTFPP, see [116]) embedded in a poly(4-tert-butylstyrene) polymer binder (poly(4-TBS), see [171]). A laser system consisting of four neodymium-doped yttrium-aluminium-garnet (Nd:YAG) lasers (*Quantel, BigSky CFR-400*) is used to excite the dye at a wave length of 532 nm [116]. The key component of the measurement system is a modified version of the scientific grade digital CCD camera *FoxCam4M* recently presented by Geisler [41, 42] and now further developed for single-shot PSP lifetime applications on fast rotating blades. For synchronization of camera and light source with the PSP-coated rotor blade, a commercially available and programmable pulse sequence generator (*Hardsoft, Sequencer V5.1*) is used as triggering unit.

2.1.1   Optimized double-shutter camera

The recording of two (or more) short-exposure frames in fast succession is limited by the technology of available image sensors. High-speed complementary metal-oxide-semiconductor (CMOS) sensors were used previously by Mebarki and Benmeddour [99], who applied a scientific CMOS camera for single-shot lifetime measurements on a slowly moving model. For the present application however, exposure times below 10 μs are required being equivalent to a recording rate of more than 100 000 fps. Currently, image sensors reaching these frame rates provide only a limited spatial resolution. Similar requirements are familiar from flow measurements with particle image velocimetry (PIV). For this, a new readout mode *Framing-Optimized Exposure (FOX)* for off-the-shelf CCD image sensors was recently presented [41, 42]. FOX provides two short exposed frames in fast succession. Both frames exhibit a binning-like reduced resolution and are completely congruent without insensitive lines or interlace-like artifacts. Because the second frame has a different exposure time for even and odd numbered pixel lines, the FOX readout mode is not suitable for luminescence lifetime measurements. For this purpose explicitly defined exposure times are required, whereas insensitive lines in principle are acceptable. Therefore, a different readout scheme is necessary.

The standard readout scheme for interline-CCD image sensors is depicted in Fig. 2.2. First the photo diode content is cleared (Fig. 2.2a. The photo diodes then accumulate photo electrons released by the incoming light (Fig. 2.2b. After the exposure time for the first frame the accumulated photo electrons are transferred to the light-shielded vertical register (Fig. 2.2c). Subsequently the register content is read out serially by one (or more) analogue-to-digital (A/D) converters (Fig. 2.2d). This is a slow process with a resolution-dependent duration in the millisecond range. Immediately after the transfer of the charges to the vertical register the photodiodes again start to accumulate photo electrons. Once the readout process is completed, these new charges optionally can be transferred to the now empty vertical register (Fig. 2.2e) and read out (Fig. 2.2f). As a result, a second frame with an exposure time of at least the frame readout time is recorded in direct succession of the first frame. This two frame readout scheme is commonly known as "double shutter" mode.

The readout scheme used in the present measurements can overcome the disadvantageous long exposure time of the second frame in double shutter mode. In this case only the charges of every second photo diode row are transferred to the vertical register after the exposure of the first frame (Fig. 2.3b) whereas the remaining photo diodes are ignored (crossed out in the sketch). Therefore half of the potential wells forming the vertical register cells remain still empty (Fig. 2.3c). The potential wells are shifted by one line (Fig. 2.3d) and take along the contained charges. Thus the empty register cells are located next to the photo diodes used in the first frame. This process takes only several microseconds posing a lower limit to the exposure time of the second frame of ~5 μs. Hence, the newly accumulated charges of the very same photo diodes can be transferred to these empty register cells after a very short exposure time for the second frame (Fig. 2.3e). The two frames are then stored in a line-interleaved pattern within the vertical register (Fig. 2.3f) and can be read out analogue to the common way (Fig. 2.2d,f). Finally the frames are separated again from the line-interleaved pattern to single frames by software.

In summary, the two captured frames are completely congruent and have an explicitly defined
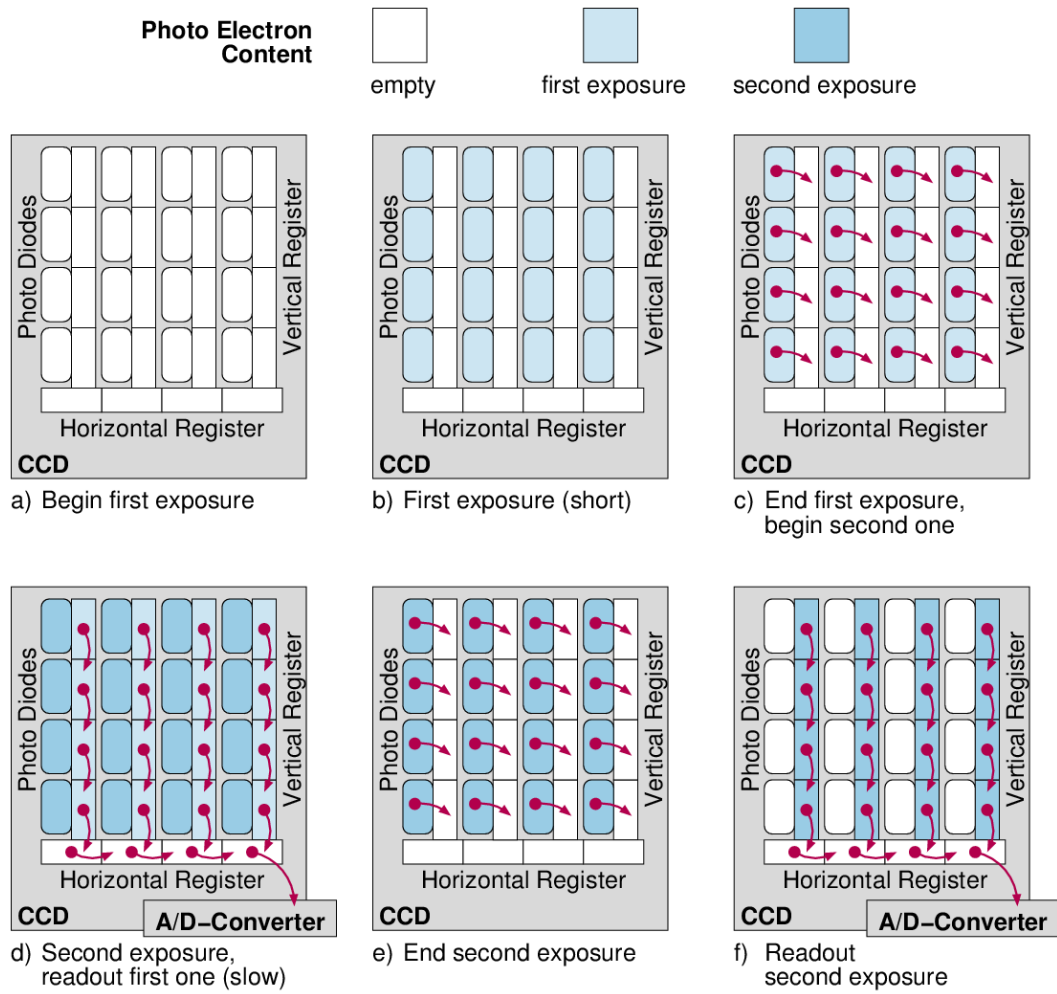
Figure 2.2: CCD image sensor readout scheme in normal mode, a)-d), and double shutter mode, a)-f).
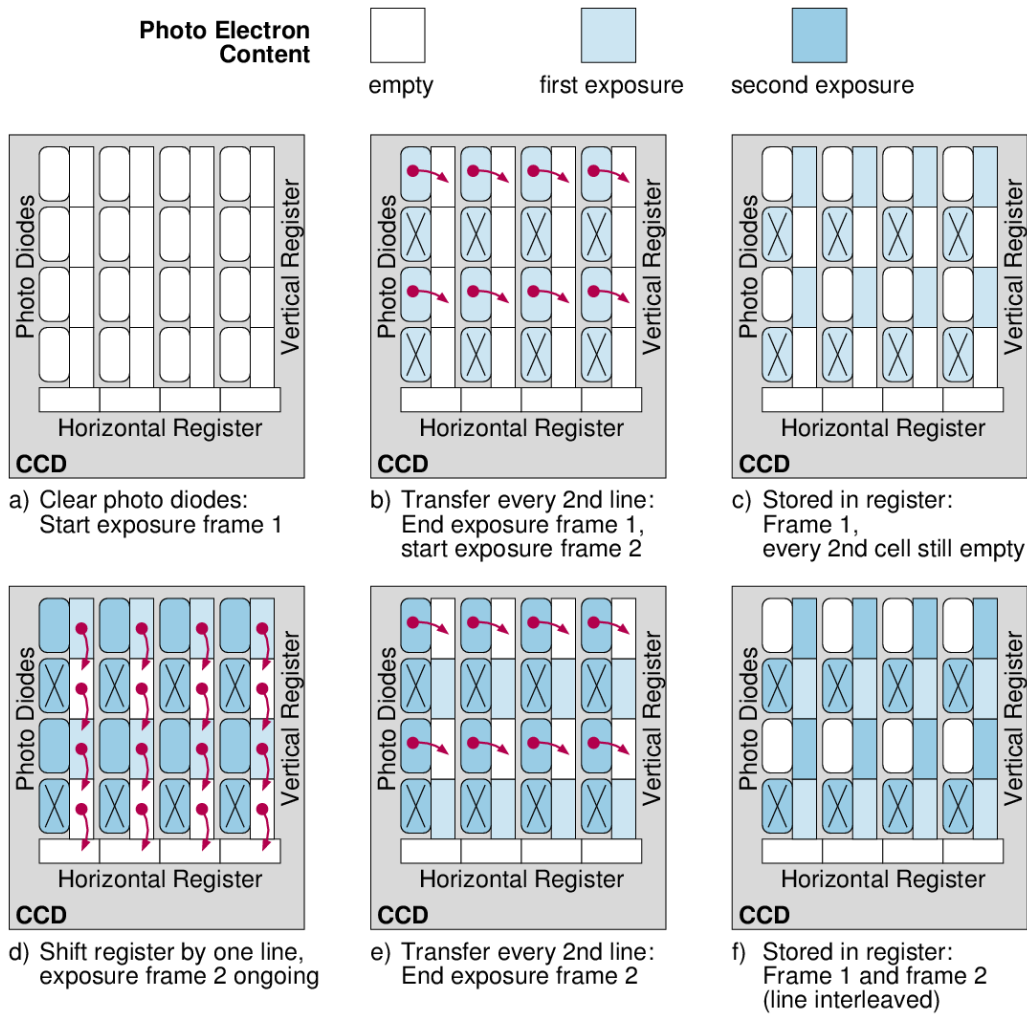
Figure 2.3: CCD image sensor readout scheme in the luminescence lifetime imaging mode used for the present measurements.

short exposure time both of which are essential for lifetime imaging. The frames are exposed in direct succession with a very short (nanosecond range) frame transition time defined by the transfer process to the vertical register (Fig. 2.3b). Only half of the photo diode rows are used, i.e. every second image row is insensitive which bisects the effective image readout resolution. This modified readout scheme was programmed to the firmware of the 4 megapixel camera *FOXCam4M* presented by Geisler [42]. In general, it can be implemented in all cameras equipped with an image sensor whose even and odd pixel lines can be addressed separately. This requires at least an adapted firmware and/or eventually severe changes in the hardware. For the presented experiments a commercial camera based on the *Kodak / ON Semiconductor KAI-4021* image sensor has been modified with in-house hardware adaptations including a separate firmware layer. More specific details are described by Geisler [43]. The modified camera properties are given in Tab. 2.1.

Table 2.1: Properties of *FoxCam4M* in lifetime mode

Sensor resolution	2048×2048 px
Effective readout resolution	2048×1024 px
Exposure time 1st frame ($G1$)	customizable to $\geq 5\,\mu s$ (typ.)
Exposure time 2nd frame ($G2$)	customizable to $\geq 5\,\mu s$ (min.)
Frame transition time	< 200 ns
Max. (double) frame rate	15 Hz
A/D dynamic range	12 bit

A principle timing chart of the system components is provided in Fig. 2.4. Assuming that a trigger signal is provided by the rotor, a delay (preferably a phase shift) needs to be set with respect to the camera trigger in order to position the rotating blade in the camera field of view. The phase-shifted signal then triggers a sequence for both laser and camera. Considering the internal camera delay (set to $10\,\mu s$) the parameter $\Delta t_{G1\rightarrow laser}$ defines the timing between the excitation pulse and the beginning of the first exposure ($G1$). Positive values of $\Delta t_{G1\rightarrow laser}$ mean that the laser pulses within the first frame. Because the pressure-sensitive signal immediately reacts to the excitation pulse, the key timing parameters determining the measured dye properties are the exposure lengths $G1$, $G2$ and $\Delta t_{G1\rightarrow laser}$. If the data acquisition rate $f_{acq.}$ (limited by either laser or camera) is lower than the rotating frequency of the blades (f_{rotor}), an idle time (t_{idle}) needs to be implemented to the trigger sequence in order to synchronize the rotating speed with laser and camera for phase-locked imaging. In the present study, the limiting system component is the laser. Being preferably pulsed at 10 Hz, t_{idle} was set to 95 ms.

2.1.2   Pressure-sensitive paint lifetime characteristics

The PSP employed in this study (PtTFPP in poly(4-TBS)) has been used previously for PSP-lifetime measurements on fast rotating blades by Klein et al. [70]. The normalized emission spectrum (at $\lambda_{ex} = 512\,nm$) and excitation sensitivity (at $\lambda_{em} = 650\,nm$) are plotted in Fig. 2.5. Its
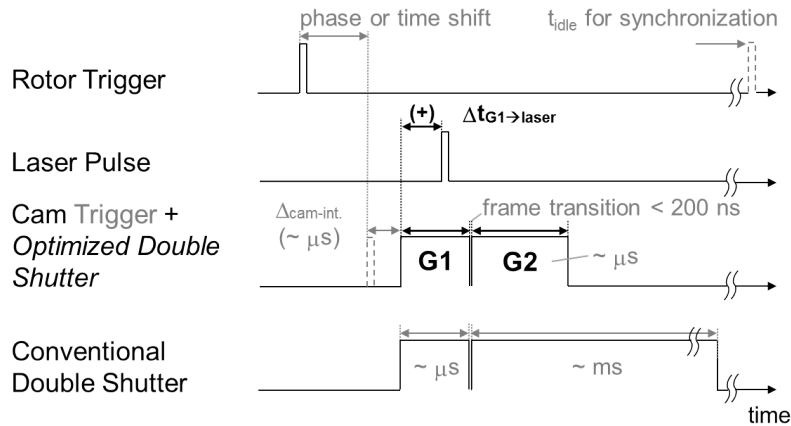
Figure 2.4: Principle trigger sequence for optimized double shutter PSP lifetime system applied to rotor testing

characteristics under ultra violet light emitting diodes (LEDs) excitation were recently studied by Yorita et al. [171] and compared to a measurement system based on laser excitation in [172]. In the following the pressure and temperature sensitivies are investigated for different settings of the timing parameters as outlined in Fig. 2.4 and considering dye excitation by a laser at 532 nm.
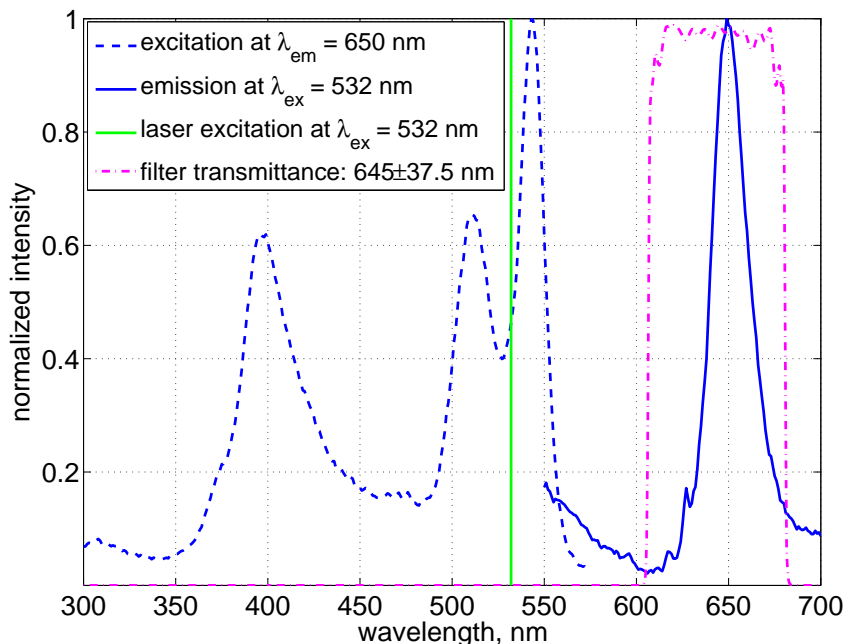
Figure 2.5: Spectral characteristics of PtTFPP in poly(4-TBS) and transmittance of band-pass filter used in the measurements.

A small coupon was prepared with the same coating layer setup as used in the wind tunnel test. A matte white foil (*3M Wrap Film Series 1080*, ~100 μm) is used as base layer to enhance the luminescent signal. Before applying the PSP an intermediate layer of boron nitride dissolved in
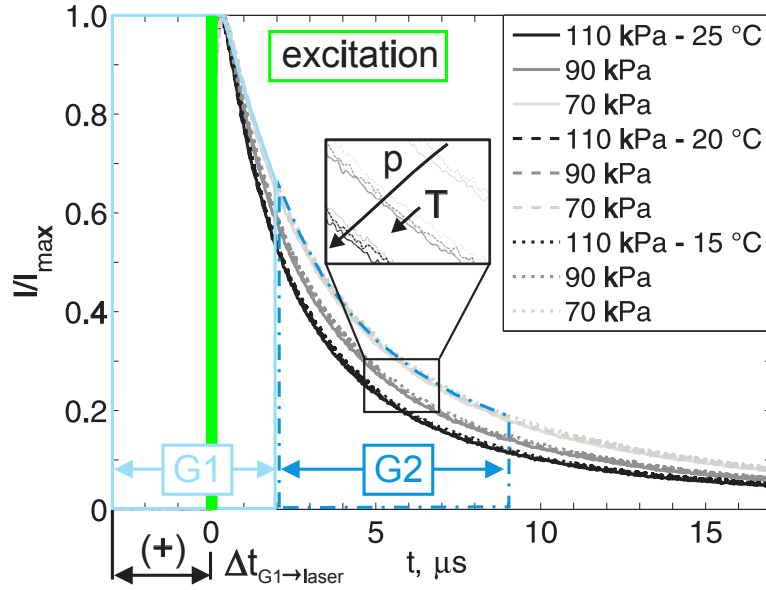
Figure 2.6: Lifetime decay curves and schematic of integration gates $G1$ and $G2$. $\Delta t_{G1 \to \text{laser}}$ is positive when excitation is pulsed during $G1$.

the same polymer as the PSP is used (see also [171]) to avoid any unwanted interactions between the active layer and the foil. A photo multiplier tube (PMT) was used to measure the luminescence lifetime of the employed PSP sensor after pulsed excitation (10 Hz) at 532 nm by the laser mentioned above. A 650 ± 40 nm band pass filter was used to separate the emitted light from the excitation pulse. The PMT signal was recorded by a digital oscilloscope at a sampling rate of 50 MHz for a total of 20 µs and ensemble averaged over 128 cycles. The sample was calibrated in a pressure- and temperature controlled chamber. Lifetime decay curves were obtained for pressures from $p = 70$ to 120 kPa ($\Delta p = 10$ kPa) and for temperatures of $T = 15$, 20 and 25 °C, respectively. Selected decay curves are presented in Fig. 2.6, where all intensities are normalized by the peak value and plotted against time. As expected, the decay rate is faster with both increasing pressure and temperature and the change in pressure has greater influence on the decay time within the depicted parameter range.

For further analysis the normalized intensity values are integrated over two adjacent gates, $G1$ and $G2$, as sketched in Fig. 2.6. The integration time $G1$ is chosen to be 5 µs and the timing parameters to be optimized are the delay between the start of $G1$ and the laser pulse, $\Delta t_{G1 \to \text{laser}}$, as well as the length of the second integration gate, $G2$. Note that the effective first exposure is reduced if the excitation light is pulsed within $G1$, i.e. for positive values of $\Delta t_{G1 \to \text{laser}}$. The ratio of the integrated intensities, I_{G1}/I_{G2}, is then normalized with the ratio at reference condition (100 kPa, 20 °C) and evaluated as ratio of ratios (RoR, see Eq. 1.1). Pressure- and temperature sensitivities s_p and s_T are defined as:

$$s_p = \frac{\Delta RoR}{\Delta p} \cdot 100 \qquad (2.1)$$

$$s_T = \frac{\Delta RoR}{\Delta T} \qquad (2.2)$$

Table 2.2: Pressure- and temperature sensitivities for different gate settings at $100\,\mathrm{kPa}$, $20\,^{\circ}\mathrm{C}$.

$G1|G2$, µs	$\Delta t_{G1\rightarrow\text{laser}}$, µs	s_p, %/100kPa	s_T, %/K
5|5	+3.0	56.7	0.34
5|7	+3.0	61.2	0.37
5|10	+3.0	66.8	0.39
5|7	+1.5	62.0	0.34
5|7	-1.5	38.7	0.18
5|7 (*FoxCam4M*)	+3.0	55.3	0.40

The evaluated parameter range and the corresponding sensitivity results are summarized in Tab. 2.2. The following main conclusions can be drawn:

1. s_p increases with increasing $G2$

2. s_p decreases for $\Delta t_{G1\rightarrow\text{laser}} < 0$, i.e. start of $G1$ follows the excitation pulse

3. The influence of $\Delta t_{G1\rightarrow\text{laser}}$ on s_p is small for $\Delta t_{G1\rightarrow\text{laser}} > 0$

In view of a rotor test application, the length of $G2$ must be an optimum between high pressure sensitivity at long exposures and a small remaining extent of image blur at short exposure times. Moreover, it is desirable that the intensity levels of both gates are similar in order to reduce the effect of shot noise on the divided ratio image. This can be achieved by adopting $\Delta t_{G1\rightarrow\text{laser}}$ accordingly, e.g. $\Delta t_{G1\rightarrow\text{laser}} = +3\,\text{µs}$ for $G1|G2 = 5|7\,\text{µs}$.

To confirm the PMT findings, the coupon was also calibrated, using the *FoxCam4M* at exposure times of $G1|G2 = 5|7\,\text{µs}$ and a delay of $\Delta t_{G1\rightarrow\text{laser}} = +3\,\text{µs}$. In Fig. 2.7 the normalized gate ratio is plotted against pressure for both the data obtained by the camera and the reference PMT measurements at $T = 20\,^{\circ}\mathrm{C}$. The error bars indicate the propagated measurement uncertainty averaging 128 images to obtain each of the four gate intensities used for the ratio of ratios calculation (Eq. 1.1). It can be deduced from the graph that the images recorded by the camera produce the expected results. Possible reasons for deviations include that the manner of integrating the luminescence signal differs between the analysis of PMT data and camera image acquisition.

2.1.3   Initial proof-of-concept

A laboratory study was conducted to demonstrate both system feasibility and the influence of different exposure times of the second gate on the blur of the resultant images. For this, a two bladed, wooden model propeller (*EM-Elektro*) was used. The propeller has an outer diameter of $0.35\,\text{m}$ at $0.23\,\text{m}$ pitch. Instead of the foil used for calibration, a white, acrylic based screen layer (*Tamiya PS-1*) was applied on one of the blades before coating the same intermediate and PSP layers as described in the previous section. The test setup corresponds to the sketch in Fig. 2.1.
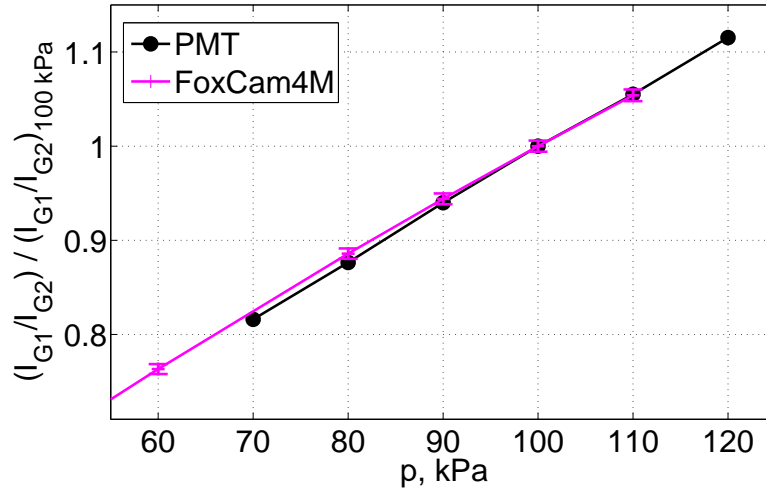
Figure 2.7: Calibration results obtained by *FoxCam4M* vs. PMT-data at $T = 20\,°C$; $G1|G2 = 5|7\,\mu s$; $\Delta t_{G1\rightarrow\text{laser}} = +3\,\mu s$.

The camera and light source were placed ~4 m in front of the propeller in order to simulate larger wind tunnel facility dimensions. A *Sonnar* lens with a focal length of 180 mm and an aperture opening of $f/2.8$ provided images of the propeller blade at a chordwise resolution of 4.6 px/mm for a tip chord length of 12 mm. A 650 ± 40 nm band-pass filter was used to separate the excitation light from the measured luminescence. Details about the propulsive unit and the 1/rev-trigger generation are described by Yorita et al. [170] and Klein et al. [70] who used a similar setup. The 1/rev. signal was phase-shifted to position the blade within the camera image. The shifted signal was then directed into the triggering unit which generated a sequence as sketched in Fig. 2.4 to control the timing between camera and laser. The laser system was operated at 200 mJ/pulse and the rotation rate of the propeller was set to 90 Hz corresponding to tip velocities of ~100 m/s. Choosing a $G1$-exposure of 5 µs and a delay of $\Delta t_{G1\rightarrow\text{laser}} = +1.5\,\mu s$ the study was performed for $G2$-lengths of 5, 7, 10 and 100 µs. The latter was chosen to be fairly larger than the lifetime of the PSP sensor ($\tau_{0.1 I_{\max}} = 12\,\mu s$ at 100 kPa, 20 °C) in order to simulate the second exposure of a conventional CCD camera in double-shutter mode. The delay $\Delta t_{G1\rightarrow\text{laser}}$ was chosen to balance image intensities between the first exposure ($G1 = 5\,\mu s$) and the second exposure ($G2 = 5 - 100\,\mu s$). Note from Tab. 2.2 that the effect of different positive delays on pressure sensitivity is small.

The self-referencing character of the single-shot lifetime method is demonstrated in Fig. 2.8, showing the coated model propeller blade at rest. In the left column images corresponding to $G1$ and $G2$ are taken at different excitation cycles, whereas on the right hand side both images are acquired in direct succession after excitation with the same laser pulse. Note the arbitrary Schlieren and speckle pattern from the excitation light in each of the gated images. While a structure persists in the ratio image of the former case, the pattern is canceled out after division of the images acquired during the same excitation cycle.

A series of the resulting $G2$-exposures is presented in Fig. 2.9. Cut-outs of raw images are displayed, showing the blade tip. From the viewer's perspective the rotational sense is counter-

I_{G1}

I_{G2}

I_{G1}/I_{G2}

from different excitation cycles   from same excitation cycle
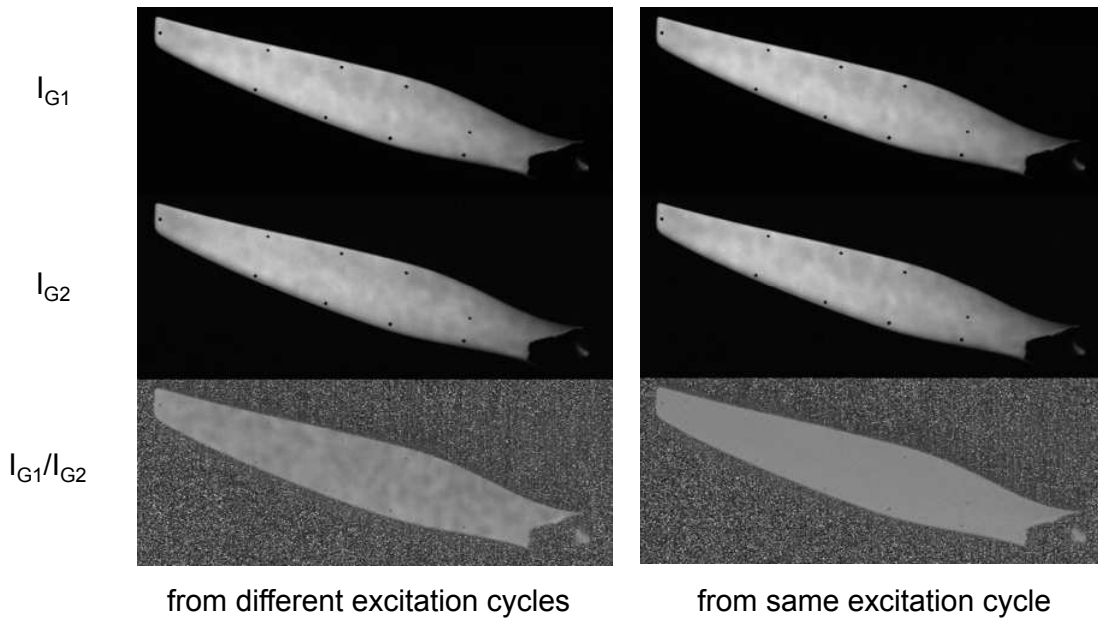
Figure 2.8: Demonstration of self-referencing using the single-shot lifetime PSP method (modified from [172]).

clockwise. In order to facilitate the visual perception of the resultant blur, a black round dot was painted close to the tip. The image on the left hand side was acquired with the propeller at rest for $G2 = 7\,\mu s$. It serves as a reference exhibiting a sharp contrast around the marker and alongside the blade edges. In contrast, the image simulating the second exposure of a conventional CCD double shutter camera with $G2 = 100\,\mu s$ is presented on the right hand side of the figure. A dark trace is visible in the vicinity of the marker in addition to the smoothed out blade edges. The pattern is similar to the blurred images recorded for instance by Gregory et al. [51] (see Fig. 1.4 and Fig. 1.5).

| $G2 = 7\,\mu s$ | 5 μs | 7 μs | 10 μs | 100 μs |

no rotation $u_{tip} = 100$ m/s; rotation is counterclockwise
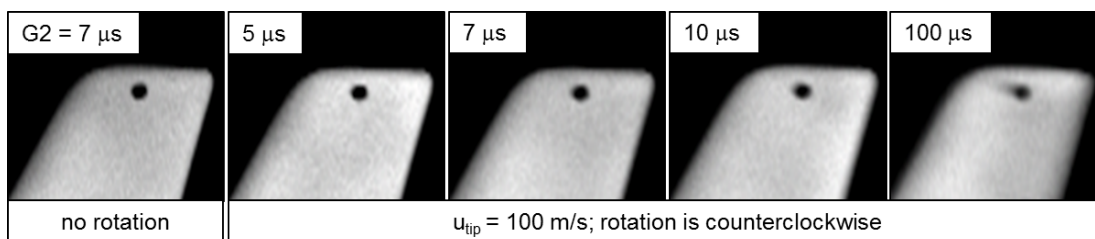
Figure 2.9: Images of propeller tip from second exposure of optimized double shutter mode for different exposure times $G2$. The colormap is centered to include 95 % of the count values.

Comparing the results for $G2 = 5, 7$ and $10\,\mu s$ with $G2 = 100\,\mu s$ the smear is reduced significantly showing the capability of the *FoxCam4M* to acquire sharp $G2$-images when applying the single-shot PSP-lifetime technique. A residual but gradually increasing blur can be observed with increasing

exposure time. The distance swept by the blade tip at $f_{\text{rotor}} = 90\,\text{Hz}$ and $G2 = 7\,\mu\text{s}$ is $\Delta x = 0.7\,\text{mm}$ corresponding to 3.2 px or 5.8 % chord in this case. Using the optimized double shutter technique of the *FoxCam4M*, image blur is inherently limited to only a few pixels for both successively acquired images (I_{G1}, I_{G2}). Therefore, presuming that the signal recorded during both gated exposures suffices, the use of de-blurring algorithms or image de-rotation techniques can be omitted. A resultant $G1$-image is not shown because the effective exposure is even shorter than $5\,\mu\text{s}$ due to the delayed excitation pulse during $G1$, which results in less residual blur than for $G2$.

To conclude, the choice of the optimum $G2$-width should be short enough to limit image blur within an allowable maximum. Within the application specific tolerance, a longer $G2$ is favorable as it provides both greater pressure sensitivity (see Sec. 2.1.2) and higher signal intensity. However, it should be considered that the intensity gain is not directly proportional to the second exposure time due to the lifetime decay (see Fig. 2.6).

2.2 Application to rotating helicopter blades in climb

2.2.1 Facility and model description

The measurements were conducted in the rotor test facility at the German Aerospace Center (DLR) in Göttingen [141, 142]. As illustrated in Fig. 2.10 and Fig. 2.13, the rotor axis is placed horizontally in the open test section of the Eiffel-type facility and the rotational plane faces the square nozzle outlet ($1.6\,\text{m} \times 1.6\,\text{m}$) at a distance of $\sim 1.2\,\text{m}$ (i.e. $\sim 1.8\,\text{R}$). The maximum allowable rotating speed is $f_{\text{rotor,max}} = 50\,\text{Hz}$. A defined low speed axial inflow of maximal $v_{\infty,\text{max}} = 14\,\text{m/s}$ can be provided mainly to avoid recirculation and in order to convect the blade tip vortices.
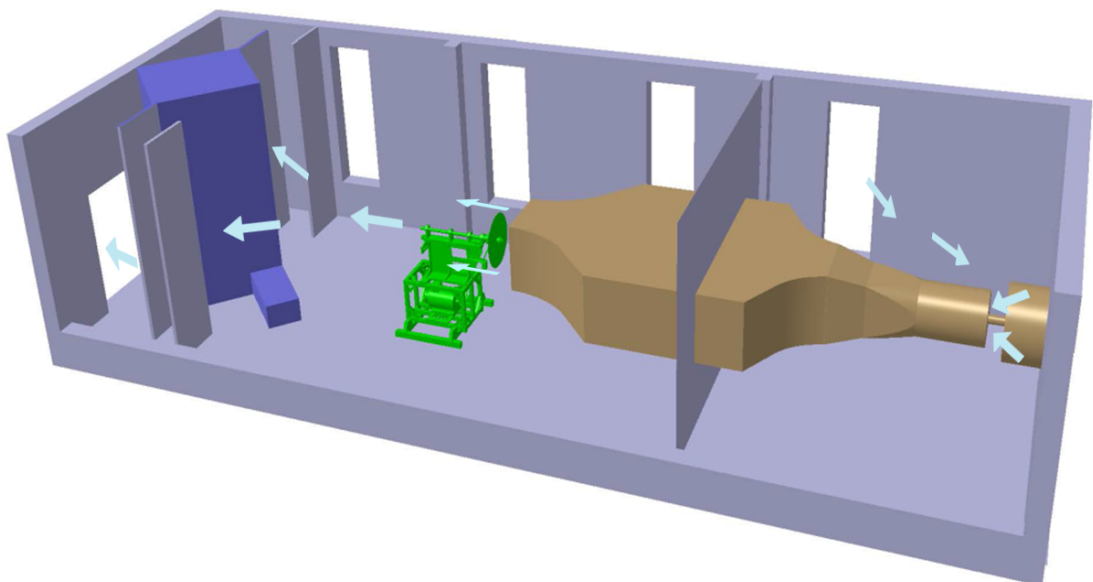
Figure 2.10: Rotor test facility at DLR Göttingen (modified from [141]).

The investigated rotor is equipped with two geometrically identical blades made out of carbon fiber
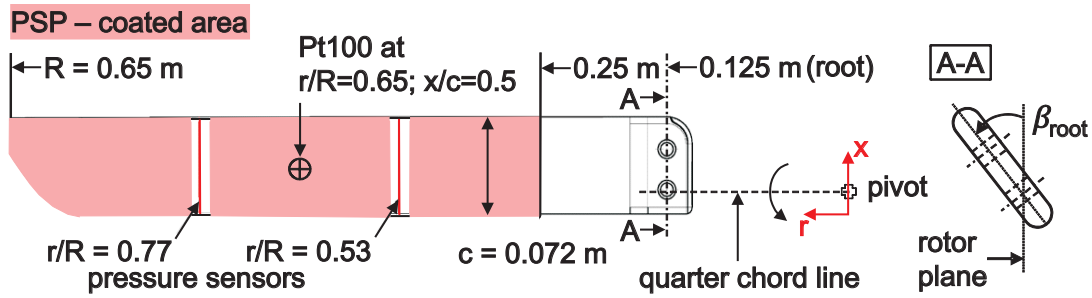
Figure 2.11: *DSA-9A* rotor blade with *SPP8* tip for PSP investigation and definition of root pitch angle β_{root}. Sketch is modified from Schwermer et al. [141] and not to scale.
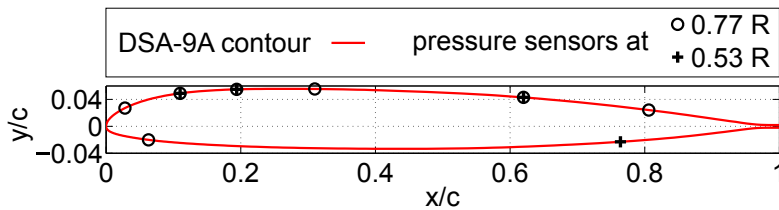
Figure 2.12: *DSA-9A* airfoil (9 % thickness) and positioning of pressure sensors.

reinforced plastic. A plan view of the blades is provided in Fig. 2.11. As indicated, they exhibit a tip radius of $R = 0.65$ m and a chord length of $c = 0.072$ m. A negative linear twist of $-9.33°$ is incorporated along the blade's span between $0.25 < r/R < 1$ with an offset of $-0.67°$ between the blade root and $r/R = 0.25$, i.e. $r = 0.160$ m. The model comprises the *DSA-9A* helicopter airfoil (see Fig. 2.12) and the parabolic shaped *SPP8* tip [159]. In one of the blades fast response pressure transducers (*Kulite LQ-062*) are installed flush to the model surface at two radial positions at $r/R = 0.77$ and 0.53 as indicated in Fig. 2.11 and Fig. 2.12. Surface pressures are provided at a bandwidth of 19 kHz and are averaged over a 10 s time period for each data point. The rotor head allows the adjustment of both the geometric collective and cyclic pitch angles at the blade root (β_{root} as defined in Fig. 2.11). Only the collective pitch was varied equally for both blades and the cyclic was kept to a minimum at $0\pm0.05°$. Therefore, the resulting configuration corresponds to a helicopter rotor in climb or a slowly advancing propeller. The rotating shaft is supported by a 3-component piezoelectric dynamometer (*Kistler 9257B*) which is employed to measure the integral thrust produced by the rotor. The balance readings are sampled at 50 kHz and averaged over 10 s for each data point.

2.2.2 Measurement system installation

The laser was installed below the wind tunnel nozzle as depicted in Fig. 2.13. An arrangement of mirrors and lenses underneath the nozzle outlet redirected the beam towards the rotor in the form of an elliptic spot to ensure full illumination of the coated area. The distance between the optical setup and the illuminated blade was approximately 1.5 m. In order to maximize the luminescence signal the quadruple laser system was operated at a nominal power of 800 mJ/pulse

(4×200 mJ/pulse). The *FoxCam4M* was mounted next to the nozzle outlet at the height of the rotor hub. A 35 mm-*Nikkor* lens was installed under Scheimpflug condition [12], to achieve sharp images across the coated span of the blade (see Fig. 2.13 and Fig. 2.14). With this setup the final spatial resolution is $2.6 - 3.3$ px/mm in chordwise direction with higher values at the blade tip. The Kulite-instrumented blade was coated with the PSP as described in Sec. 2.1.2 and the pressure transducer rows were masked before the coating was applied. An image of the installed and PSP-coated blade is provided in Fig. 2.14 on the right hand side.
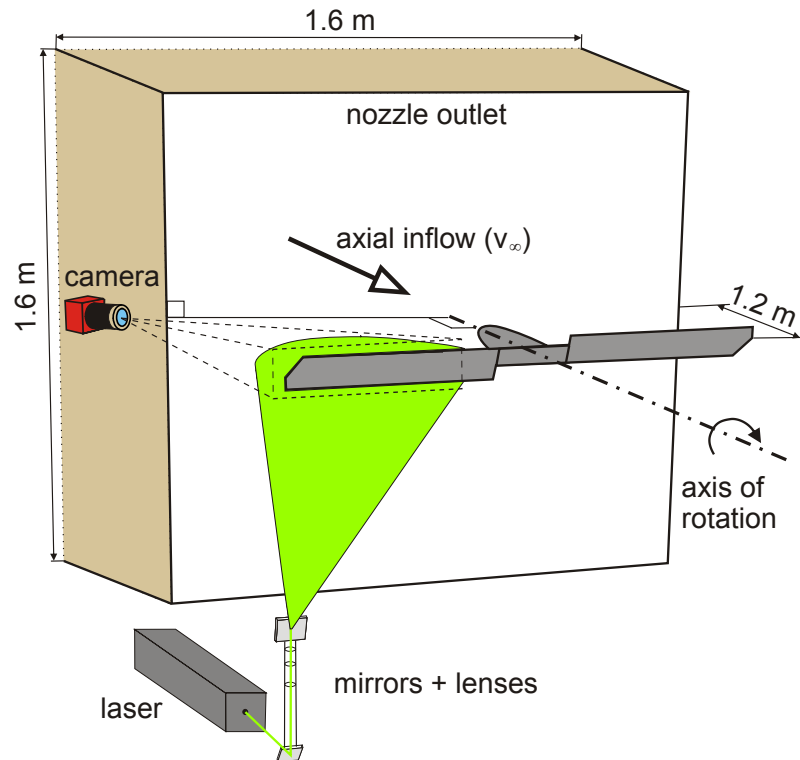
Figure 2.13: PSP setup in the rotor test facility of DLR Göttingen.

Considering the lifetime parameter study of the PSP in view of the configuration investigated, a setting of $G1|G2 = 5|7$ μs and $\Delta t_{G1 \rightarrow \text{laser}} = +3$ μs (see Tab. 2.2, Sec. 2.1.2) was selected in order to get sharp images at high pressure sensitivity and balanced intensity levels between both frames. At a maximum blade tip speed of $u_{\text{tip}} = 193$ m/s ($f_{\text{rotor}} = 47.2$ Hz) the resulting blur pattern for $G2 = 7$ μs is 1.3 mm at the tip corresponding to 1.8 % chord and 4.4 px. Calibration was conducted using the same measurement system as in the test obtaining pressure- and temperature sensitivities of 55.3 %/100 kPa and 0.40 %/K under reference conditions (100 kPa, 20 °C), respectively.

2.2.3 Data acquisition

In the setup described, an encoder was mounted to the rotating shaft providing a 1/rev and a 1000/rev TTL-signal. A custom made selective-trigger-box then allowed to position the rotating blade within the camera field of view as sketched in Fig. 2.13. The positioning was done by
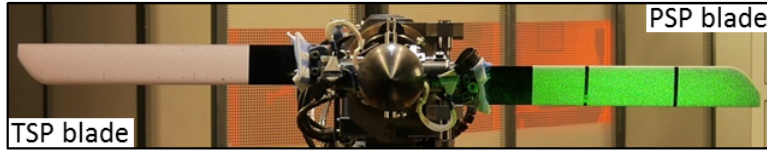
Figure 2.14: PSP- and TSP-coated rotor blades in rotor test facility of DLR Göttingen. PSP-blade is illuminated by laser light at 532 nm.

selecting the appropriate rising edge of the encoder signal and feeding the properly shifted 1/rev-signal as trigger input to the sequencer, which generated the synchronized signals for laser and camera according to Fig. 2.4 using the settings as listed for the *FoxCam4M* in Tab. 2.2.

Initially, *dark* images were acquired under the absence of excitation light and at minimum background illumination. As the rotor was at rest, the blades were set to reference position as sketched in Fig. 2.13 for the acquisition of *wind-off* images. Considering that the blade surface temperature reaches an asymptotic value after adjusting for the desired rotating speed, the time signal of the temperature probe on the suction side of the PSP blade was monitored online to ensure data acquisition under equilibrium condition. In practice, the rotor was running for ~90 s until an asymptotic value was reached and the image acquisition process was started under *wind-on* condition.

For each data point a series of 128 double frames, i.e. pairs of $G1$ and $G2$ images, was acquired in order to increase the SNR by ensemble averaging the single-shot results, respectively. Depending on f_{rotor} = 23.6, 35.4 and 47.2 Hz, the image acquisition rate was limited to every third, fourth or fifth revolution, resulting in acquisition rates of $f_{\text{acq.}}$ = 7.9, 8.9 and 9.4 double frames per second (fps), respectively.

Kulite and Pt100 data are provided at a bandwidth of 19 kHz and balance readings are sampled at 200 kHz. All rotor data were averaged over a period of 10 s. More detailed information about the rotor data acquisition system is provided by Schwermer et al. [142].

2.2.4   Data reduction

After the images were read out a 2×1 binning was applied. This way, the SNR is increased by $\sqrt{2}$ and the original image aspect ratio is recovered (Sec. 2.1.1). All image processing is then performed using the in-house developed software package *ToPas* (as in [69]) according to the following procedure:

1. Subtraction of *dark* signal from all images

2. 2D-image registration: all images acquired under *wind-on* condition are aligned to the first $G1$ image of the series using 23 dot-markers applied to the coated surface; the procedure accounts for rotation and translation within the image plane

3. Calculation of *wind-off* ratio: ensemble averaging of 128 double frames and calculation of
$$\overline{R}_{\text{wind−off}} = \left(\frac{\overline{I_{G1}}}{\overline{I_{G2}}} \right)_{\text{wind−off}}$$

4. Calculation of *wind-on* ratio: for single-shot result only a single double frame is considered for $R_{\text{wind-on}} = \left(\frac{I_{G1}}{I_{G2}}\right)_{\text{wind-on}}$; for ensemble averaged results the mean of all 128 *wind-on* ratios is calculated $\left(\overline{R}_{\text{wind-on}}\right)$

5. 3D - image projection of *wind-off* and *wind-on* ratio images to blade surface grid with a resolution of $0.9 - 1.1$ nodes/px; the projected image is 5×5 median filtered before mapping is applied

6. Calculation of ratio of ratios according to Eq. 1.1

7. Application of calibration polynomial (Eq. 1.1) under consideration of temperatures at each node (see Sec. 2.2.5)

8. Application of offset correction according to Sec. 2.2.6

A single-shot pressure result obtained at a rotation rate of $f_{\text{rotor}} = 35.4$ Hz and a collective pitch of $\beta_{\text{root}} = 17°$ is depicted in Fig. 2.15. For the results presented, a homogeneous temperature distribution based on the probe reading underneath the blade surface at $r/R = 0.65$ is prescribed at step 7 of the above mentioned data reduction procedure. Principal features of an expected pressure distribution can be assessed. A low pressure region corresponding to stronger suction evolves along the leading edge followed by a pressure increase towards the trailing edge. Close to the blade tip, at $r/R \sim 0.99$, a small region of relatively low pressures is visible denoting the footprint of the tip vortex.
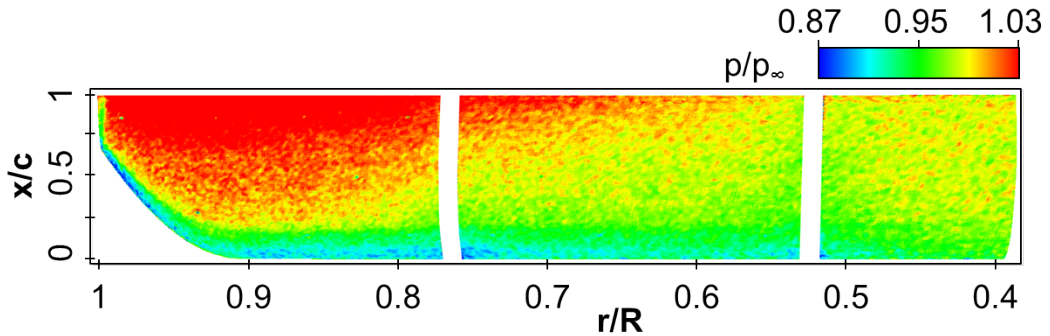
Figure 2.15: Pressure result of temperature uncorrected single-shot ratio of ratios at $f_{\text{rotor}} = 35.4$ Hz; $\beta_{\text{root}} = 17°$. Rotation is counter-clockwise.

2.2.5 Temperature correction

The surface temperature on a rotating blade was previously approximated by the adiabatic wall recovery temperature [21, 162]. Similar to equation 1.20 it can be expressed as:

$$T_{\text{aw}} = T_{\infty} + \frac{\gamma - 1}{\gamma} r(Pr) \cdot \frac{\left(v_{\infty}^2 + (2\pi f_{\text{rotor}} r)^2\right)}{\gamma R_{\text{air}}} \tag{2.3}$$

Due to the linear dependency of the resulting velocity with the blade radius, the theoretical wall temperature increases quadratically from rotor hub to tip. Applying the values in Eq. 2.3 as proposed by Disotell et al. [21] the estimated maximal radial temperature variation within the coated blade area is $\Delta T = 13.4\,°C$ at $f_{rotor,max} = 47.2\,Hz$. The resulting error in pressure would be $\Delta p \sim 9.7\,kPa$ if the pressure and temperature sensitivities of $55.3\,\%/100kPa$ and $0.40\,\%/K$ (see Tab. 2.2) are considered.

To account for this effect, a temperature map is approximated by calculating a value for T_{aw} for each node on the 3D grid according to its radial position and resulting rotational speed (Eq. 2.3). T_∞ is obtained by assuming that the temperature probe on the PSP-blade suction side provides the value of T_{aw} at $r/R = 0.65$ and $x/c = 0.5$. This way, the approximated temperature map is anchored at the position of the associated temperature measurement on the PSP blade. Because the temperature sensor is applied just underneath the original blade surface, the reading might differ from the actual temperature of the PSP coating at that position, due to the foil between the coating and the blade surface. Nevertheless, an offset in T_∞ can be accounted for (see Sec. 2.2.6) and does not affect the radial distribution according to Eq. 2.3.

The validity of this approach is checked by measuring the temperature distribution on the second, structurally identical blade using a TSP coating (Fig. 2.14). For this purpose, PtTFPP was embedded inside the oxygen impermeable poly urethane (PU) binder material (*Clearcoat, ANAC advanced coatings*) as it was previously done by Klein et al. [70]. Application of the same dye as for the PSP allows to use the identical optical setup and additionally enables efficient excitation at 532 nm. Before coating the TSP, the same white foil as used on the structurally identical PSP blade is applied to ensure as similar boundary conditions as possible. The gate exposures are identical to those applied for the PSP blade ($G1|G2 = 5|7\,\mu s$). A delay of $\Delta t_{G1\rightarrow laser} = -10.9\,\mu s$ results in a temperature sensitivity of $0.2\,\%/K$. The residual pressure sensitivity of $3.5\,\%/100kPa$ was neglected and hence the calibration coefficients in the pressure terms of Eq. 1.1 are not considered for the evaluation of temperature. In addition to that, the node-wise temperatures are deduced as described above in Sec. 2.2.4 (steps 1-6). An additional 7×7 median filter was applied at the end to smooth out residual spatial non-uniformities in the data.

The approximated temperature map and the temperatures measured by TSP are displayed in Fig. 2.16a and Fig. 2.16b, respectively. The results correspond to the conditions presented in Fig. 2.15. In general, the temperatures measured by TSP resemble a radial temperature increase, as expected. Moreover, the measured temperature distribution is two-dimensional for the most part of the surface, i.e. between $0.4 < r/R < 0.85$ and $0.1 < x/c < 0.85$. In this region, measured and theoretical approximated data is in good agreement.

Detailed analysis of the TSP results reveal temperatures higher than the theoretical stagnation point temperature along the leading edge ($x/c < 5\,\%$) and values lower than the free stream temperature along the trailing edge ($x/c > 85\,\%$). These unphysical findings can neither be explained by faulty alignment or 3D-mapping nor by blurred images, since both the applied post-processing and the image exposure times are identical for the PSP results (Fig. 2.15). Note also that any faulty trends due to image blur would be in the opposite direction [51]. In fact, it is believed that the observed deficiencies result from unforeseen properties of the dye which was thinned out along the rounded
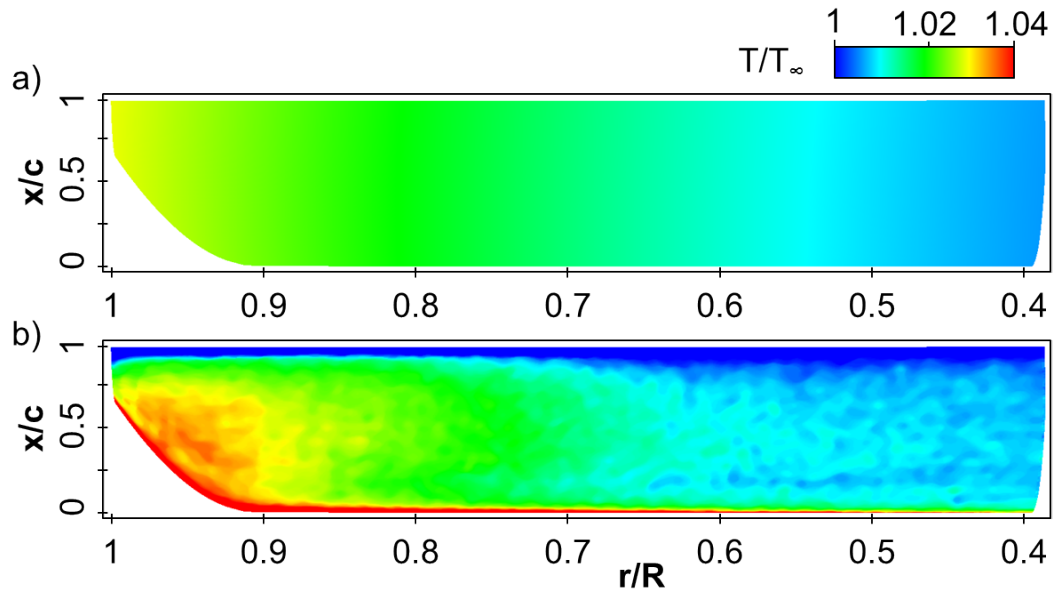
Figure 2.16: *a)* Approximated adiabatic wall temperature. *b)* Temperatures measured by TSP. Same conditions as in Fig. 2.15.

leading edge and accumulated along the tabbed trailing edge (Fig. 2.12) during the drying process. As opposed to the PSP being sprayed onto an intermediate boron-nitride layer, the TSP was directly applied on the foil probably causing different adhesive properties. At $r/R > 0.85$ the measured temperatures exceed the approximation up to a maximum delta of ~2.5 K for $x/c < 0.75$ and a 3D structure becomes visible the reason of which could not finally be assessed.

For these reasons the adiabatic wall recovery temperature is further considered for correction purposes. The temperature-corrected single-shot result from Fig. 2.15 is presented in Fig. 2.17. As opposed to the uncorrected pressure map, the radial pressure gradient is reduced, as expected.
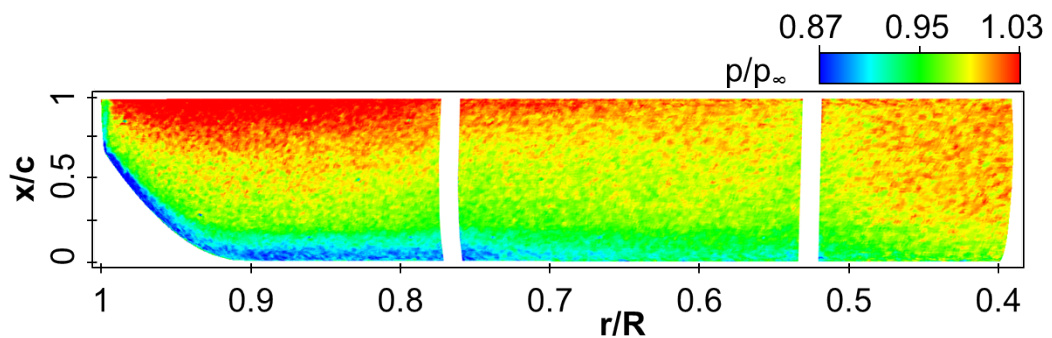
Figure 2.17: Single-shot pressure result of Fig. 2.15 after temperature correction with adiabatic wall temperature from Fig. 2.16a

2.2.6   Offset correction

In PSP measurements any uncertainty in the bulk temperature level of the model surface between *wind-off* and *wind-on* condition causes a bias in the final result. Therefore, if pressure tap data is available, it is common practice to correct for this offset by anchoring the PSP data using the available tap readings nearby [98]. Unfortunately, it is observed in this study that the Kulites installed in the PSP-coated blade pose an internal heat source to the dye which causes a bias in the vicinity of the transducer sections due to the temperature sensitivity of the PSP. This bias can neither be corrected by the approximated wall recovery temperature nor by the temperature measured on the second blade, since this is not instrumented with pressure sensors.

During the measurement campaign the data point presented above was repeated with Kulites switched off. The difference of the ensemble averaged results between the "Kulite-on" and "Kulite-off" condition ($p_{Ku-on} - p_{Ku-off}$) is displayed in Fig. 2.18. It can be deduced that the pressure is underestimated by more than 1 kPa close to the pressure tap sections when the transducers are powered. As opposed to the *wind-off* condition, part of the excess heat from the Kulites is convected by the free stream under *wind-on* condition. This leads to relatively lower values of $T_{wind-on}/T_{wind-off}$ and therefore relatively lower pressures as compared to the Ku_{off} condition (see Eq. 1.1). The observed pressure delta of up to 1 kPa is therefore attributed to underestimated temperatures in the range of 1.25 – 2 K assuming the corresponding sensitivities at pressures between 100 – 70 kPa.
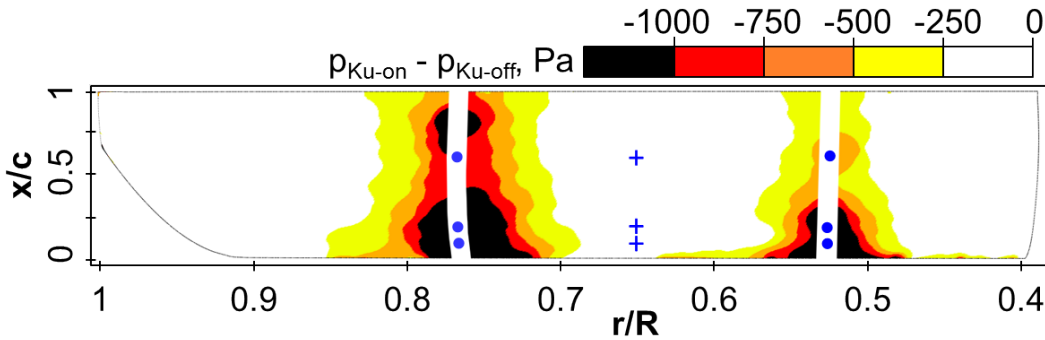
Figure 2.18: Pressure error caused by internal heating of Kulites for conditions presented in Fig. 2.15. Circles and crosses indicate positions of Kulite and PSP data used for offset correction.

An accurate estimation of the resulting temperature on the surface influenced by the Kulite heating is complex. Therefore, the following method is applied in order to correct for an offset in the PSP data and to compare available pressure tap measurements to PSP data not influenced by the effect shown. In Fig. 2.18 circles indicate the Kulite locations where data is available at same chordwise positions for both radial sections, respectively. The PSP data in between, marked as crosses at $r/R = 0.65$ in Fig. 2.18, is now compared to the mean of the adjacent pressure tap measurements at the same chordwise locations according to Eq. 2.4.

$$\Delta_{\text{offset}} \quad = \quad \frac{1}{3} \sum \left[p_{\text{PSP},0.65R,\frac{x}{c}} - \left(\frac{p_{\text{Ku},0.77R} + p_{\text{Ku},0.53R}}{2} \right)_{\frac{x}{c}} \right]; \quad \frac{x}{c} \quad = \quad 0.11; 0.19; 0.62 \quad (2.4)$$

The deduced value describes the average delta between the mean of the corresponding Kulite readings at the same chordwise positions of both radial sections and the corresponding PSP value in between. During post processing Δ_{offset} is added as a bulk shift to all values on the 3D grid. In this campaign the magnitude of the applied offset was in the order of $300\,\text{Pa}$. Note that the correction method implies a linear development of pressure between $0.53 < r/R < 0.77$, which cannot be physically justified. Therefore, this approach is regarded as best practice in this study.

As the final post-processing step, the pressure differences presented in Fig. 2.18 are subtracted from the offset corrected results in order to account for the Kulite heating effect. This is only an approximate correction for other data points at different pitch settings and especially at different rotating speeds as the effect is influenced by the convective heat transport from the surface. Therefore, a quantitative discussion of the PSP data in the vicinity of the Kulite sections is omitted in the discussion of the results. To overcome these deficiencies in future experiments, it should be attempted to either measure the temperature of the PSP coating directly or to repeat all data points with Kulites switched off.

2.3   Results and discussion

In Sec. 2.3.1 the surface pressure distribution is investigated at constant collective pitch for a variation of rotating speeds. The axial inflow velocity v_∞ was adjusted proportionally to the rotating frequency in order to maintain a constant advance ratio $J = v_\infty/(2\pi f_{\text{rotor}} R)$. Furthermore, in Sec. 2.3.2, different blade loadings are examined at constant rotation rate and under variation of the collective pitch angle at $f_{\text{rotor}} = 23.6\,\text{Hz}$. The results indicate the occurrence of stalled flow, which is further investigated in Sec. 2.3.3. A summary of the investigated test conditions is presented in Tab. 3.1. The indicated blade tip Mach and chord Reynolds numbers $\left(M_{\text{tip}}, Re_{\text{tip}} \right)$ are based on the velocity resulting from superposition of the axial inflow to the respective rotating speed, i.e. $\sqrt{v_\infty^2 + (2\pi f_{\text{rotor}} r)^2}$.

Table 2.3: Test conditions

f_{rotor}	$23.6\,\text{Hz}$	$35.4\,\text{Hz}$	$47.2\,\text{Hz}$
M_{tip}	0.29	0.43	0.57
Re_{tip}	$4.63 \cdot 10^5$	$6.94 \cdot 10^5$	$9.26 \cdot 10^5$
β_{root}	$10 - 28°$	$17°$	$17°$
$J = v_\infty/(2\pi f_{\text{rotor}} R) = 0.021 \pm 0.001$			

2.3.1   Variation of rotating frequency

In Fig. 2.19 the surface pressure distribution is presented for rotating frequencies of f_{rotor} = 23.6, 35.4 and 47.2 Hz at a collective root pitch angle of β_{root} = 17°. The results displayed are normalized by the ambient pressure and the same color map is used for all cases to ease a comparative discussion. Note the improved SNR due to ensemble averaging as compared to the single-shot result presented in Fig. 2.17. In all pressure maps shown, suction areas can be distinguished parallel to the leading edge and along the parabolic shaped blade tip followed by the expected pressure recovery in chordwise direction. A comparison of the results reveals that the streamwise pressure gradients are more pronounced as the rotating frequency is increased. This results in comparatively lower pressures close to the leading edge. The larger suction effect at greater rotating frequencies is also manifested in the evolution of the footprint of the tip vortex. It appears as a low pressure region with pronounced radial gradients near the blade tip. The resulting surface pressure in this region decreases with increasing rotation rates. In view of the Kutta-Joukowski theorem the trend is plausible as the tip vortex is expected to gain strength (in terms of circulation) at higher blade velocities [94] and thus induces higher velocities at the blade tip.
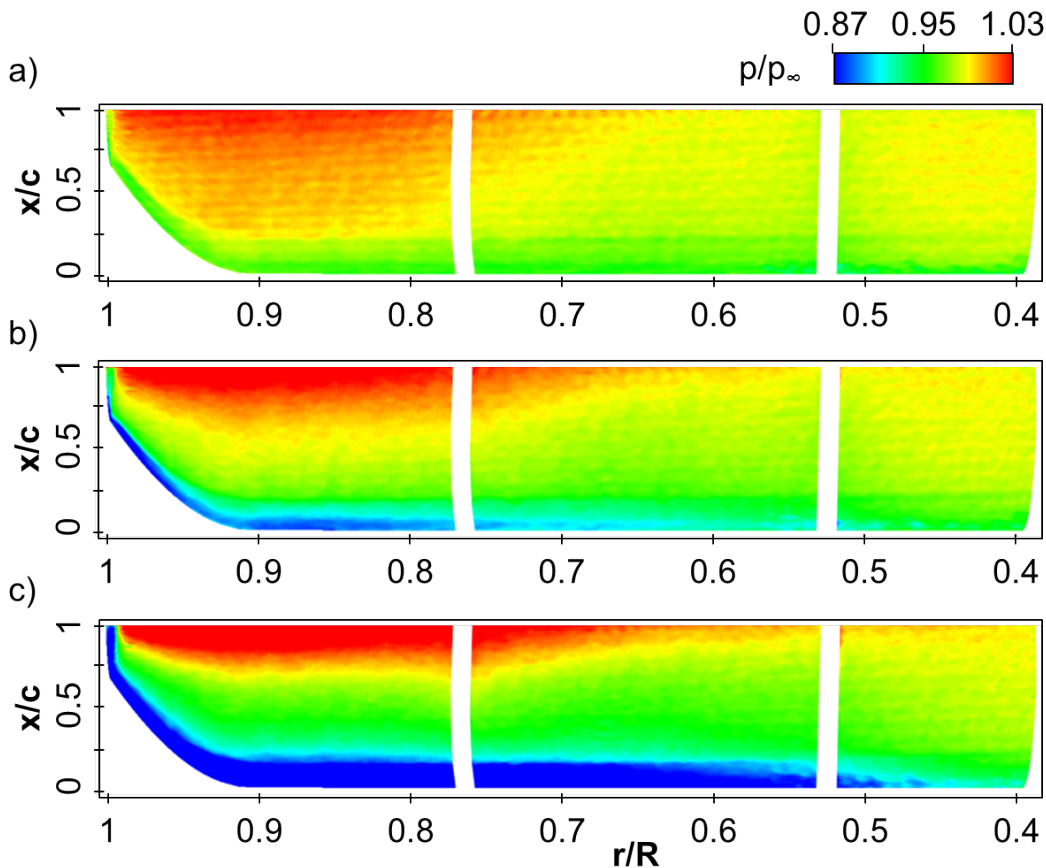
Figure 2.19: Surface pressure distribution at β_{root} = 17° for different rotating frequencies f_{rotor} = *a)* 23.6 Hz *b)* 35.4 Hz *c)* 47.2 Hz
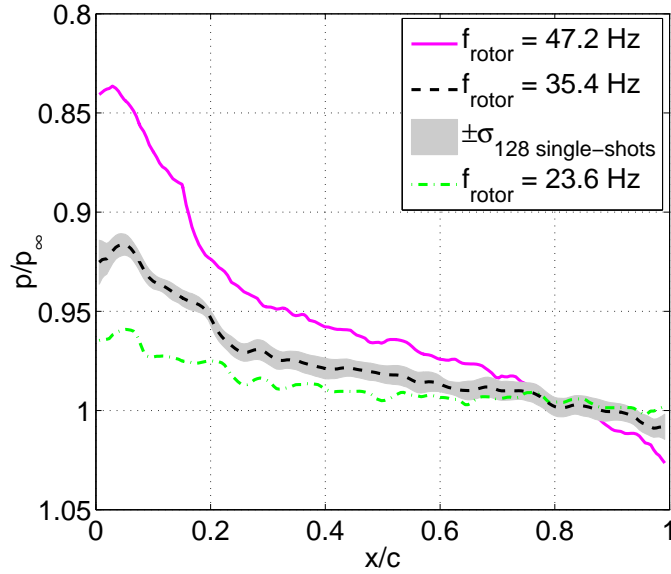
Figure 2.20: Chordwise pressure distribution extracted at $r/R = 0.65$ for different rotating frequencies at $\beta_{\mathrm{root}} = 17°$ (same cases as in Fig. 2.19). The shaded region denotes the standard deviation of 128 consecutive single-shot results.

Note the visible horizontal stripe artefacts in Fig. 2.19. This phenomenon results from a sensor specific fixed periodicity in the electrodes and exists both in horizontal and vertical direction. Since the periodicity is known (in the present case: 16 pixel vertically causing the horizontal stripes and 4 pixel perpendicular to that) appropriate spatial filters can be used to suppress the visibility of this effect (see e.g. [21]). In the present case the applied 5x5 median filter was sufficient to filter out the 4 pixel periodicity. The remaining horizontal stripes could not be filtered out efficiently by a spectral filter possibly due to the low number of stripes. Furthermore, aerodynamic structures exist with only slightly different orientation. As they could be affected by spectral filtering, the application of such a filter was omitted in this direction. Note from Fig. 2.19 that the described effect is predominant in the case of $f_{\mathrm{rotor}} = 23.6\,\mathrm{Hz}$ and it is mostly obscured in the cases with higher SNR, i.e. at $f_{\mathrm{rotor}} = 35.4$ and $47.2\,\mathrm{Hz}$.

For further analysis, the chordwise pressure distribution is extracted at $r/R = 0.65$ and plotted as p/p_∞ against x/c in Fig. 2.20. Note the reversed vertical axis expressing increased suction at higher rotating frequencies. For all cases presented a suction peak is distinguishable, followed by a pressure increase towards the trailing edge as mentioned above. When plotted as p/p_∞, the pressure levels and gradients primarily scale with the resulting dynamic pressure which is a function of both radius and rotating frequency. However, the pressure distribution also depends on the effective angle of attack at the respective cross-section. Since the advance ratio is reasonably constant for all f_{rotor} shown, the variation in angle of attack for the various rotational speeds at $r/R = 0.65$ is expected to be small and the different pressure levels can mainly be attributed to the variation of dynamic pressure.

The data point corresponding to $f_{\mathrm{rotor}} = 35.4\,\mathrm{Hz}$ and $\beta_{\mathrm{root}} = 17°$ has been repeated four times. In
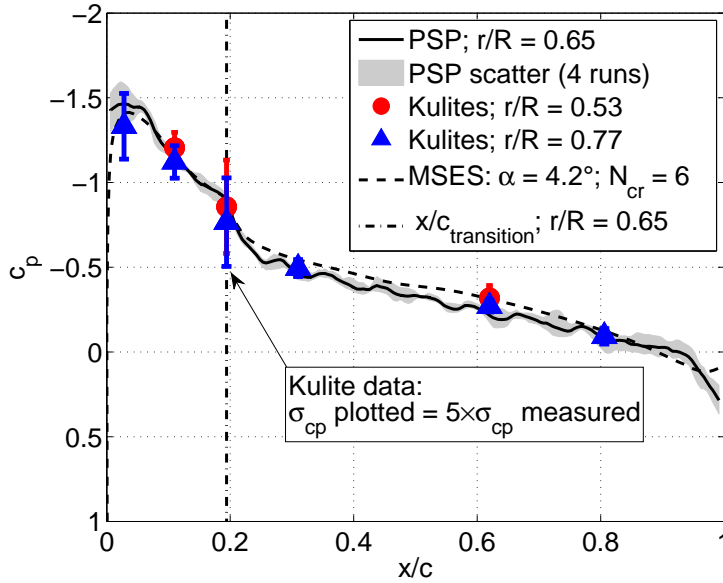
Figure 2.21: Ensemble averaged PSP and Kulite data from four repeated data points at f_{rotor} = 35.4 Hz, β_{root} = 17°. MSES data corresponds to conditions at r/R = 0.65 and f_{rotor} = 35.4 Hz. Vertical line indicates transition position detected from result in Fig. 2.22.

Fig. 2.21, an average of the ensemble averaged PSP data of the four runs is plotted in terms of c_p based on the resultant speed at the respective radial section:

$$c_p = \frac{p_x - p_\infty}{\frac{\rho_\infty}{2} u_{\text{res}}^2} = \frac{p_x - p_\infty}{\frac{\rho_\infty}{2} \left[v_\infty^2 + (2\pi r f_{\text{rotor}})^2 \right]} \tag{2.5}$$

The shaded band includes the ensemble averaged results of all repetitions and comprises Δc_p < 0.15 for the most part of the chord, which corresponds to ±400 Pa in this case. Comparatively greater variations can be deduced close to the leading edge where the pressure distribution is sensitive to variations of the inflow conditions between the individual runs. For comparison, the available Kulite data is added to the graph. The symbols mark the mean of the four averages over a 10 s time interval. Deviations of this mean are smaller than the symbol size. The bars indicate the pressure fluctuation in terms of the respective standard deviations σ_{c_p} averaged over the four runs. Note that the bar sizes are emphasized by multiplying the measured values times five. The Kulite readings at r/R = 0.53 exhibit slightly but consistently lower mean values in c_p than at r/R = 0.77 indicating a slightly lower effective angle of attack further outboard. The trend seems reasonable when considering the negatively twisted blade geometry and the expected increasing induced velocity by the tip vortex at higher radii. Qualitatively, the PSP data resemble the trend prescribed by pressure transducers. For this reason, it is assumed that the pressure distribution is quasi two-dimensional between the pressure-transducer sections. This finding legitimizes the offset correction approach (Eq. 2.4) a posteriori.

An interesting aspect can be observed in the cross-sectional PSP data for f_{rotor} = 35.4 and 47.2 Hz in Fig. 2.20 and for f_{rotor} = 35.4 in Fig. 2.21. In both plots, the chordwise pressure gradients exhibit an abrupt increase at $x/c \sim 0.19$ (at f_{rotor} = 35.4 Hz) and at $x/c \sim 0.15$ (at f_{rotor} = 47.2 Hz),

respectively. In Fig. 2.21 the kink in the pressure distribution coincides with the maximum in σ_{c_p} indicating boundary-layer transition [39]. However, in view of the sparse spatial resolution of pressure transducers the absolute maximum in σ_{c_p} might not be resolved and it is rather coincidental that the pressure discontinuity corresponds to the $\sigma_{c_p,\mathrm{max}}$ location from the available sensors. Nevertheless, the observed discontinuity in the PSP data can be explained by the laminar-turbulent boundary-layer (BL) transition phenomenon as described in more detail by Popov et al. [114].

To show this, BL transition was measured in a separate test by means of TSP. Details of the test including the setup and post-processing procedures are provided in chapter 3. The result for the data point at $f_{\mathrm{rotor}} = 35\,\mathrm{Hz}$ and $\beta_{\mathrm{root}} = 17°$ is presented in Fig. 2.22. The displayed gray scale values of the TSP intensity ratio are a measure of the temperature on the heated model surface. Dark areas correspond to turbulent flow regions and lower surface temperatures due to more efficient cooling as compared to bright areas, which correspond to laminar or laminar separated regions (see [77]). It can be deduced from Fig. 2.22 that the transition region evolves nearly parallel to the leading edge, which supports the above stated hypothesis of a predominantly two-dimensional pressure distribution across the blade. The transition position $(x/c)_{\mathrm{transition}}$ is defined as the chordwise location of the maximum intensity gradient in the thermographic result corresponding to the location of 50 % turbulence intermittency [5, 72]. The transition position detected at $r/R = 0.65$ is indicated by the vertical line in Fig. 2.21. It coincides with the above mentioned pressure discontinuity measured by PSP and the location of the Kulites exhibiting maximum values for σ_{c_p}.
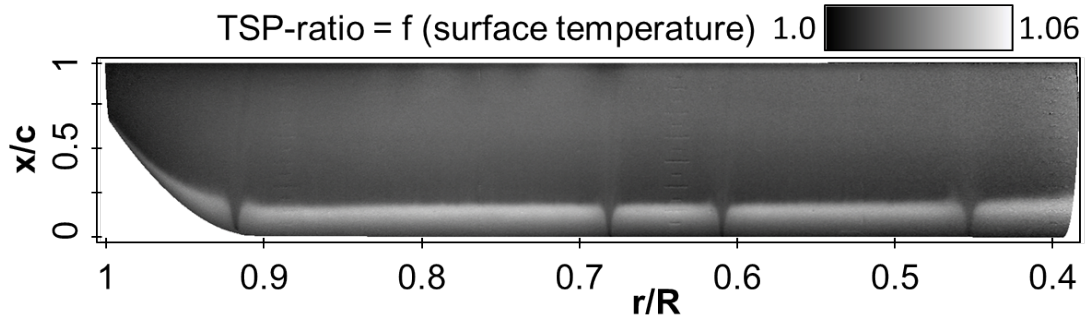
Figure 2.22: Transition result from separate TSP experiment at $f_{\mathrm{rotor}} = 35.4\,\mathrm{Hz}$, $\beta_{\mathrm{root}} = 17°$. Dark areas correspond to turbulent, bright areas to laminar or laminar-separated flow regions. Turbulators are applied at four radial positions causing turbulent wedges further downstream.

It should be mentioned that the observed discontinuity in the PSP data (in Fig. 2.21) partially originates from the different adiabatic wall recovery temperatures between laminar and turbulent boundary-layers. Considering $T_\infty = 283\,\mathrm{K}$, $M_{0.77R} = 0.33$ and the recovery factors of $\sqrt{Pr}$ and $\sqrt{Pr^3}$ for laminar and turbulent boundary-layers (see [30]) at a Prandtl number of $Pr = 0.72$ for air, this temperature difference is $\sim 0.3\,\mathrm{K}$ (according to Eq. 2.3). However, the kink in Fig. 2.21 is in the order of $\Delta c_p \sim 0.2$ corresponding to $\Delta p \sim 1500\,\mathrm{Pa}$. If pressure and temperature sensitivities at reference conditions (see Tab. 2.2) are taken into account, a temperature change of $\sim 2.1\,\mathrm{K}$

would be necessary if the observed pattern was due to different temperatures only. Hence, the influence of chordwise temperature differences between laminar and turbulent flow in the PSP results is believed to be small and the observed discontinuity can mainly be attributed to a change in pressure. In contrast, the temperature differences in the TSP result of the same case (displayed qualitatively in Fig. 2.22) are amplified by heating the blade and reflect the differences in heat transfer between laminar and turbulent boundary-layers. To conclude, PSP can in principle detect BL transition by the pressure gradient (for particular cases) when no other measurement technique is available.

In order to complement the experimental results, computations were performed using the coupled 2D Euler-/ boundary-layer code [24]. The flow was computed for the DSA-9A airfoil at $M_{0.65R} = 0.28$ and $Re_{0.65R} = 4.51 \cdot 10^5$. The conditions are based on the rotating speed at 65 % radius and the PSP data point presented in Fig. 2.21 to allow direct comparison. In the code, transition is predicted via an approximate version of the e^N-envelope method (see Sec. 3.4.1) and the critical $N-$factor used is $N_{cr} = 6$ as suggested by Lang et al. [77]. Computations were performed for various angles of attack α and the best fit between experimental and calculated pressures was found at $\alpha = 4.2°$ (see Fig. 2.21). The MSES simulation predicts a pressure discontinuity at $x/c = 0.19$ due to BL transition matching the experimental findings. Deviations to the PSP results are less than $\Delta c_p \sim 0.1$ for the most part of the chord. Note the last 5 % chord where the pressure increase indicated by PSP is unphysical. The exact reasoning for the latter remains unclear, yet possible causes include incorrect assumptions for temperature or shape deviations between the actual and the theoretical trailing edge contour.

The simulation suggests that the surface pressures are prone to exceed p_∞ near the trailing edge on the suction side of the DSA-9A airfoil causing values of $c_p > 0$. The effect can be attributed to the tabbed contour (Fig. 2.12). It is also visible in Fig. 2.20 and also more pronounced at higher radii (see Fig. 2.19). Gardner and Richter [39] and Richter et al. [122] also measured pressures corresponding to $c_p > 0$ near the trailing edge on the same airfoil. In both studies it was observed that the spatial extent for values of $c_p > 0$ expands towards chordwise locations further upstream at decreasing incident angles. These findings match the qualitative radial trend displayed in the pressure maps in Fig. 2.19. The displayed surface area corresponding to $p/p_\infty > 1$ expands to chordwise positions further upstream when examining the blade at increasing radii where it is believed that the angle of incidence decreases due to the blade twist and tip effects. In addition to that a possible under-compensation of temperature using the approximation from Sec. 2.2.5 would also result in overestimated pressure values as discussed in Sec. 2.3.4. Because the exact radial angle of attack distribution is unknown, a quantitative discussion of the values corresponding to $p/p_\infty > 1$ is not feasible.

2.3.2   Variation of collective pitch

The variation of collective pitch angles from $\beta_{root} = 8.6 - 28.8°$ at $f_{rotor} = 23.6$ Hz reveals interesting PSP results. The pressure map at $\beta_{root} = 24°$ is displayed at the top of Fig. 2.23. It exhibits the same features as discussed above in Fig. 2.19. In contrast, the topology of the PSP result at $\beta_{root} = 28°$ on the bottom of Fig. 2.23 is noticeably different. The tip vortex is less pronounced and
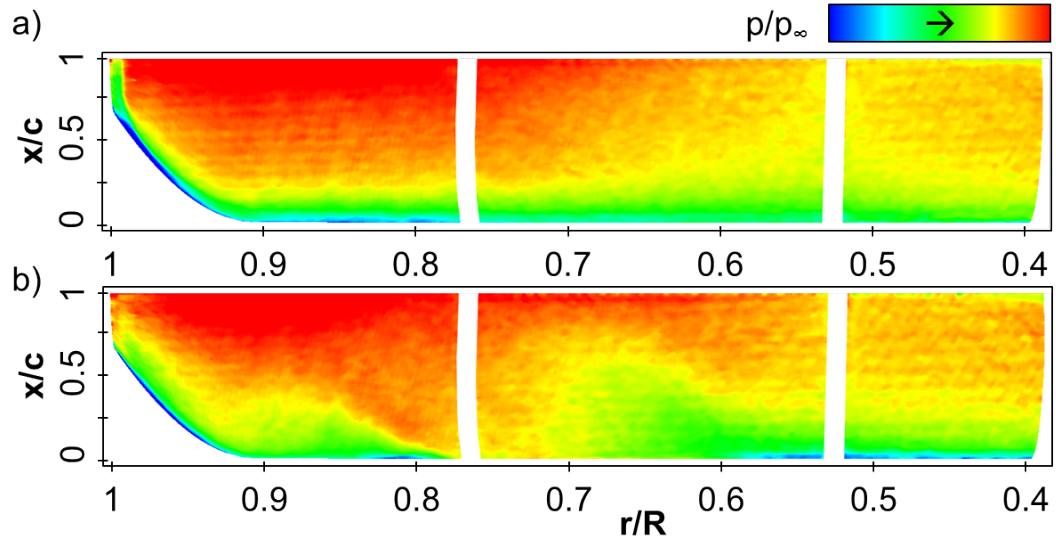
Figure 2.23: Pressure topology (ensemble averaged) for $f_{rotor} = 23.6$ Hz at $\beta_{root} = 24°$ *a)* and 28° *b)*. Data corresponds to points highlighted by blue squares *a)* and red diamonds *b)* in Fig. 2.24 and Fig. 2.25.

the pressure pattern is significantly altered between $0.65 < r/R < 0.9$. Especially in the region between $0.7 < r/R < 0.8$ the suction peak diminishes almost completely as compared to the case at $\beta_{root} = 24°$. Moreover, oblique pressure gradients can be distinguished between $0.6 < r/R < 0.7$ and $0.8 < r/R < 0.85$ on the blade. The observed three dimensional features at $\beta_{root} = 28°$ in the ensemble averaged results are caused by stalled flow. Therefore, the offset correction according to Eq. 2.4 was omitted because the assumed linear pressure development between the Kulite sections is infringed. Moreover, both corrective measures applied, the temperature correction via Eq. 2.3 and the subtracted influence of the internal Kulite heating do not resemble the appropriate physical behavior under stalled flow conditions due to differently balanced convective heat transfer as compared to the attached flow scenario. Hence, a quantitative discussion is omitted yet the results are suited for qualitative comparison as data acquisition and processing is identical for the cases presented.

Stalled flow conditions at $\beta_{root} = 28°$ are confirmed by the integral thrust measured by the piezo-balance. The polar in Fig. 2.24 exhibits the expected increase in thrust up to a collective pitch angle of $\beta_{root} = 26°$, where it reaches the maximum blade loading coefficient (according to Eq. 3.1, see [79]) of $C_T/\sigma = 0.165$. At $\beta_{root} \geq 28°$ the thrust exceeds its maximum and the standard deviation is almost doubled as indicated by the bar sizes denoting at least partially stalled flow. A similar maximum in thrust and the corresponding overall high standard deviations were previously measured by Schwermer et al. [142] investigating the same configuration. They attributed the high level of fluctuations to the recording of inertial forces due to mechanical system vibrations of the test stand.

The findings are complemented by time averaged Kulite recordings at the conditions corresponding to the colored symbols in Fig. 2.24. For $\beta_{root} = 20, 24$ and 28° the mean pressures are plotted
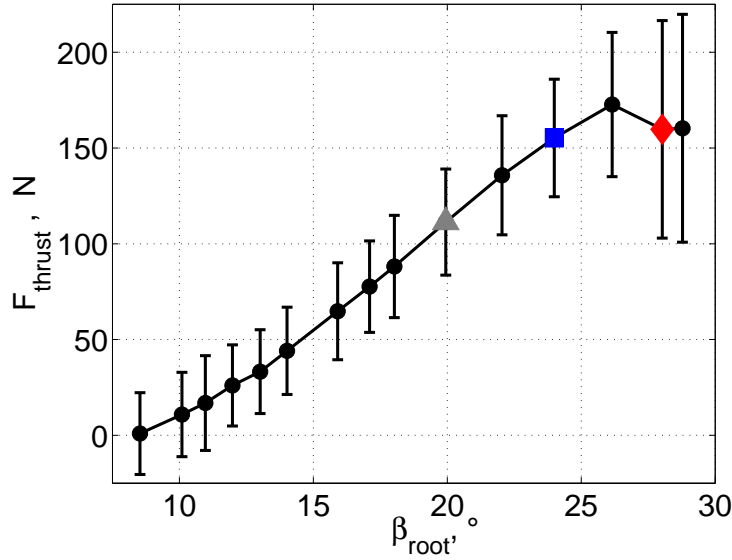
Figure 2.24: Thrust polar at $f_{rotor} = 23.6\ Hz$ for various β_{root}, bars indicate standard deviation of a time series of $10\ s$ sampled at $200\ kHz$.

as chordwise c_p−distributions in Fig. 2.25 with bars indicating the standard deviation σ_{c_p}. For $\beta_{root} = 20°$ and $24°$, the pitch angle increase results in stronger suction especially close to the leading edge at both radial sections. The data at $\beta_{root} = 28°$ and $r/R = 0.53$ follows the trend prescribed above indicating increased suction as compared to the lower pitch angles. In contrast, at $r/R = 0.77$ the c_p−distribution is characterized by remarkably higher pressures close to the leading edge accompanied by almost no pressure recovery further downstream. The resulting plateau-type distribution correlates with significantly increased values of σ_{c_p} which is characteristic for stalled flow [40, 88]. Note the significantly greater difference in standard deviation between attached and stalled flow regions for the pressure sensors as compared to the balance data in Fig. 2.24 because the former capture aerodynamic fluctuations only.

Considering the presented pressure maps obtained by PSP in conjunction with the force balance and Kulite measurements, it is concluded that the pressure topology at $\beta_{root} = 28°$ is influenced by partially stalled flow for $r/R > 0.6$.

2.3.3   Pressure fluctuation analysis

The unsteady Kulite signal at $r/R = 0.77$ and $x/c = 0.028$ is investigated for the cases at $\beta_{root} = 24°$ and $28°$. The time series of the pressure fluctuations p' and the corresponding amplitude spectra are plotted in Fig. 2.26a and Fig. 2.26b. The signals shown are conditioned by a $500\ \text{Hz}$ Butterworth low-pass filter. The spectra are obtained from a Fast-Fourier Transformation (FFT) of the Hanning-windowed time series. The overall stronger pressure fluctuations in the time signal at $\beta_{root} = 28°$ reflect the difference in σ_{c_p} as observed in Fig. 2.25. The corresponding spectrum in Fig. 2.26b denotes comparatively high amplitudes especially at frequencies below $2 - 3\ \text{Hz}$. Note that in both signals the highest amplitudes are contained in the rotating frequency and its higher
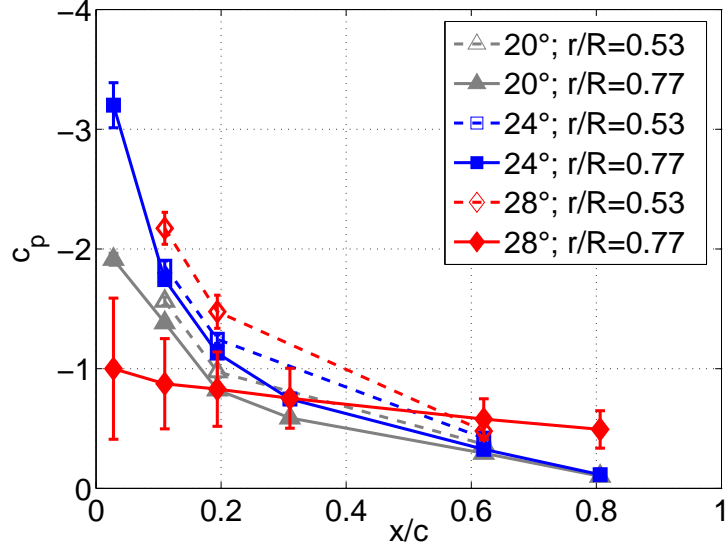
Figure 2.25: Kulite data at $f_{\text{rotor}} = 23.6\,\text{Hz}$ for different β_{root}. Symbol- and color-coding corresponds to data points highlighted in Fig. 2.24.

harmonics. This is due to the rotor support downstream and in the wake of the rotor disc causing an upstream pressure change once per revolution for the blade equipped with pressure sensors. The effect is therefore also present under the attached flow condition at $\beta_{\text{root}} = 24°$, where all other frequencies exhibit negligible amplitudes.

Whereas conventional phase-averaging methods are in principle limited to resolve periodic phenomena, a great advantage of the single-shot lifetime technique is that it allows to capture random, i.e. broadband pressure fluctuations. Presuming that the camera is at rest, transient phenomena are sampled every n^{th} blade revolution depending on the system limit with respect to the data acquisition rate and the time response of the PSP sensor. In order to extract information on pressure fluctuations from the data available the measured standard deviation in pressure is evaluated according to:

$$\frac{\sigma_{p'}}{p_\infty} = \frac{1}{s_{p,\text{ref}}} \cdot \frac{\sqrt{\sigma_{R_{\text{wind-on}}}^2 - \sigma_{R_{\text{wind-off}}}^2}}{\overline{R}_{\text{wind-off}}} \tag{2.6}$$

In this equation σ_R is the standard deviation of all 128 *wind-on* and *wind-off* ratio images, respectively, and $s_{p,\text{ref}}$ is the pressure sensitivity at reference conditions ($100\,\text{kPa}$, $20°$). In the expression above, it is assumed that $\sigma_{R_{\text{wind-on}}}$ contains residual noise from image acquisition and processing which is superposed to the signal variations due to oscillating pressure. Therefore, $\sigma_{R_{\text{wind-off}}}$ is subtracted since the *wind-off* ratio images are acquired at constant pressure and thus contains residual noise only.

The resulting standard deviations at $f_{\text{rotor}} = 23.6\,\text{Hz}$ and $\beta_{\text{root}} = 24°$ as well as at $28°$ are displayed in Fig. 2.27a and Fig. 2.27b, respectively. As opposed to the case at $\beta_{\text{root}} = 24°$ significantly stronger pressure fluctuations occur at $\beta_{\text{root}} = 28°$. They can be deduced along the leading edge starting from $r/R > 0.6$ all the way to the blade tip, where the footprint of the tip vortex was
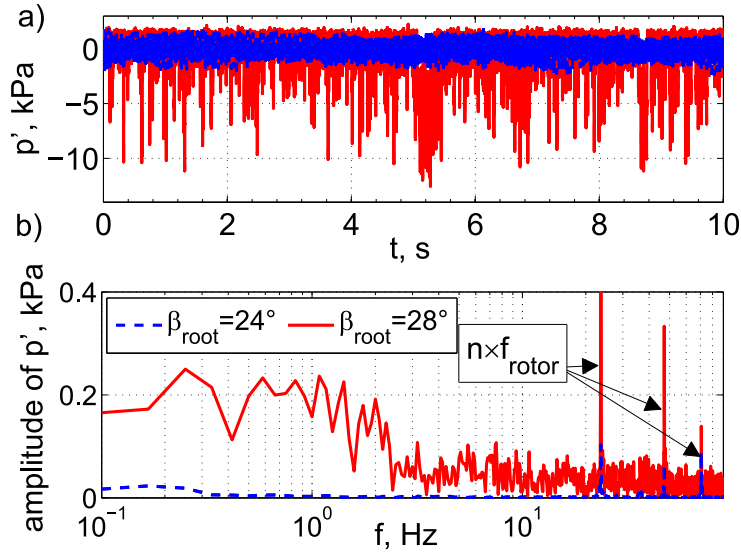
Figure 2.26: Time series *a)* and amplitude spectra *b)* of pressure fluctuations measured by Kulite at $x/c = 0.028$; $r/R = 0.77$ and $f_{\text{rotor}} = 23.6\,\text{Hz}$. Signals are low-pass filtered at $500\,\text{Hz}$. Colors as in Fig. 2.24 and Fig. 2.25.

previously identified (see Fig. 2.23). The finding seems reasonable presuming that it constitutes the area where the flow detaches causing blade loading fluctuations and thus a transient behavior of the tip vortex as well. Letzgus et al. [81] simulated the same rotor model configuration at cyclic pitch variation. In their study, stall onset was detected by finding incipient vortex shedding starting from the leading edge at $80 - 90\,\%$ radius which is where transient flow is detected in this study. In Fig. 2.27b strong pressure fluctuations can be distinguished in the form of an oblique patch between $0.8 < r/R < 0.9$. It is accompanied by a smaller area between $0.6 < r/R < 0.65$ which also denotes increased oscillations. Note that these patterns occur approximately where oblique pressure gradients can be deduced from the corresponding ensemble averaged pressure result in Fig. 2.23b. Similar oblique patterns were detected by Disotell et al. [21] on helicopter blades in forward flight who attributed the finding to the effect of centrifugal forces on detached flow structures as previously studied by Raghav and Komerath [120].

It should be noted that the PSP sensor used in this study (PtTFPP in poly(4-TBS)) is mainly designed for steady-state measurements. Though the time response has not been measured explicitly, it is expected to be in the order of several Hertz, similar to other polymer-based PSPs [163]. Thus, it is believed that mainly the increased low-frequency amplitudes are contained in the result shown in Fig. 2.27. In addition, higher-frequency fluctuations (above $5 - 10\,\text{Hz}$) are smeared out which complicates a precise distinguishability between stalled and attached flow regions in the result shown. For more sophisticated investigations, the measurement system dynamics should be improved especially in terms of the time response of the PSP sensor. For instance, fast-responding PSPs have successfully been applied to capture transient pressure phenomena on model helicopter rotor blades in forward flight [21, 162]. However, the results presented in this study underline the capability of the single-shot lifetime technique to investigate stalled flow on fast rotating blades.
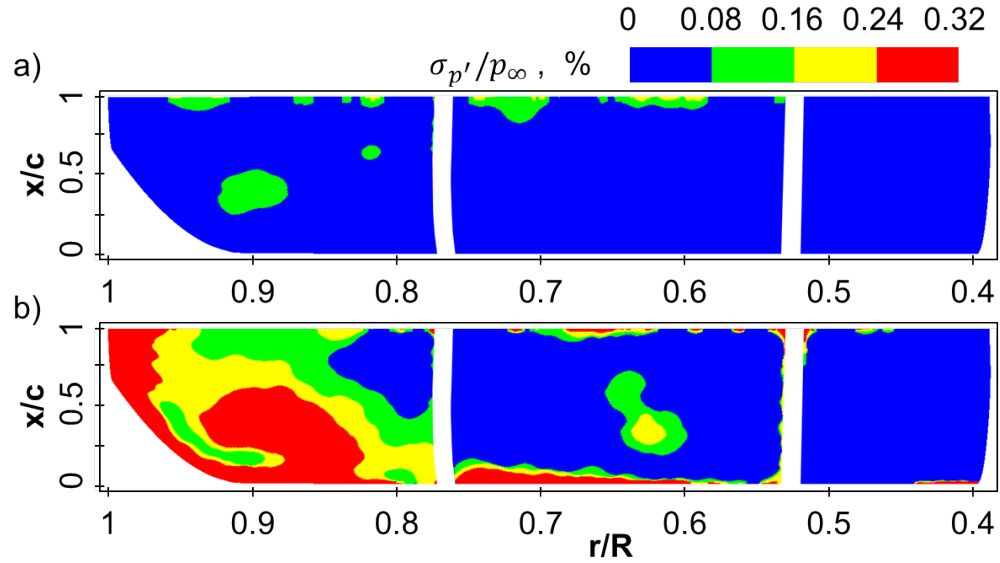
Figure 2.27: Measured relative standard deviation of pressure according to Eq. 2.6 for $f_{rotor} = 23.6$ Hz; $\beta_{root} = 24°$ *a)* and $28°$ *b)*.

2.3.4   Measurement uncertainty

The uncertainty remaining from uncorrected temperature ranges from $0.5 - 0.8$ kPa/K with increased sensitivity at higher pressures and lower temperatures occurring closer to the rotor hub. In this work, the maximum deviation between valid TSP data and the adiabatic wall temperature is found to be ~2.5 K in radial direction. An uncertainty in this range corresponds to an error in pressure between $1 - 2$ % of p_∞ in blade radial direction depending on the temperature between the tip and the hub, respectively. Even if temperature effects are appropriately corrected for, the limiting error source in that case is due to photon noise in the acquired images. According to the method proposed by Liu and Sullivan [85] for the gated-lifetime approach, this uncertainty ranges approximately from 1.4 to 2.3 % for the single-shot results. The variation is due to the variability of pressure sensitivity with temperature and pressure as well as due to the inhomogeneous signal intensity across the blade span. Ensemble averaging of 128 images reduces this uncertainty to 0.1 – 0.2 % corresponding to $100 - 200$ Pa, according to the test conditions in this work.

All error sources in PSP measurements are included, when comparing the data to reference measurements such as the fast response pressure transducer readings in this study. In view of the above mentioned difficulties in the vicinity of the Kulite sections (see Sec. 2.2.6), PSP data is extracted at $r/R = 0.65$ and compared to the mean of pressure tap data at the same chordwise locations but at 53 % and 77 % radius, respectively. After applying the offset according to Eq. 2.4, the residual deltas are evaluated at each chordwise location and for all data points but the one, where stalled flow is detected. The root-mean-square level of the residual deltas is ~250 Pa. Because the value is based on the assumption of linear pressure evolution in between the Kulite sections and includes all possible error sources (see [85]), it is reasonable that the more restrictive and theoretical photon-noise approximation from above is exceeded.

3 Boundary-layer transition investigations[2]

The following chapter comprises boundary-layer transition investigations on the suction side of a Mach-scaled helicopter blade in climb. For this purpose the same rotor configuration was utilized as for the PSP measurements presented in Sec. 2.2-2.3. Transition experiments were conducted in the same facility as for the PSP campaign (see Sec. 2.2.1) and integral thrust as well as surface pressure measurements at two radial blade sections complement the study. The content of this chapter is organized as follows: After a description of the investigated parameter range and of the conducted transition experiments, the procedure of how boundary-layer transition is detected and how the extent of laminar flow is quantified are presented. Experimental results are extensively discussed with respect to variations in collective pitch and rotating speed. An experimental approach is presented with respect to the investigation of the effect of rotational forces on measured boundary-layer transition. The experimental findings are finally compared to two-dimensional (2D) numerical computations and transition N-factors are obtained by employing methods based on 2D linear stability theory.

3.1 Investigated parameter range and thrust measurements

The investigated parameter range comprises three different rotating speeds at various collective pitch settings β_{root}, respectively. The test conditions are listed in Tab. 3.1.

Table 3.1: Test conditions for boundary-layer transition experiments

	Re_{tip}, 10^5	M_{tip}	f_{rotor}, Hz	β_{root}, °	v_∞, m/s	p_∞, hPa	T_∞, °C	$Re_{0.77R}$, 10^5	$M_{0.77R}$
I	4.86 ± 0.04	0.29	23.6	8.7 - 13.5	2.0	1000 ± 2	7.7 - 8.9	3.74	0.22
II	7.34 ± 0.08	0.43	35.4	8.5 - 13.5	3.1	1000 ± 2	7.6 - 9.5	5.65	0.33
III	9.38 ± 0.02	0.57	47.2	8.7 - 16.9	4.1	987 ± 2	12.2 - 13.0	7.21	0.44

Fine increments in β_{root} were selected in order to resolve small changes of the transition region with changing angles of incidence. For each rotating speed, the axial inflow u_∞ was adjusted to maintain an approximately constant advance ratio $J = v_\infty/(2\pi f_{\text{rotor}} R)$. The investigated parameter range is plotted in Fig. 3.1 as J against β_{root}. The measured thrust force is evaluated in terms of the blade loading coefficient

$$\frac{C_T}{\sigma} = \frac{F_{\text{thrust}}}{\rho_\infty A_{\text{blades}} (2\pi f_{\text{rotor}} R)^2} \tag{3.1}$$

where $A_{\text{blades}} = 2cR$, and plotted against collective pitch in Fig. 3.2.

---

[2]Text and illustrations from this section appear in:

A. Weiss, A. D. Gardner, C. Klein, and M. Raffel. Boundary-layer transition measurements on Mach-scaled helicopter rotor blades in climb. *CEAS Aeronautical Journal*, 8(4):613–623, 2017. doi: 10.1007/s13272-017-0263-2, and in

A. Weiss, A. D. Gardner, T. Schwermer, C. Klein, and M. Raffel. On the effect of rotational forces on rotor blade boundary-layer transition. In *2018 AIAA Aerospace Sciences Meeting*, number AIAA 2018-0309, Kissimmee, FL, USA, January 8-12 2018. doi: 10.2514/6.2018-0309.
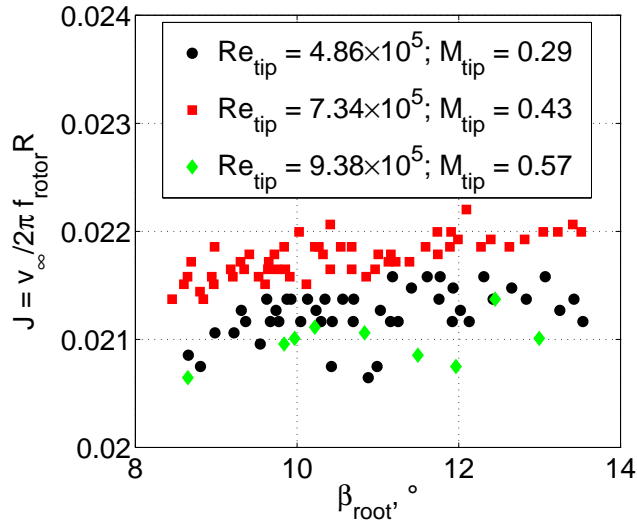
Figure 3.1: Parameter range for boundary-layer transition investigations in terms of advance ratio J against collective pitch at blade root β_{root}.
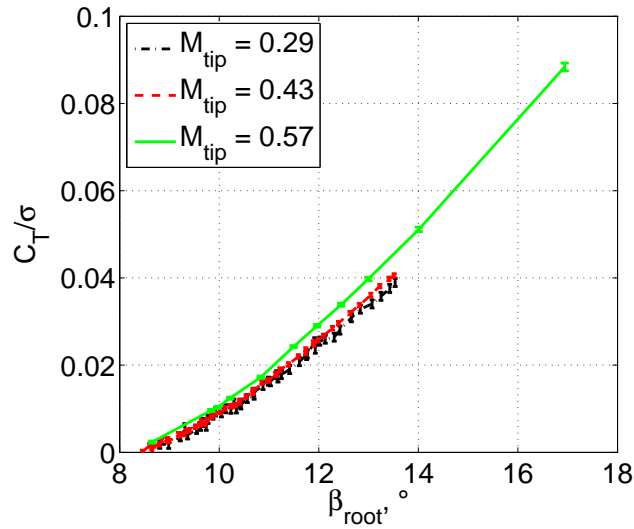
Figure 3.2: Blade loading coefficient against collective pitch setting for all data points.

The bar sizes indicate the linearity error of the piezo-balance being ± 1 % of the measured value but at least ± 1 N. As expected, the blade loading increases at higher collective pitch settings. The absolute thrust forces measured at the lowest Re_{tip} are similar to those obtained by Schwermer et al. [142], who investigated the same test configuration at conditions comparable to condition I. When plotted as C_T/σ the curves coincide especially at low collective pitch settings and start to diverge for $\beta_{\text{root}} > 11°$. The latter is due to compressibility effects at the two higher rotating speeds.

3.2   Experimental setup, data acquisition and processing

Most investigations are based on data obtained with TSP. For comparison selected data points were acquired in a separate campaign by means of IR thermography.

3.2.1   TSP measurements

Setup   A sketch of the setup for the transition measurements via TSP is provided in Fig. 3.3.
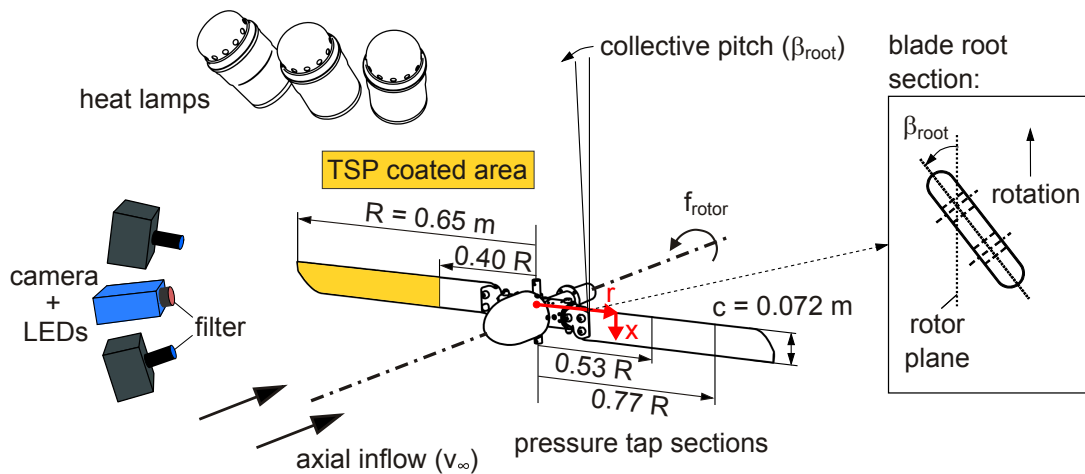
Figure 3.3: Sketch of experimental setup for TSP measurements in the rotor test facility of DLR Göttingen with important dimensions (geometry is modified from [119]).

The TSP sensor applied in this test is based on ruthenium phenanthroline (Ru(phen)) inside a polyurethane binder matrix. The TSP and method have been employed previously and are described in more detail by Yorita et al. [170]. Before the blade was coated, a thin matt white foil (*3M Scotchprint 1080*, ~90 µm) was applied in order to enhance the luminescent signal and to protect the model surface finish from aggressive solvents. The TSP was applied between $0.4 < r/R < 1$ on the suction side of the blade which is not equipped with pressure transducers (see Fig. 3.3). After coating, the TSP surface was polished to a mean roughness depth of $R_z = 0.2 - 0.8$ µm. TSP excitation was provided by four pulsed LEDs (*Hardsoft Illuminator*) emitting in the blue at a peak wavelength of 462 nm. The emitted TSP signal peaks at 580 nm and was recorded by a 14 bit CCD camera (*pco.4000*) with a resolution of 4008×2672 pixels. The temperature-sensitive luminescence was separated from the excitation light using a 550 nm low pass filter on the LEDs and a 600 ± 40 nm band pass filter on the camera lens (*Nikon Nikkor*, 50 mm, f/1.4). The spectral characteristics of the TSP sensor are provided in Fig. 3.4 along with the emission and transmission characteristics of the blue LED and the applied band pass filter. Camera and lens were mounted under the Scheimpflug condition [12] due to the oblique perspective of the installed hardware with respect to the rotor blade (see Fig. 3.3). The final resolution of the model surface was 6.5 and 8.8 pixel/mm in span- and chordwise direction, respectively. In other words, TSP information is provided on 635 pixels along the chord and 2535 pixels across the TSP-coated span.
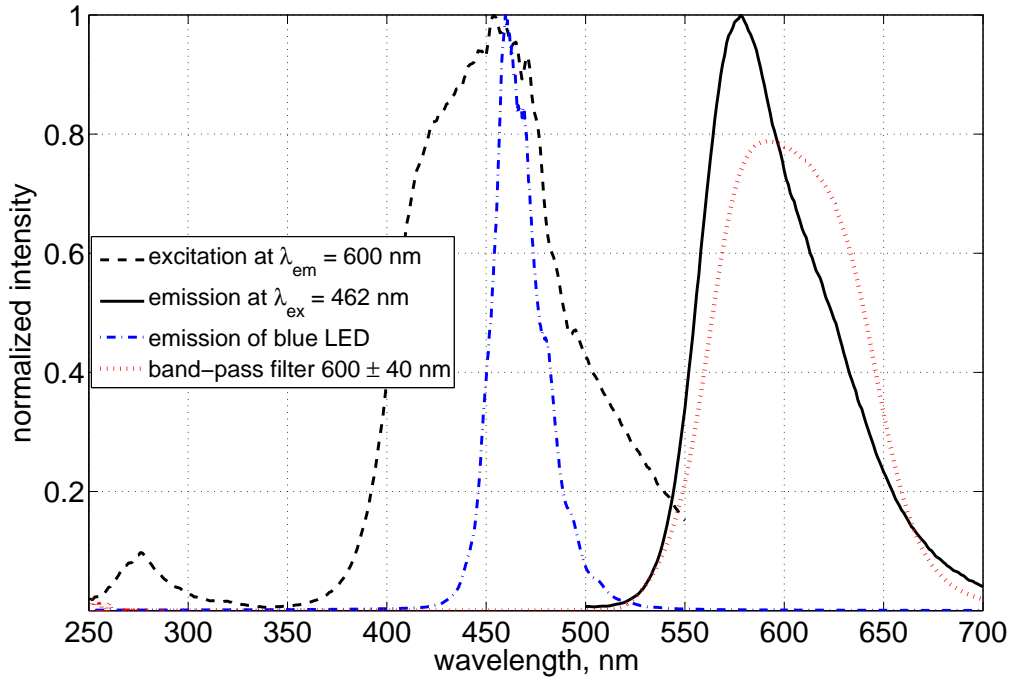
Figure 3.4: Spectral characteristics of Ru(phen), emission spectrum of the blue LED used for TSP excitation and transmission characteristic of the employed band pass filter.

Data acquisition and processing   For image acquisition the camera was operated in modulation mode in order to capture sharp images at high SNR. It means that, depending on the rotating speed of the rotor, 7 or 12 exposures are accumulated to a single image at equal phase positions and with an integration time of 11 or 8 μs for each exposure. In the worst case ($f_{rotor} = 47.2$ Hz) the movement of the blade tip was ~ 1.5 mm during an image exposure. The LED pulse width was set equal to the camera exposure time and a multi-trigger digital delay generator (*BNC - Model 725*) was used to align the excitation pulse and image exposure with respect to a master trigger. The latter was provided by a custom made selective-trigger-box used to position the rotating blade within the camera field of view as sketched in Fig. 2.13. The box allows the selection of the appropriate rising edge of the 1000/rev rotor shaft encoder signal realizing a phase shift at 0.36° increments.

The TSP data recording procedure in this study is adopted from Lang et al. [77] and illustrated in Fig. 3.5. As described in Sec. 1.2.2 a simple division of the luminescence intensities at quasi-stationary reference conditions (I_{ref}) by the intensities acquired at a temperature difference between airflow and model (I) suffices to enhance the distinguishability between laminar and turbulent boundary-layer flow [36]. The acquisition of 16 reference images (I_{ref}) was started after the rotor reached the desired rotating speed and as soon as the online reading of the surface temperature measured by a Pt100-probe on the blade suction side at $r/R = 0.65$ reached asymptotic values denoting temperature equilibrium. The rotor blade surfaces were then consistently heated up for 60 s until temperature equilibrium could again be inferred by an asymptotic Pt100-probe reading. The heating was realized by seven 2 kW halogen spot lights which were arranged around

the wind tunnel nozzle outlet (see sketch in Fig. 3.3). A series of 16 "heated" images (I) was then acquired right after the spot lights were turned off to avoid any disturbances of the recorded TSP luminescence. The resulting ratio I_{ref}/I then qualitatively describes the surface temperature subject to the difference in convective heat transfer between laminar and turbulent boundary-layers.
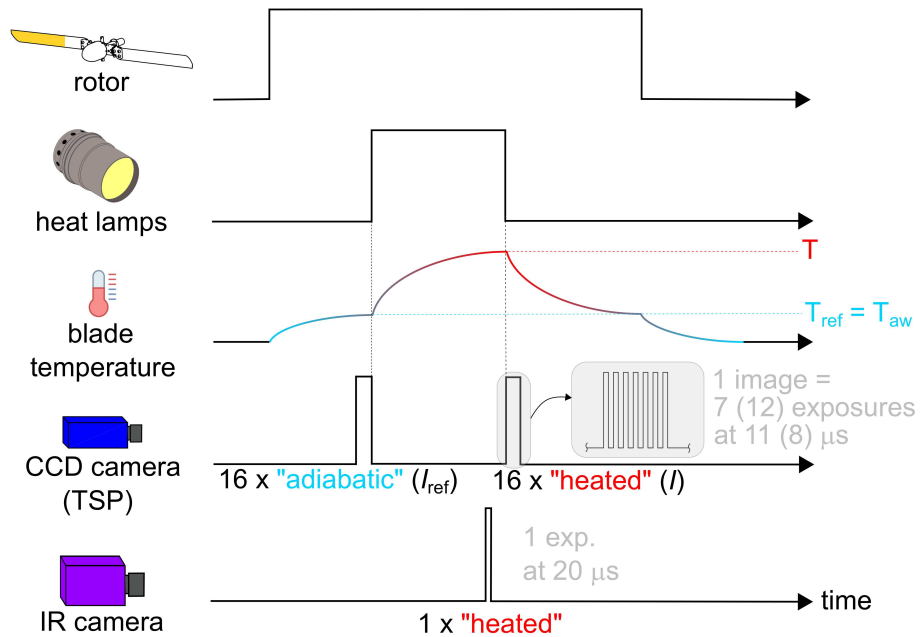
Figure 3.5: Data acquisition scheme for TSP and IR measurements.

An example raw TSP image is displayed in Fig. 3.6 *top*. Marker lines were applied at $\Delta = 5$ mm onto the surface as well as at $r/R = 0.53$ and $r/R = 0.77$ for orientation. In addition to that 23 dot markers are visible. They are used for image alignment in post processing. Note the visible pattern in the emitted luminescence being visible on the blade. It is mostly due to the slightly inhomogeneous excitation light distribution. Since both images needed for division are acquired under quasi-steady conditions while the blade is rotating, the pattern cancels out after the images are processed (see Fig. 3.7).

All image processing was performed with the inhouse software *ToPas* including the following steps:

1. Subtraction of *dark* images from all images to account for background illumination and CCD - *dark* current

2. Applying a flat-field correction and a 3x3 pixel median filter to account for spatial nonuniformities on the CCD chip

3. 2D alignment of all images using 23 dot-markers applied to the surface

4. Averaging of all images acquired prior to and after the "temperature step" and division of averaged images to obtain I_{ref}/I

TSP raw image:
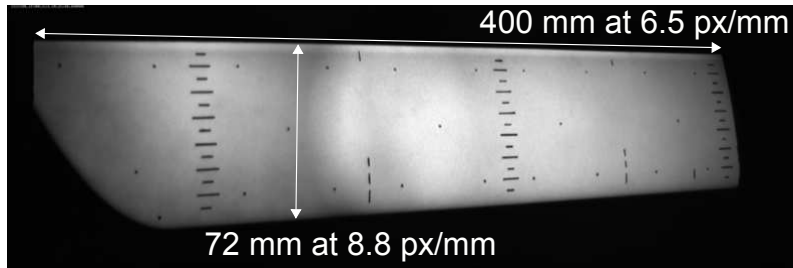
IR raw image:
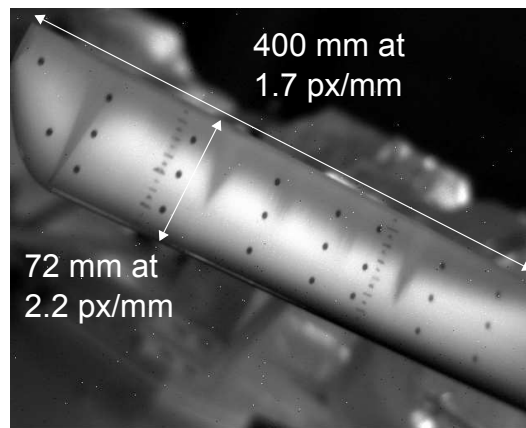
Figure 3.6: Raw images acquired by TSP *(top)* and IR *(bottom)* and spatial resolutions, accordingly.

5. 3D mapping of the final image data to a 3D grid of the model suction side as in [69, 77]

The resolution of the final results on the 3D grid is 4.2 and 5.7 nodes/mm in span- and chordwise direction, respectively.

3.2.2 IR measurements

For selected data points and comparative reasons IR data was obtained of the suction side of the blade which is equipped with pressure transducers and no extra surface coating was applied. Despite the camera and LEDs used for TSP measurements, the setup in principle corresponds to the sketch in Fig. 3.3. The IR camera used was a *FLIR SC7750-L* with a 50 mm lens. It provided images at a spatial resolution of 1.7 and 2.2 pixel/mm in span- and chordwise direction. This is about one fourth of the resolution achieved by the TSP setup. The exposure time was set to 20 μs. At $f_{\text{rotor}} = 23.6\,\text{Hz}$ for instance, the resulting image blur at the blade tip comprises 1.9 mm comparing to 1.1 mm at 11 μs exposure time for the TSP images. As opposed to the TSP data acquisition procedure, IR images were acquired while the heat lamps were switched on (see Fig. 3.5). This could be realized due to the long-range IR sensitivity of the camera sensor between 8.0−9.4 μm, whereas the halogen heat lamps emit ∼ 95 % of the energy at wavelengths of less than 4 μm [58].

A sample raw image obtained by IR is shown in Fig. 3.6 *(bottom)*. The visible dot markers were applied for image alignment and projection onto a 3D grid. Note the greater size of the markers as

compared to the TSP raw data on the left hand side which is due to the lower spatial resolution of the IR camera. As opposed to the "heated" TSP image, a distinction between laminar and turbulent regions is clearly visible in the IR data and expressed by the change from bright to dark as the flow condition changes from laminar to turbulent. For instance, a turbulent wedge can be distinguished close to the blade tip, emanating from a transition dot which has been applied as proof-of-concept. The post-processing of the IR images comprised the application of a 3×3 median filter (to remove hot pixels) and to the mapping of the filtered image to a 3D grid of the model surface. The measures applied are equivalent to steps 2 and 5 of the TSP post-processing mentioned above.

3.3 Experimental results and discussion

3.3.1 Topology and quantification of transition region

A sample TSP result is presented in Fig. 3.7 for a collective root pitch of $\beta_{\text{root}} = 12.4°$ at $Re_{\text{tip}} = 4.86 \times 10^5$. The bright and dark areas correspond to higher and lower temperatures and therefore to regimes of less or more efficient cooling of the heated blade surface, respectively. Note the orientation markings at equidistant chordwise locations and at those radial positions where pressure data is available. Because the applied marks nearly disappear when dividing the images (post-processing step 4 in Sec. 3.2.1), the visible lines in Fig. 3.9 are masked over the displayed result after post-processing to ease visual analysis. At $r/R = 0.92$ a roughness element was attached to the leading edge serving as proof-of-concept to always distinguish turbulent from laminar flow. The resulting turbulent wedge is clearly visible. The rest of the span exhibits a gradual increase
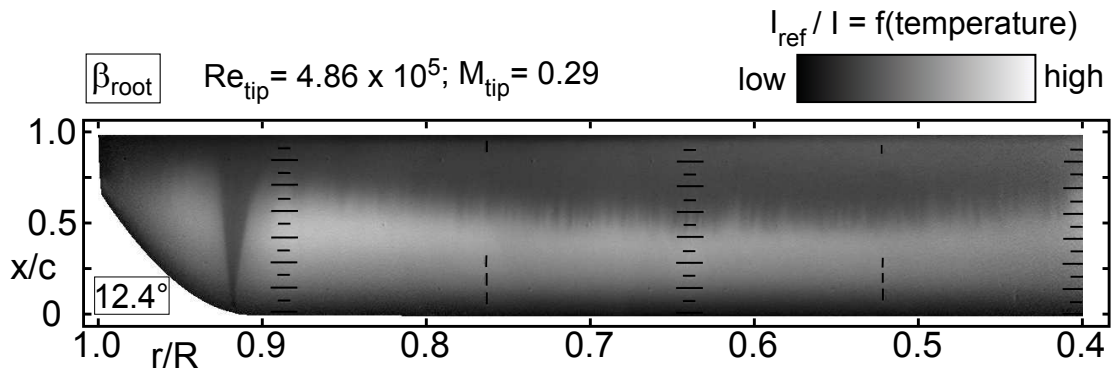
Figure 3.7: Sample boundary-layer transition result obtained from TSP. Rotation is counter-clockwise. Black lines represent orientation markers on the surface at $\Delta = 5\,\text{mm}$ in chord direction and at the locations of available pressure data (acquired on the second blade).

in brightness starting from the leading edge. This is in correlation with the Reynolds analogy as the skin friction rates are higher close to the leading edge where the boundary layer is thin, causing more efficient cooling than further downstream where skin friction rates decrease (see also Fig. 3.27). The gradual increase in temperature is followed by a sudden decrease further downstream (change from bright to dark) which corresponds to laminar-turbulent boundary-layer transition. As detailed in Sec. 1.2.1 the phenomenon does not occur at a specific chordwise location but has to be regarded as a process along a finite distance of the wall-bounded flow. Note

that the high spatial resolution of the presented results allows to distinguish individually fringed patterns in the transition regime. It should be pointed out that the high spatial resolution of the presented results allows to distinguish individually fringed patterns in the transition regime which are probably due to the three dimensional nature of the turbulent breakdown in the laminar flow [129].

To quantify the extent of laminar flow at a specific spanwise location, radial cuts of the TSP intensity ratio are extracted and analyzed as depicted in Fig. 3.8. The points defined as transition location $(x/c)_{\mathrm{tr}}$, onset $(x/c)_{\mathrm{tr,\,onset}}$ and end $(x/c)_{\mathrm{tr,\,end}}$ are then detected by the following algorithm using Matlab:

1. Smoothing of data by a cubic spline approximation using the function `csaps` and a smoothing parameter of $1 - 5 \times 10^5$

2. Identify $(x/c)_{\mathrm{tr}}$ at location of minimum gradient of spline

3. Identify $(x/c)_{\mathrm{tr,\,onset}}$ at intersection between the horizontal line through the curve maximum and the line through $(x/c)_{\mathrm{tr}}$

4. Identify intersection between the line through $(x/c)_{\mathrm{tr}}$ and the succeeding inflection point or local minimum as $(x/c)_{\mathrm{tr,\,end}}$

   Note: All slopes are determined according to the value of the first derivative of the spline at the detected points, respectively.

5. Repeat the procedure for 21 equidistant and adjacent radial cuts across 10 mm span, i.e. ~ 65 pixel in the image or ~ 42 nodes on the 3D grid, to obtain a mean value and a standard deviation of the detected locations.
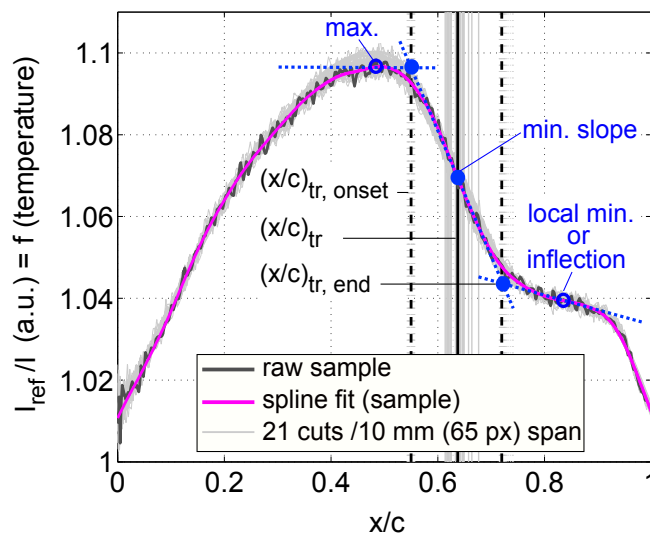
Figure 3.8: Chordwise sections of TSP results for systematic detection of locations defined as boundary-layer transition, onset and end.

According to Ashill et al. [5] the location of the steepest gradient of such a thermographic result is equivalent to the position where the root-mean-square value of an unsteady hot-film signal peaks when influenced by boundary-layer transition, [147]. Hence, the detected location corresponds to the position of 50 % turbulence intermittency [72] and is therefore a reasonable definition for the measured transition position. Similarly it has been argued that in a thermographic transition measurement the chordwise locations of the local maximum curvature upstream and downstream of $(x/c)_{tr}$ correlate with start and end points of the transition zone [5, 147]. The method used in this study is modified accordingly for the sake of robust automated data processing and is similar to the method described by Schülein [137].

3.3.2 Comparison of TSP and IR results

A data point at $Re_{tip} = 4.86 \times 10^5$ and $\beta_{root} = 11.8°$ was acquired by both TSP and IR and the results are presented in Fig. 3.9 *top* and *bottom*, respectively. To ease comparison, the markings applied to the TSP surface are added in red to the correspondint IR data. The TSP data comprises similar features as described above with respect to Fig. 3.7. To ease comparison between the two results, the markings used in the TSP result are added as red lines in the IR data below. Both results are remarkably similar. However, in addition to the noticeably stronger blur in the IR result the reduced image resolution does not resolve the fine structures in the boundary-layer transition region, which are visible in the equivalent TSP result. Note also the turbulent wedges at $r/R = 0.53$ and $r/R = 0.77$ in the IR result which are due to additional disturbances introduced by the pressure taps (0.3 mm diameter) at these locations which induce turbulent flow comparatively further upstream. Detailed investigation of the IR result reveals an upstream movement of transition of $\sim 5 - 10$ % chord across small spanwise stripes of $\Delta(r/R) \sim 0.02$ in the vicinity of $r/R = 0.6$ and $r/R = 0.68$. Photographs of the leading edge surface area from both measurements are provided in Fig. 3.10. Whereas the original blade surface exhibits abrasive regions from previous campaigns in the noted areas, the TSP surface allows polishing to obtain a homogeneous surface quality similar to the original model finish. Hence, the observed upstream movement of boundary-layer transition in the striped areas around $r/R = 0.6$ and $r/R = 0.68$ can be attributed to roughness induced receptivity. The phenomenon was similarly observed and has been described in more detail by Carpenter et al. [14].

The TSP and IR data presented in Fig. 3.9 are compared in more detail in Fig. 3.11. Tangential cuts are extracted at $r/R = 0.75$, where the IR signal is neither influenced by pressure taps nor by relatively increased surface roughness. Both signals have been post processed according to the procedure described in the previous section and the approximate spline fit as well as the detected transition regime are added to the graph. The evolution of the signals is qualitatively similar and the agreement between the detected positions for boundary-layer transition, onset and end are within one percent chord. Note also the slightly higher signal to noise ratio in the IR data. In addition to that a small peak is visible in the IR signal at $x/c < 0.1$. It can be attributed to residual disturbance light in the IR reflecting from the rounded blade leading edge into the camera sensor. Being often reported as a challenge in IR measurements, reflections could be minimized to the visible, yet insignificant peak which does not move downstream of $x/c = 0.1$ in the campaign as the collective
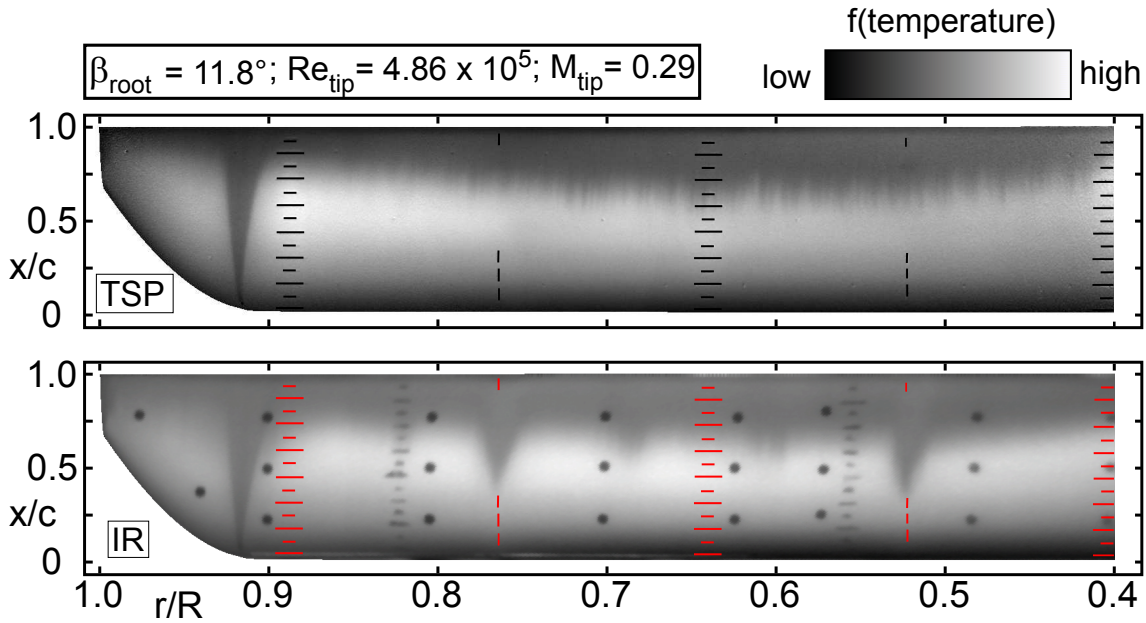
Figure 3.9: Comparison of transition results obtained via TSP (*top*) and IR (*bottom*) at same conditions. Markers in TSP result are sketched in red for the IR result to ease comparison.
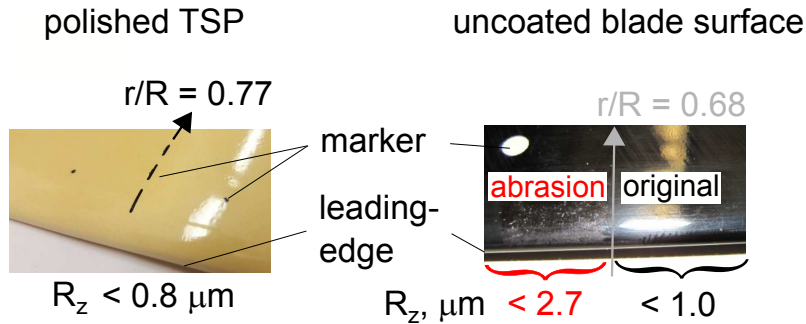
Figure 3.10: Close-up photographs of TSP surface *(left)* and uncoated blade surface *(right)* as used for IR measurements and corresponding mean roughness depths (peak-to-peak) R_z.

pitch is altered. All data points where IR measurements were encountered are compared to the equivalent data points obtained by TSP in Fig. 3.12. The graph shows the detected distinctive transition positions at $r/R = 0.75$ which are plotted against collective pitch at $Re_{tip} = 4.9 \times 10^5$ and $Re_{tip} = 7.3 \times 10^5$ in open and closed symbols, respectively. The overall comparability of the results is within 2 % of the chord. Hence, any differences possibly originating from the TSP coating itself or from data acquisition on the other blade can be neglected.

3.3.3 Effect of collective pitch, blade tip Mach and chord Reynolds number

A series of TSP results is presented in Fig. 3.13 for different collective pitch settings β_{root} at $Re_{tip} = 4.86 \times 10^5$. It can be deduced that boundary-layer transition moves upstream as the collective pitch is increased. Note the individually fringed transition patterns which alter depending
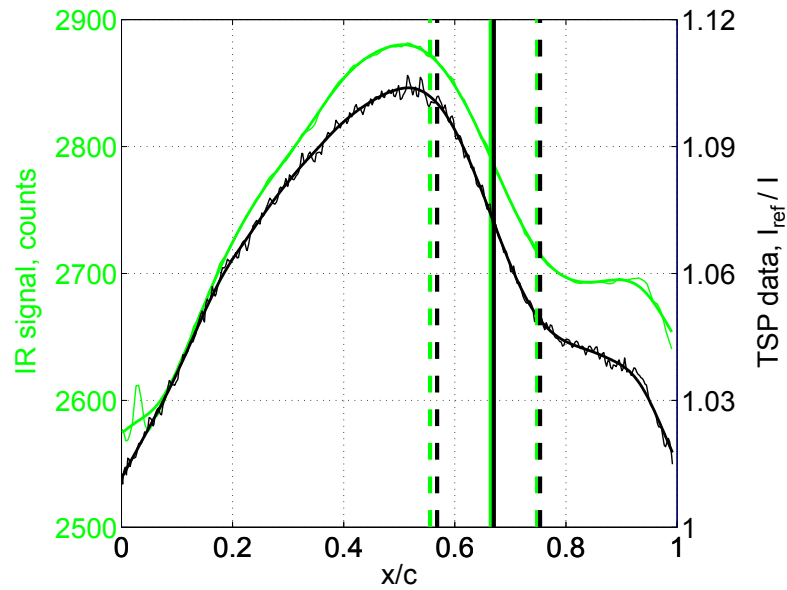
Figure 3.11: Comparison of post-processed IR and TSP signal at $r/R = 0.75$, $Re_{tip} = 4.86 \times 10^5$ and $\beta_{root} = 11.8°$. Raw signals are thin and spline fits are thick. Detected points of boundary-layer transition, onset and end are represented by vertical solid and dashed lines, respectively.
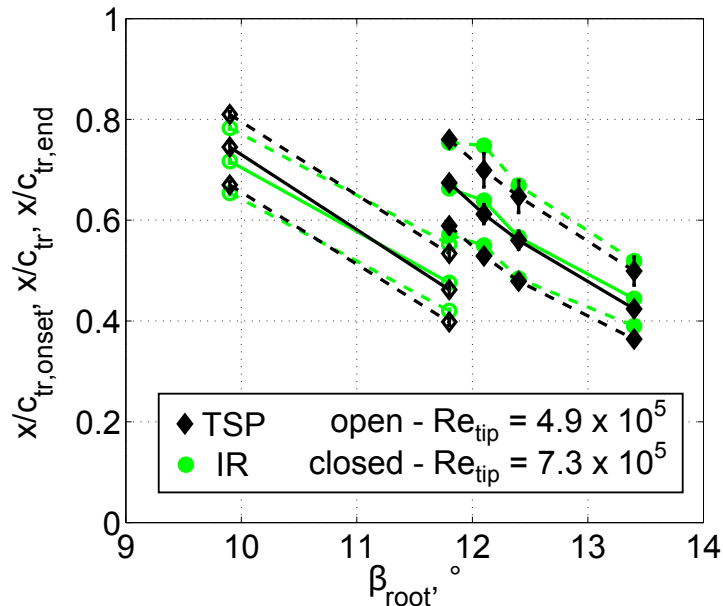
Figure 3.12: Comparison of measured transition regions at $r/R = 0.75$ against collective pitch for all data points measured by both IR and TSP.
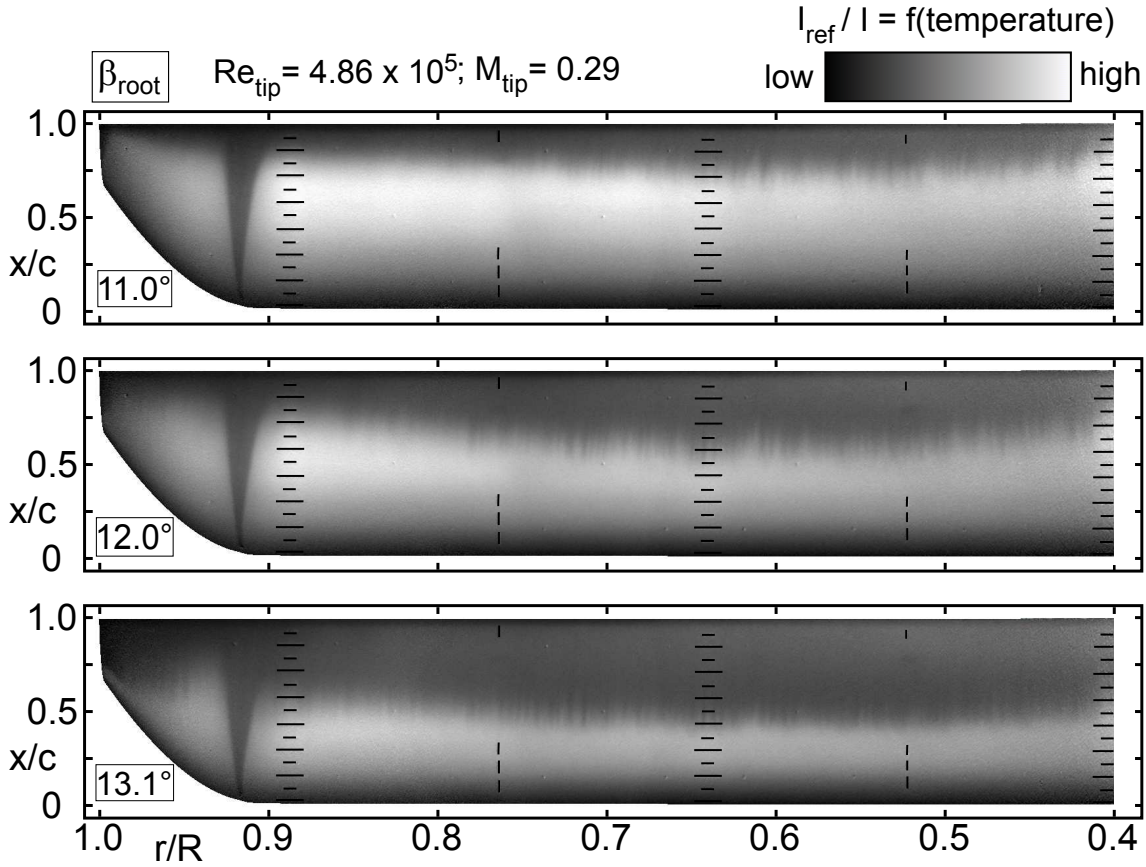
Figure 3.13: TSP transition results for different collective pitch settings β_{root} at blade tip Mach and chord Reynolds numbers of $M_{\text{tip}} = 0.29$ and $Re_{\text{tip}} = 4.86 \times 10^5$.

on the chordwise range where transition takes place.

The detected transition positions at $r/R = 0.77$ and $r/R = 0.53$ are plotted against collective pitch angle in Fig. 3.14 for all data points investigated. A consistent upstream movement of the detected transition position can be deduced at increasing collective pitch settings and increasing tip chord Reynolds number. The corresponding standard deviations are depicted as bands by thin solid lines indicating the scatter in the detected transition positions. The scatter is smaller than $\pm 2\%$ in x/c for all data points displayed. Note that this scatter contains physical information related to the three-dimensionality of the transition region across the spanwise 10 mm averaging interval such as the fringed patterns (see Fig. 3.13). The uncertainty with respect to the detection algorithm is expected to be smaller. This is suggested by the trend observed in Fig. 3.15 which displays zoomed-in data from Fig. 3.14. Note that the smallest detected systematic change of $(x/c)_{\text{tr}}$ with β_{root} is less than 1 % chord which is ~ 0.1 mm.

The curves in Fig. 3.14 corresponding to $Re_{\text{tip}} = 4.8 \times 10^5$ and $Re_{\text{tip}} = 7.3 \times 10^5$ both exhibit an increase in slope $(\delta (x/c)_{\text{tr}} / \delta \beta_{\text{root}})$ as the transition position moves upstream of $x/c \sim 0.75$. In turn, the slope decreases again as transition moves upstream of approximately $x/c \sim 0.5$. The change in transition position relative to the change of the pressure gradient on an airfoil is smaller
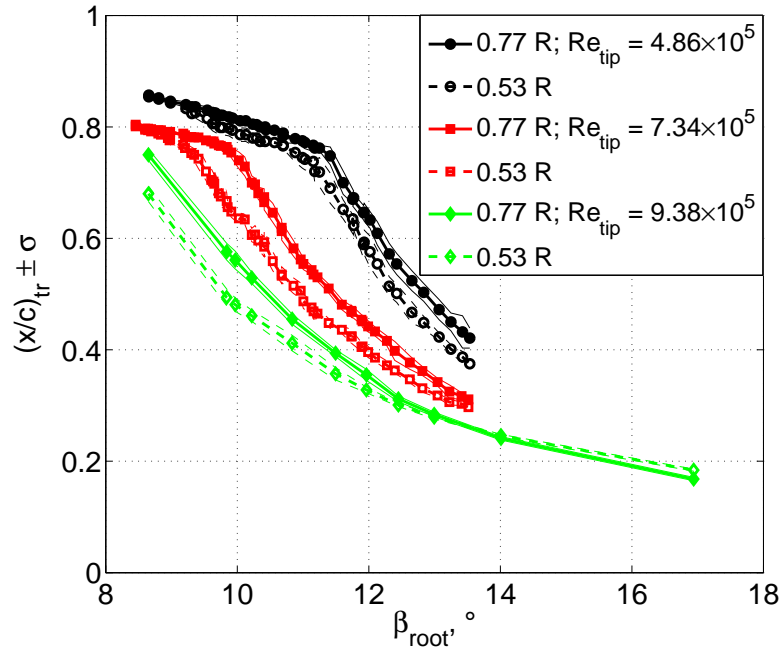
Figure 3.14: Detected transition positions at $r/R = 0.77$ and $r/R = 0.53$ vs. collective pitch for all data points.

in regimes where adverse pressure gradients are high as compared to areas with more moderate adverse pressure gradients or where the flow is accelerated [47]. Hence, the observed change in slope suggests that the pressure distribution on the DSA-9A airfoil exhibits stronger adverse pressure gradients at $x/c > 0.75$ than further upstream where $\delta\,(x/c)_{\mathrm{tr}}\,/\delta\beta_{\mathrm{root}}$ is larger. This is confirmed by the surface pressure investigations in Sec. 2 and in previous studies on the same airfoil [39]. The finding is further discussed in Sec. 3.4.1.

It is also noticeable that for most data points displayed in Fig. 3.14 the detected transition positions at $r/R = 0.53$ (open symbols) are further upstream compared to those detected at $r/R = 0.77$. A spanwise distribution of the detected transition positions including its onset and end are plotted for a sample data point in Fig. 3.16. The detected transition region covers about $15 - 20\,\%$ percent of the chord at each radial section and varies over $20\,\%$ in (x/c) across the span. The resulting spanwise transition position is influenced by various factors which partly counteract and therefore are hard to be isolated. An increase of relative Reynolds number towards the tip would cause transition to move upstream [129], whereas the negative blade twist leads to radially decreasing angles of incidence, therefore to more moderate pressure gradients causing a longer extent of laminar flow [136]. Additionally, transition is influenced by the induced downwash velocity of the tip vortex especially close to the blade tip, which is noticeable for $r/R > 0.9$ in Fig. 3.16.

The effect of collective pitch on the radial distribution of $(x/c)_{\mathrm{tr}}$ at constant $Re_{\mathrm{tip}} = 7.3 \times 10^5$ is presented in Fig. 3.17. As compared to the case shown in Fig. 3.16, the transition line is more two dimensional for $r/R < 0.9$ at all collective pitch settings displayed. An upstream movement of boundary-layer transition can be deduced as β_{root} is increased. Similar to the observed change of the
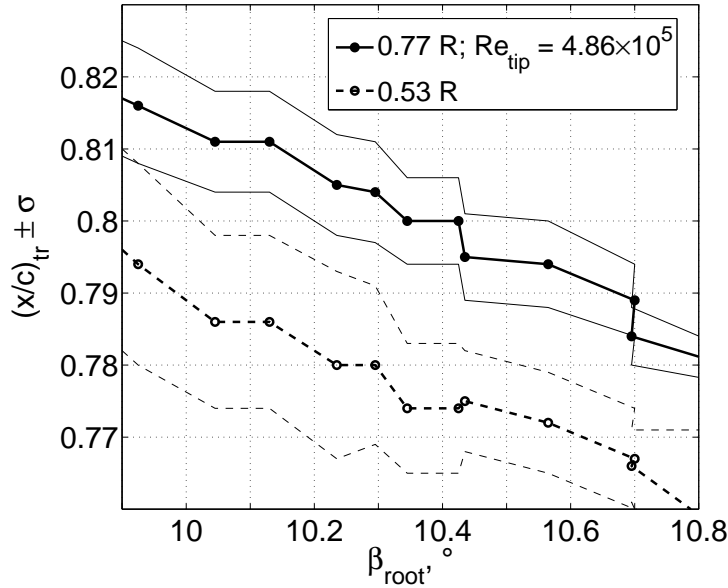
Figure 3.15: Zoom into Fig. 3.14, systematic changes of $\Delta(x/c)_{tr} \sim 1\%$ can be detected.

slope ($\delta(x/c)_{tr}/\delta\beta_{root}$) in Fig. 3.14 the incremental upstream movement of transition decreases, despite equidistant steps in β_{root}, as transition passes $x/c \sim 0.5$ which is due to the changing pressure gradients on the airfoil [47]. Moreover, as the blade loading is increased, a qualitative change in the detected positions can be observed at the blade tip and chordwise maxima are visible at $r/R = 0.94$ for $\beta_{root} \geq 11.4°$. Following the argumentation of Tanner and Yaggy [151], the effect might be explained by the contraction of the slipstream, where "the tip vortex creates an increase in angle of attack outboard of the contracted slipstream and a decrease inboard" [151]. For further insight in this respect, smoke visualizations of the tip vortex dynamics or velocity field measurements via particle image velocimetry are recommended (see e.g. [164]).

The effect of tip chord Reynolds number on the radial distribution of $(x/c)_{tr}$ at constant blade loading of $C_T/\sigma = 0.010$ is presented in Fig. 3.18. As expected from linear stability theory, boundary-layer transition moves upstream as the Reynolds number is increased, [129]. At $r/R > 0.88$ the transition position is influenced by the tip vortex and the radial trend is similar as for the lowest two collective pitch settings in Fig. 3.17. The tip vortex induces a downwash and eventually leads to lower effective angles of attack and therefore to boundary-layer transition further downstream. The effect is more dominant at higher Re_{tip}. The findings from Mahalingam et al. [94] imply that, according to the Kutta-Joukowski theorem, the tip vortex strength (in terms of circulation Γ) scales according to $\Gamma \propto Re_{tip} \cdot C_T/\sigma$ if a linear relationship between C_T/σ and the geometric angle of incidence as well as constant viscosity are presupposed. This relationship explains the observed trends in Fig. 3.17 and Fig. 3.18 as stronger tip vortices induce larger velocities according to the Biot-Savart law.

The combined effect of changing Re_{tip} and C_T/σ on the spanwise evolution of the distinctive boundary-layer transition points is shown in Fig. 3.19. The data points displayed were chosen according to their similarity in $(x/c)_{tr}$ at $r/R = 0.77$. The curves coincide for the most part of the

span and no influence on the length of the transition region can be deduced. The lines for the two larger Re_{tip} are similar close to the blade tip. In contrast the transition line at $Re_{\text{tip}} = 4.86 \times 10^5$ reveals stronger radial variations (also at $r/R < 0.48$) and seems to be stronger influenced by the tip vortex. Though differences are small, the observation is in line with the scaling of the tip vortex strength as suggested by Mahalingam et al. [94] as the product between Re_{tip} and C_T/σ is greatest for $Re_{\text{tip}} = 4.86 \times 10^5$ amongst the cases displayed.
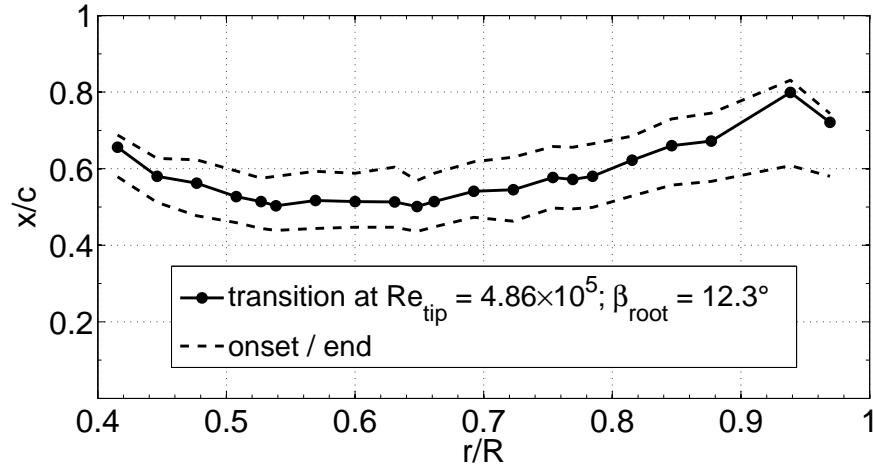
Figure 3.16: Detected points of boundary-layer transition, onset and end at $Re_{\text{tip}} = 4.8 \times 10^5$ and $\beta_{\text{root}} = 12.3°$.
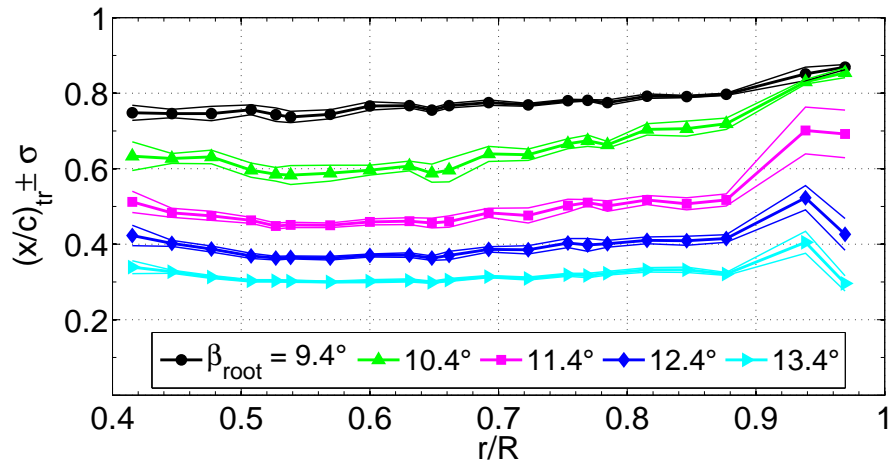
Figure 3.17: Influence of collective pitch on spanwise transition positions at constant tip chord Reynolds number of $Re_{\text{tip}} = 7.3 \times 10^5$.

Experimental data for selected measurement points is listed in Appendix A. The data include measurement conditions, integral thrust readings, measured surface pressures at $r/R = 0.53$ and $r/R = 0.77$ as well as transition data, which consists of the TSP results and the detected transition region, respectively.
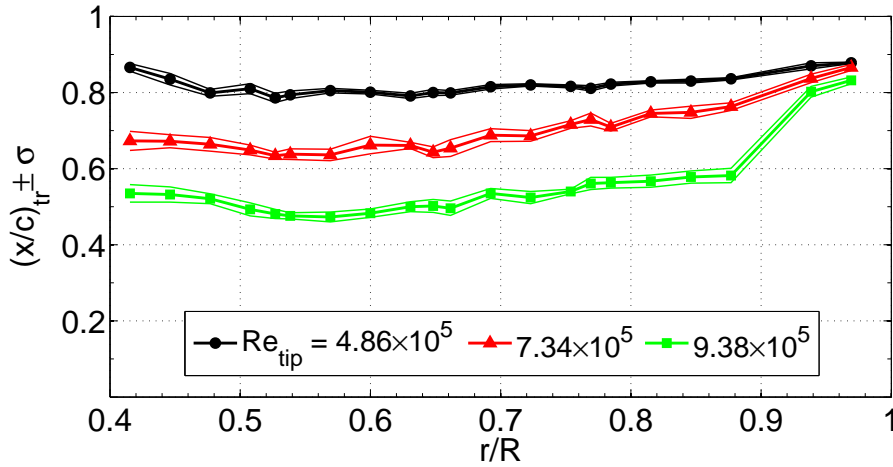
Figure 3.18: Influence of tip chord Reynolds number on spanwise transition positions at constant blade loading of $C_T/\sigma = 0.010$.
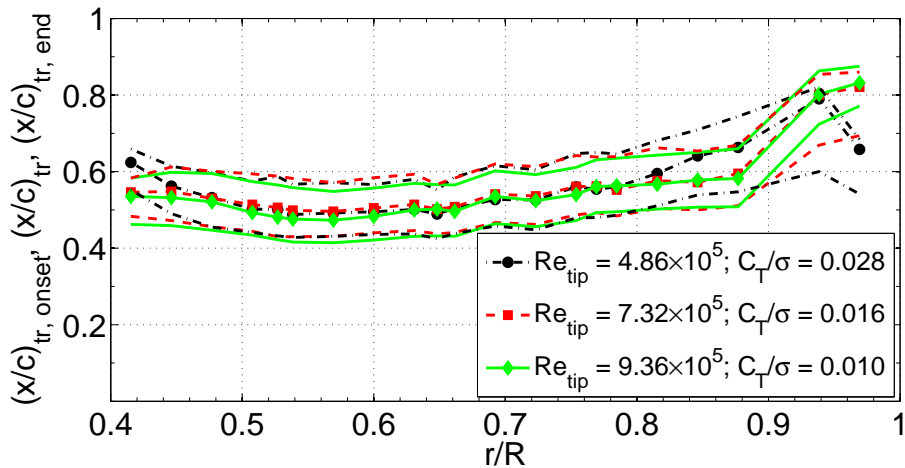
Figure 3.19: Combined effect of tip chord Reynolds number and blade loading (Re_{tip} and C_T/σ) on radial distribution of distinctive points for boundary-layer transition of data points with similar $(x/c)_{\text{tr}}$ at $r/R = 0.77$.

3.3.4 Investigation of effect of rotational forces

The effect of rotational forces on boundary-layer transition is studied by comparison of detected transition positions at a systematic variation of the Rossby number Ro. In Sec. 1.2.3 Ro^{-1} has been identified as the relevant scaling parameter for the relative contribution of rotational forces on the flow [80]. According to Eq. 1.22 Ro^{-1} is defined as:

$$\frac{1}{Ro} = \frac{\Omega^2 \tilde{r} c}{u_{res}^2} = \frac{(2\pi f_{\text{rotor}})^2 \tilde{r} c}{u_\infty^2 + (2\pi f_{\text{rotor}} \tilde{r})^2} = \frac{1}{\tilde{J}^2 + 1} \cdot \frac{c}{\tilde{r}} \tag{3.2}$$

In this equation $\tilde{r}$ is the characteristic radial position where rotational forces are investigated and $\tilde{J}$ is the advance ratio based on the corresponding rotation speed. In this investigation it is attempted

to vary the relative contribution of rotating forces by changing the Rossby number exclusively. At the same time it is desired to leave the effect of viscous forces and compressibility in terms of Re and M as well as the influence of pressure forces in terms of c_p unaltered. For the investigated configuration the corresponding parameter variation is realized by comparing transition positions detected at $r/R = 0.77$ and $f_{\text{rotor}} = 23.6\,\text{Hz}$ with those obtained at $r/R = 0.53$ and $f_{\text{rotor}} = 35.4\,\text{Hz}$. Using this method the corresponding Reynolds and Mach number, based on the resultant velocity u_{res} (see Eq. 3.2), are unchanged while the Rossby number is altered by the varying radial position.

The resulting test conditions for the investigation of the effect of Rossby number on boundary-layer transition are listed in Table 3.2. Note that due to the low and similar values of the relative advance ratios $\tilde{J}$ the variation of Ro is mainly accomplished by a variation of $\tilde{r}/c$.

Table 3.2: Test conditions for investigation of rotational effect on boundary-layer transition

Ro	f_{rotor}, Hz	r/R	$\tilde{r}/c$	$\tilde{J}$	Re_{res}, 10^5	M_{res}	β_{root}, °
6.95	23.6	0.77	6.94	0.0281	3.73 ± 0.03	0.220	9.9-13.5
4.76	35.4	0.53	4.76	0.0258	3.75 ± 0.10	0.226	8.5-11.7

To exclude an effect of different pressure forces, the comparison of transition positions should be carried out at the same effective angle of attack. As it is hard to measure the effective angle of attack directly, the concept of a "c_p-pair" is introduced. Considering that the effective angle of attack directly affects the resulting surface pressures, the different radial positions for the variation of Ro are chosen according to the locations of available surface pressure data, which limits the range of investigated Rossby numbers in this study. In this respect, a c_p-pair denotes two data points at which the respective collective pitch angle β_{root} causes the same pressure distribution at $r/R = 0.77$ and $f_{\text{rotor}} = 23.6\,\text{Hz}$ as at $r/R = 0.53$ and $f_{\text{rotor}} = 35.4\,\text{Hz}$. The data pair then corresponds to the Rossby numbers $Ro = 6.95$ and 4.76, respectively, and allows a comparison of $(x/c)_{\text{tr}}$ at same Reynolds and Mach number, as well as at same surface pressures but at different contributions of rotational forces as expressed by the levels of Ro. The range of tested collective pitch settings for each Ro-condition is given in Tab. 3.2. It is a subset of all acquired data points which are listed in Tab. 3.1.

Measured surface pressures of a sample c_p-pair are presented in Fig. 3.20. The bar sizes indicate the 65 % confidence interval, $\pm\sigma_{c_p}$, of the corresponding pressure readings. As indicated by the red arrows, there are three chordwise positions where pressure tap data is available at both radial sections for comparison. The criterion for a matching pressure distribution is that the differences between the mean values of each of the corresponding chordwise pressure readings is less than the lower value of the associated standard deviations σ_{c_p}. In all cases the values of σ_{c_p} are less than ≈ 0.02.

The detected spanwise transition positions for the c_p-pair displayed in Fig. 3.20 are presented in Fig. 3.21. Vertical lines mark the radial positions of the measured pressures which were found to coincide in Fig. 3.20 and which correspond to the different Rossby numbers as indicated.

The transition positions of all c_p-pairs found are compared between the two Rossby numbers in
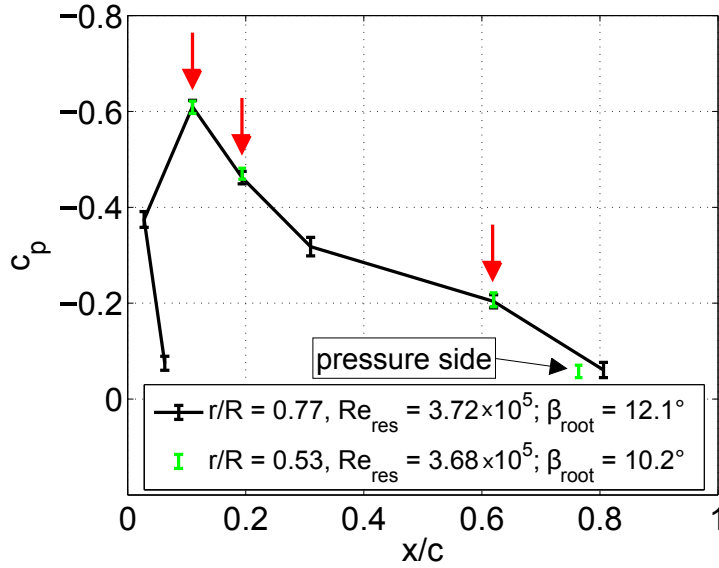
Figure 3.20: Sample c_p-pair suited for investigation of rotational effect. The cases exhibit different Rossby numbers Ro, yet the same Reynolds numbers and effective angles of attack.

Fig. 3.22. A total of 16 data pairs were found within the tested range of β_{root} at the corresponding Rossby numbers (see Tab. 3.2) where the measured boundary-layer transition can be compared exclusively with respect to the effect of rotational forces. Neither the collective pitch angles nor the integral blade loading of the corresponding c_p-pair data points are the same. For this reason, the corresponding pairs are simply numbered and sorted according to the associated collective pitch setting in ascending order for the plot in Fig. 3.22. A comparison of the corresponding transition positions for the two Rossby numbers reveals no distinguishable differences. In fact, the detected transition positions at both Rossby numbers agree to within the margin spanned by the corresponding standard deviations. Hence, an effect on the chordwise extent of laminar flow, due to the exclusive change of the relative contribution of rotational forces, can be excluded. This is the case for all displayed cases, i.e. where transition occurs in the range between $0.4 < (x/c)_{tr} < 0.8$.

It should be underlined that the presented data for the variation of Rossby number is not biased by an effect of the acting viscous forces. Therefore, the chord Reynolds numbers corresponding to the c_p-pair data points used to investigate the rotational effect in Fig. 3.22 are plotted in Fig. 3.23. Although deviations in the associated Reynolds numbers exist, they are only in the order of 2 - 3 %. And more important, it can be deduced that the deviations in Re_{res} between the investigated Rossby numbers do not systematically correlate with the differences in the detected transition positions of the corresponding c_p-pairs, which are insignificant. It can therefore be concluded that the investigation of rotational effects on boundary-layer transition is not biased by the measured differences in chord Reynolds number which are therefore negligible.
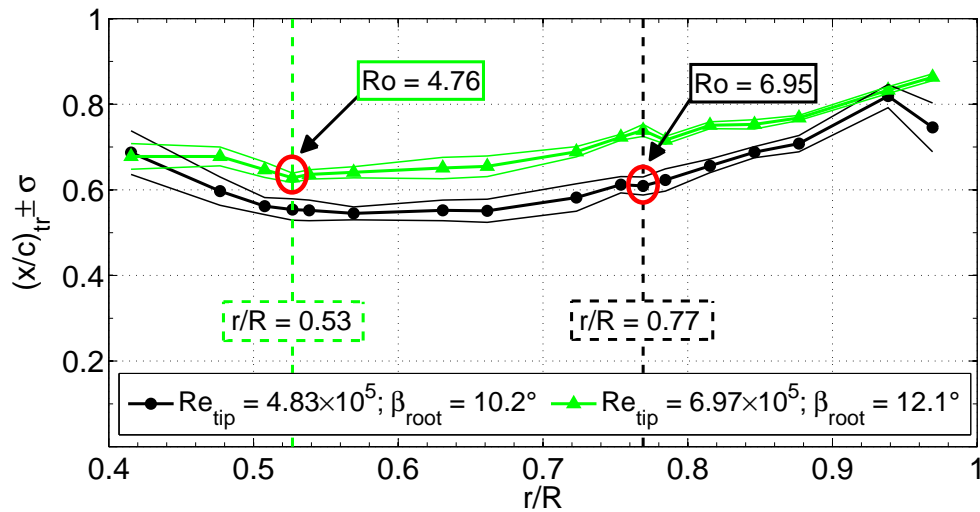
Figure 3.21: Detected boundary-layer transition positions for the c_p-pair presented in Fig. 3.20. Transition positions dedicated for comparison with respect to an effect of rotational forces are highlighted in red.
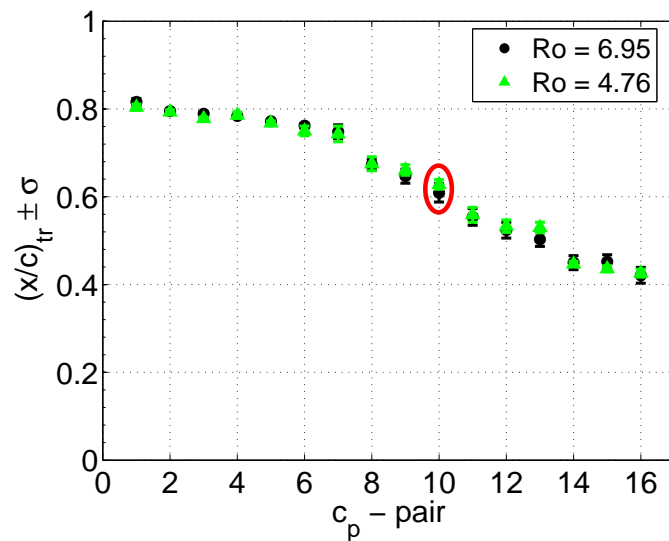
Figure 3.22: Effect of Rossby number on boundary-layer transition for all c_p-pairs denoting comparable surface pressures as well as similar resultant chord Reynolds and Mach numbers. Data points presented in Fig. 3.20 and Fig. 3.21 are highlighted by the red ellipse.

3.3.5 Relative effect of non-adiabatic wall temperature

For wall-bounded flows in air a heating of the surface creates a viscosity gradient close to the wall which destabilizes the boundary-layer [129] eventually causing premature transition as for instance observed by Fisher and Dougherty [37]. When comparing different data points in this campaign with respect to each other it has to be ensured that the blade heating does not introduce a
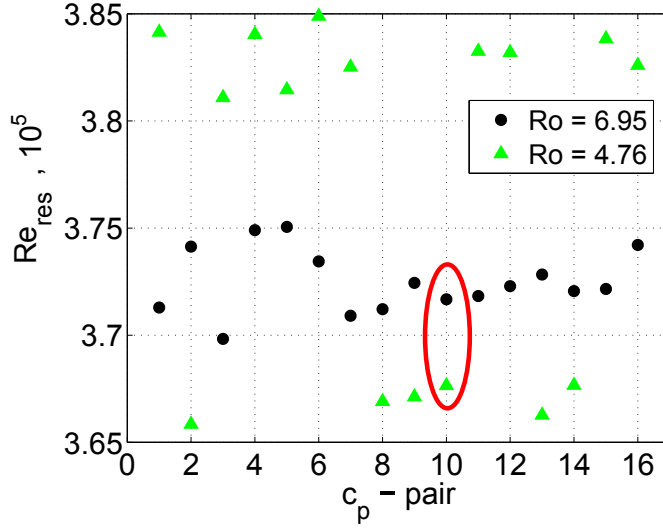
Figure 3.23: Resultant chord Reynolds numbers for c_p-pairs used for investigation of rotational effect. Data for points presented in Fig. 3.20, 3.21 and 3.22 are highlighted by red ellipse.

bias. Especially in view of the investigation of the effect of rotational forces it should be affirmed that the employed blade heating does not have a different effect on boundary-layer transition when comparing for instance data points at different rotating speeds against each other. In order to obtain the non-adiabatic wall temperature from the presented intensity ratios the Ru(phen) based TSP sensor was calibrated prior to the test. TSP intensity values and temperatures are related by the following calibration polynomial:

$$\frac{I_{ref}}{I} = \sum_{i=0}^{2} a_i \left(\frac{T}{T_{ref}}\right)^i \tag{3.3}$$

In this equation a_i are calibration coefficients and T_{ref} is the temperature distribution on the blade surface at reference conditions, i.e. without additional blade heating (see Fig. 3.5). The temperature sensitivity in terms of "percentage intensity change - per - Kelvin" comprises 2.3 %/K at 293 K and 100 kPa. The reference temperature distribution is presumed to satisfy the two-dimensional relation for the adiabatic wall recovery temperature T_{aw} (see Eq. 3.4) as it is applied above for the temperature correction of surface pressure investigations with PSP on the same configuration (see Sec. 2.2.5) as well as on helicopter rotor investigations in forward flight condition [21].

$$T_{ref}(r) \equiv T_{aw} = T_\infty + \frac{\gamma - 1}{\gamma} r(Pr) \cdot \frac{\left(v_\infty^2 + (2\pi f_{rotor} r)^2\right)}{\gamma R_{air}} \tag{3.4}$$

In this equation γ and R_{air} are the ratio of specific heats and the gas constant for air calculated at measured inflow conditions. The recovery factor $r(Pr)$ is considered for a laminar boundary-layer at a Prandtl number of $Pr = 0.72$, i.e. $r(Pr) = 0.85$ [30]. T_∞ is obtained by anchoring $T_{ref}(r)$ at $r/R = 0.65$ where the temperature was measured by the Pt100 probe and setting $T_{ref}(0.65\, R) \equiv T_{Pt100}$. The surface temperature is then obtained by solving the calibration polynomial in Eq. 3.3.

The assumption of a constant recovery factor along the chord is a simplification and introduces an uncertainty because the turbulent recovery factor is slightly higher (≈ 0.90 [30]) than the corresponding laminar value and it is not a priori known whether the temperature probe reading is obtained within a laminar or turbulent flow regime. However, the natural difference in the viscous heating is more than an order of magnitude less than the temperature difference obtained by heating up the blade by the halogen spot lights. Therefore, the uncertainty introduced by the deviation of T_{aw} can be neglected. Moreover, the effect of surface heating on premature transition depends rather on the non-adiabatic wall temperature ratio than on absolute values. A relation for the relative decrease of transition Reynolds number (with the transition position as reference length) due to non-adiabatic surface temperatures is reported by Fisher and Dougherty [37]:

$$\frac{Re_{x_{\mathrm{tr}}}}{Re_{x_{\mathrm{tr,aw}}}} = \left(\frac{T_{\mathrm{w}}}{T_{\mathrm{aw}}}\right)^{-7} \tag{3.5}$$

The relation was found from transition measurements in flight tests and wind tunnel experiments on a 10° cone which was investigated at zero and small angles of incidence. Costantini et al. [17] showed that the destabilizing effect is significantly weaker if transition occurs in adverse pressure gradient regions as it is the case in the present study. For this reason Eq. 3.5 can be regarded as an upper limit when estimating the relative change of transition positions due to non-adiabatic wall heating in the present study.

In order to investigate the consistency of the applied heating, the non-adiabatic wall temperature ratio $T_{\mathrm{w}}/T_{\mathrm{aw}}$ was calculated from the intensity ratios by solving the calibration polynomial for T/T_{ref} (Eq. 3.3 with $T_{\mathrm{w}}/T_{\mathrm{aw}} \equiv T/T_{\mathrm{ref}}$) and assuming Eq. 3.4 for T_{ref}. The wall temperature ratio is extracted as average value of a 25×25 nodes region of interest inside the turbulent wedge at $r/R = 0.92$ (see Fig. 3.7). In this way it is ensured that the values to be compared are all extracted at similar, that is fully turbulent, conditions. The extracted values are plotted in Fig. 3.24 against collective pitch for all data points investigated. It can be deduced that the wall temperature ratio is shifted towards higher values as the tip Reynolds number is decreased. The finding satisfies the expectation that the blades are cooled down faster at higher rotation rates. Since the heated TSP images are acquired right after heating was applied, i.e. while the flow is cooling the blade surface, the non-adiabatic wall temperature ratios are comparatively lower at higher Re_{tip}. Recall that the data points considered for the investigation of rotational effects (in Fig. 3.22) are extracted out of the series at $Re_{\mathrm{tip}} = 4.86 \times 10^5$ and 7.34×10^5, respectively. The different temperature ratio levels are approximated in Fig. 3.24 by the dashed lines at $T_{\mathrm{w}}/T_{\mathrm{aw}} \approx 1.006$ and 1.004 for the lower and higher rotating speed, respectively.

Considering the approximated values for the wall temperature ratios in the relation 3.5, the relative difference in transition position between $Re_{\mathrm{tip}} = 4.86 \times 10^5$ and 7.34×10^5 is about 1 % of the chord. This is in the range of the reported precision of the transition position detection in this study. Therefore it is assumed that the blade heating does not have a relative influence when comparing the obtained transition data against each other. The absolute influence of the measured non-adiabatic wall temperatures is addressed in section 3.4.2.
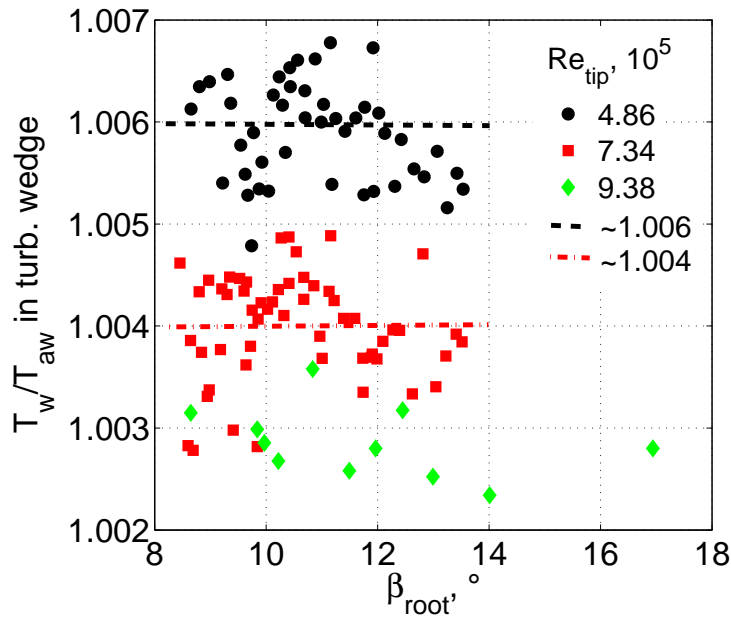
Figure 3.24: non-adiabatic wall temperature ratio T_w/T_{aw} evaluated within the turbulent wedge at $r/R \approx 0.92$ against collective root pitch for all data points investigated.

3.4   Comparison to 2D computations employing LST for transition prediction

Based on the results discussed in the previous section, a stabilizing effect of rotational forces on boundary-layer transition is insignificant for the investigated configuration. It is therefore inferred that influences of rotation on the three-dimensional deformation of the boundary-layer itself, i.e. centrifugal pumping (see Sec. 1), and on the corresponding stability characteristics are small. For this reason the investigation in the following section intends to compare the experimental results to numerical simulations which are inherently limited by two-dimensional assumptions for both boundary-layer flow and the corresponding stability characteristics. More precisely, the capabilities of industry-oriented numerical tools are exploited in order to

- Check the agreement between measured and calculated surface pressures and

- To investigate the coherence of measured boundary-layer transition data with numerical simulations based on two different e^N-methods, both in the framework of 2D local LST.

The comparative study is performed for experimental data extracted at 77 % of the blade span. It corresponds to the location where, in addition to measured transition positions, most data is available from pressure transducers (see Fig. 2.12). However, also at $r/R = 0.77$ the spatial resolution of pressure sensors is insufficient to prescribe the streamwise pressure gradients needed as boundary condition for an appropriate boundary-layer solution (see Eq. 1.4). For this reason, measured surface pressures are assimilated by numerical computations using the 2D transonic Euler-/ boundary-layer code MSES [25]. The tool was originally developed for airfoil design purposes [23, 44, 45] and allows robust and automated analyses of aerodynamic airfoil characteristics

at short computing time. According to Smith et al. [144] MSES yields similarly accurate results in terms of integral lift and drag predictions when compared to more sophisticated Navier-Stokes solvers, especially at subcritical Mach numbers ($M < 0.6$) and under attached flow conditions.

The flow solution in MSES which best resembles the experimentally obtained surface pressures is then used for further analysis aiming to find transition N-factors using two different methods, both based on two-dimensional linear stability theory (2D LST). The first approach is implemented in MSES directly. In this work it is referred to as the *approximate e^N-method* as being a simplified version of the originally proposed procedure by van Ingen [60] and Smith and Gamberoni [143] (see also Sec. 1.2.1). Implementation of the approximate method is described in detail by Drela and Giles [26] and briefly outlined in Sec. 3.4.1. The second approach is in line with the originally proposed procedure by van Ingen [60] and Smith and Gamberoni [143]. It is therefore denoted as the *original e^N-method* for better distinguishability from the former. The original method employs the compressible boundary-layer solver COCO [133] and the linear stability equation analysis tool LILO [134] both of which are further described in Sec. 3.4.2. Both COCO and LILO are currently applied in research and industry. For instance, the tools are employed as essential elements of the transition prediction module [74, 75] implemented in the state-of-the-art Navier-Stokes solver TAU [139] of the German Aerospace Center (DLR). The module is employed for automated transition detection of flows over complex three-dimensional, yet non-rotating, aircraft geometries and has matured for industrial applications [73].

Other than being based on the same pressure distribution, there is no direct coupling between results obtained from MSES and the solutions of the boundary-layer flow in COCO along with the resulting stability characteristics calculated in LILO. In fact, the results in terms of the critical transition N-factor are expected to disagree because of the differences in the applied procedures and the involved flow assumptions (see Sec. 3.4.3).

3.4.1 Coupled Euler-/boundary-layer computations

Calculation of surface pressures   In MSES the flow domain is divided into the viscous boundary-layer and the inviscid potential flow. The inviscid part is described by the compressible Euler equations in integral form for steady 2D flow. The exact equations are described by Giles and Drela [44]. The flow variables are discretized on an intrinsic streamline grid and the streamlined coordinate system allows for automated grid generation and adaptation to alternating flow conditions, e.g. at changing angles of attack, which speeds up the computations. The viscous boundary-layer flow is described by a compressible two equation integral formulation as detailed by Drela and Giles [26]. The laminar and turbulent boundary-layer solutions depend on the shape factor H_{12}, the momentum thickness δ_2, the corresponding Reynolds number Re_{δ_2} and the Mach number at the boundary-layer edge. The closure relations for the laminar boundary-layer, which describe the inter-dependencies of the remaining unknowns in the governing equations, are based on boundary-layer solutions relying on the Falkner-Skan velocity profile family [34]. Boundary-layer transition is modeled with an approximate e^N-method which is part of the laminar boundary-layer formulation and briefly outlined in the next section. The turbulent formulation comprises an extra "lag" equation which accounts for lags in the response of the turbulent stresses and in principle

models the turbulent intermittent region as the flow changes from laminar to turbulent. More detailed information on the exact closure relations for both laminar and turbulent boundary-layers as well as the corresponding discretized equations are provided by Drela and Giles [26]. The solutions of the Euler and boundary-layer equations are obtained simultaneously and they are fully coupled via the displacement thickness δ_1 (see Eq. 1.9), which poses the lower boundary of the inviscid domain when added to the prescribed airfoil contour.

The *approximate* e^N - method in MSES   In MSES the laminar boundary-layer is locally prescribed by a profile corresponding to the family of one-parametric Falkner-Skan solutions [34]. The free parameter defines the shape of a self-similar profile and is related to the streamwise pressure gradient, which in turn is also manifested in the shape factor H_{12} (see Sec. 1.2.1). The approximate e^N-method in MSES makes use of a database comprising the stability characteristics of the Falkner-Skan profile family. The database has been computed in advance and is accessed during the integral boundary-layer computation using the local shape factor H_{12} and the momentum thickness Reynolds number Re_{δ_2} as coupling parameters. Re_{δ_2} expresses the dependency on the streamwise coordinate and is defined as $Re_{\delta_2} = u_e \delta_2 / \nu$, where u_e denotes the velocity at the boundary-layer edge. Growth rates of amplified instabilities are obtained from solutions of the Orr-Sommerfeld equations [104, 145] according to 2D local incompressible LST for many different self-similar Falkner-Skan profiles, corresponding to many different values of H_{12}, and integrated along increasing Re_{δ_2}. Following the idea of Gleyzes et al. [46] the envelopes of integral growth rates at constant H_{12} are approximated for different amplified frequencies by straight lines according to:

$$N(Re_{\delta_2}, H_{12}) = \left[\frac{\mathrm{d}N}{\mathrm{d}Re_{\delta_2}} (H_{12}) \right]^* \left[Re_{\delta_2} - Re_{\delta_{2_0}} (H_{12}) \right] \tag{3.6}$$

The zero crossing $Re_{\delta_{2_0}} (H_{12})$ corresponds to the momentum thickness Reynolds number at the indifference point, denoted by the subscript $_0$, which is the starting point of the streamwise integration of growth rates. Both slope and zero crossing are empirical relations entirely dependent on H_{12} and explicitly formulated in [26]. The asterisk * in Eq. 3.6 denotes a value from a straight line approximation of the envelope of integral growth rates for several different frequencies at constant H_{12} as sketched in Fig. 3.25a. By this method, the frequency dependency of integrated growth rates is lost. The loss of information on the unstable frequencies poses the major difference to the original e^N-method. Equation 3.6 holds for self-similar flows. In practice however, e.g. for the flow over an airfoil, H_{12} changes constantly and the flow is not self-similar. The actual envelope curve is obtained from an integral of the estimated slopes in Eq. 3.6 along the streamwise distance x according to:

$$N(x) = \int_{x_0}^{x} \left[\frac{\mathrm{d}N}{\mathrm{d}Re_{\delta_2}} (H_{12}) \right]^* \frac{\mathrm{d}Re_{\delta_2}}{\mathrm{d}x} \mathrm{d}x \tag{3.7}$$

Transition sets in if the threshold N_{cr} is reached. In the equation above the derivative of Re_{δ_2} with respect to x is obtained directly from the governing integral momentum equation (see [19]). As reported in [26] integration over the streamwise distance rather than over Re_{δ_2} (as in [46]) allows to determine integrated growth rates over the laminar portion of a separation bubble in a more realistic fashion.

The described envelope method was analyzed by Dini et al. [20]. As it can be inferred from Eq. 3.6 linearly approximated integral growth rates are equivalent to the original integral growth rates for self-similar flows, i.e. at constant H_{12}, with existing deviations due to the linear approximation only. Differences are large in vicinity of the indifference point. However, a systematic deviation to the original envelopes is introduced for non-similar flows with changing values for H_{12}. This is in principal due to the loss of frequency information of the integrated growth rates. The systematic deviation is demonstrated in [20] and nicely illustrated by Lutz [90] using the extreme example of a step increase of the shape factor H_{12} in streamwise direction along Re_{δ_2}, see Fig. 3.25b.
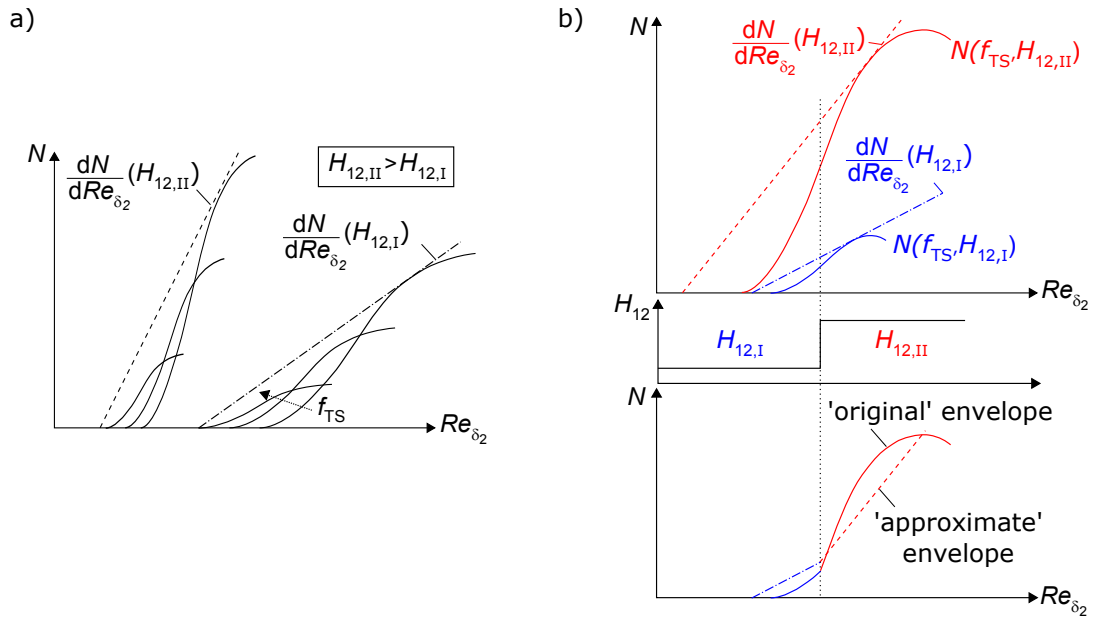
Figure 3.25: *a)* Linear approximation of maximum integral growth rates of TS waves as originally proposed by Gleyzes et al. [46] *b)* Sketch illustrating systematic deviation of approximate e^N-method to the original method by means of a step increase in H_{12}, according to [90]

For a disturbance of given frequency f the original amplification curve $N(f_{TS})$ is composed of parts corresponding to $N(f_{TS}, H_{12,I})$ and $N(f_{TS}, H_{12,II})$. Application of the approximate envelope method would yield the dashed envelope which is flatter than the curve using the original method. Dini et al. [20] state that if a monotonically increasing shape factor is approached by the approximate envelope method using a series of infinitesimally small steps in H_{12}, "the resulting growth of N will never be able to catch up with the value obtained from a self-similar profile at the same local shape factor and Reynolds number". In Fig. 3.25b the values "obtained from a self-similar profile at same local shape factor and Reynolds number" correspond to the values of $N(f_{TS})$ denoted by the solid red curve downstream of the step. For this reason the approximate envelope method systematically underestimates N_{cr} at increasing H_{12} which corresponds to streamwise decelerated flows. The opposite holds for streamwise accelerated flows at decreasing H_{12}, where N_{cr} is overestimated by the approximate method.

Because the critical N-factor as obtained by the approximate envelope method depends on the evolution of H_{12}, which in turn is a function of the pressure distribution, it is concluded that N_{cr}

from MSES is a characteristic parameter depending on e.g. the employed airfoil on which transition is investigated. This is confirmed by experimental investigations of Würz [168]. He showed that application of the approximate envelope method on different airfoils, but investigated under similar flow conditions, showed higher scatter in N_{cr} than the application of the original e^N-method.

Results   In Fig. 3.26 measured surface pressures at $r/R = 0.77$ are plotted as c_p against x/c for a sample data point at $\beta_{root} = 12.3°$ and at a rotating speed corresponding to resulting Reynolds and Mach numbers of $Re_{0.77R} = 3.75 \times 10^5$ and $M_{0.77R} = 0.22$. Computations were performed at these conditions for various angles of attack α_{MSES} and critical N-factors. The best fit between experimental and calculated pressures was found at $\alpha_{MSES} = 1.05°$. The corresponding numerical pressure distributions are added to the graph for three different values of N_{cr}. The overall influence of N_{cr} on the pressure distribution is small, yet an upstream movement of a "kink" can be distinguished between $0.45 \leq x/c \leq 0.62$ as N_{cr} is reduced. This feature is attributed to the sudden thickening of the boundary-layer resulting from laminar-turbulent transition [114]. The calculated results for all three critical N-factors presented fit the pressure tap readings to within the bar sizes which indicate the measured standard deviation in c_p (σ_{c_p} is in less than 0.02 for all cases). An assertion on the critical N-factor based on the pressure data presented in Fig. 3.26 is therefore not feasible. Instead, a comparison of the independently obtained surface temperature to the numerical skin friction results is better suited to provide an estimate of the critical N-factor.
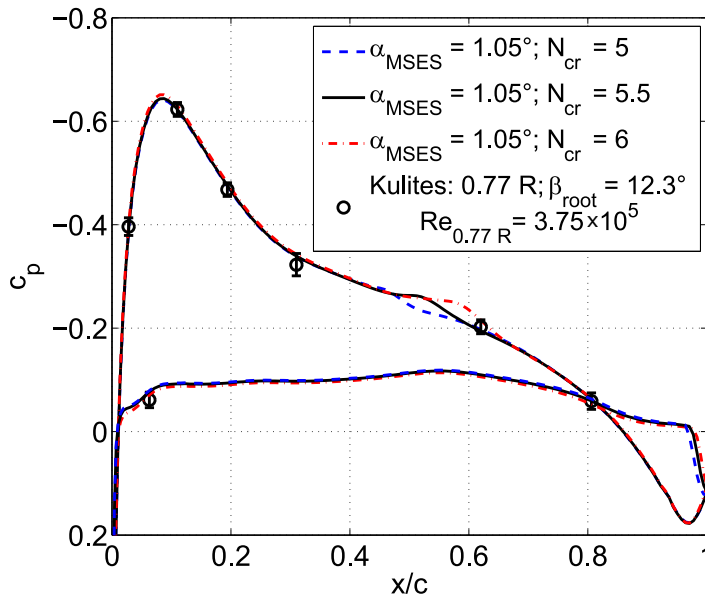
Figure 3.26: Comparison of measured surface pressures at $r/R = 0.77$ and $\beta_{root} = 12.3°$ to MSES results at $\alpha_{MSES} = 1.05°$ and at $\left(Re_{0.77R} = 3.75 \times 10^5; M_{0.77R} = 0.22\right)$ for different critical N-factors.

The corresponding chordwise temperature distribution obtained by TSP and the calculated friction coefficients c_f (see Eq. 1.13) corresponding to the three chosen values of N_{cr} are displayed in

Fig. 3.27a and Fig. 3.27b, respectively. Note the expected opposing trends between skin friction and surface temperature. High values of c_f close to the leading edge cause low surface temperatures due to more efficient cooling as compared to regions where c_f is low. One can also distinguish a slight change in the gradient of the rising temperature at $x/c \approx 0.2$ which corresponds to the beginning of a relatively low c_f-plateau. The opposing trends continue in the transition region where the drop in temperature coincides with the rise in c_f. The corresponding trends follow the Reynolds analogy and have similarly been observed by Richter et al. [121] on model and full scale helicopter blades in hover using IR for transition measurements. It should be noted that in MSES only the transition onset is provided. However, the resulting c_f distribution allows to define a transition point, $(x/c)_{tr,MSES}$, at the location of the maximum gradient (in analogy to the TSP data analysis, see Fig. 3.8) and also the end of transition which is often associated with the local c_f-maximum [2]. For the case presented it is found that the numeric solution obtained for $N_{cr} = 5.5$ matches the corresponding experimental results best. The finding is illustrated by the associated lines marking the transition regime for $N_{cr} = 5.5$ in Fig. 3.27b.
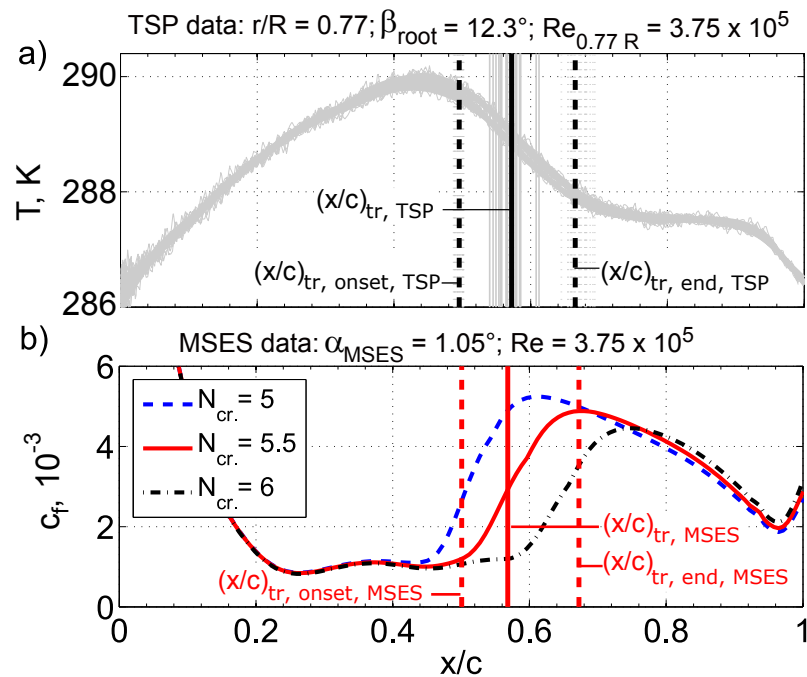
Figure 3.27: Comparison of *a)* TSP data and detected boundary-layer transition regime to *b)* c_f distributions obtained with MSES for the cases presented in Fig. 3.26.

To enable a comparison between numerical and experimental data for the whole data base presented, a data assimilation procedure was established as sketched in Fig. 3.28. Computations were performed at the conditions corresponding to the three tested Mach/ Reynolds number combinations at $r/R = 0.77$ (see Tab. 3.1). For each condition polars were calculated with various prescribed transition N-factors $N_{cr,i}$ as well as for a fully turbulent boundary-layer. In this context a polar corresponds to computations at angles of attack between $-2° \leq \alpha \leq 6°$ at increments of $\Delta\alpha = 0.05°$ and at a constant value for N_{cr}. The angles of attack α_{best} and the transition N-factor $N_{cr,best}$, yielding
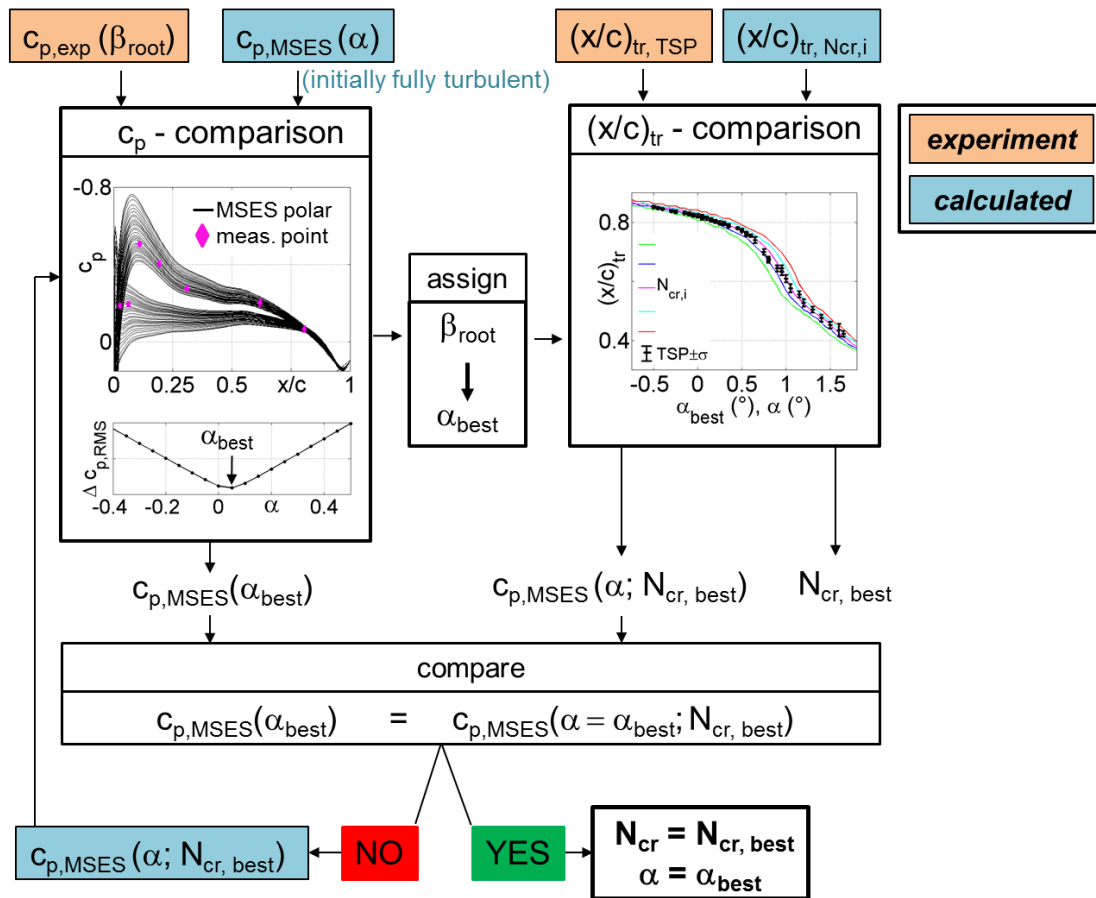
Figure 3.28: Data assimilation scheme for data points at conditions listed in Table 3.1

the surface pressure distributions and the transition positions, which best fit to corresponding experimental data, are found iteratively. For each experimental data point the measured surface pressures, $c_{p,\mathrm{exp}}$, are compared to numerical values of all pressure distributions, $c_{p,\mathrm{MSES}}$, from a computed polar. Initially, the fully turbulent polar is taken for comparison, since N_{cr} is unknown. The value for α_{best} is found by searching for that numerical c_p-distribution out of the polar which yields the minimum root-mean-square (RMS) value of the differences between measured and calculated c_p-values at the associated chordwise positions $\left(\Delta c_{p,\mathrm{RMS}} \rightarrow \mathrm{min.}\right)$. The RMS delta of the differences is calculated according to Eq. 3.8.

$$\Delta c_{p,\mathrm{RMS}} = \sqrt{\frac{1}{n_{\mathrm{sensors}}} \sum_{i=1}^{n_{\mathrm{sensors}}} \left(c_{p,\mathrm{exp},(x/c)_i} - c_{p,\mathrm{MSES},(x/c)_i}\right)^2} \tag{3.8}$$

The calculation is performed using available pressure data at six chordwise positions on the suction side, at $x/c = 0.028, 0.110, 0.194, 0.310, 0.620, 0.806$, and at one position on the pressure side, $x/c = 0.063$. The resulting value for $\Delta c_{p,\mathrm{RMS}}$ can be regarded as the effective difference between numerical and experimental surface pressures. Once every measurement point has been assigned to a best fitting numeric angle of attack $(\alpha_{\mathrm{best}} \leftrightarrow \beta_{\mathrm{root}})$ the experimentally measured transition positions can be plotted against α_{best}, $(x/c)_{\mathrm{tr,\,TSP}}$ vs. α_{best}, and compared to the calculated transition polars, $(x/c)_{\mathrm{tr},N_{\mathrm{cr,i}}}$ vs. α, obtained from different $N_{\mathrm{cr,i}}$. This way, a best matching critical N-factor, $N_{\mathrm{cr,best}}$, is found. However, the pressure distribution $c_p\left(\alpha_{\mathrm{best}}\right)$ depends on the value for N_{cr}, which is used in the c_p-comparison, and especially differs in the fully turbulent case. Therefore, it has to be ensured that the best fitting pressure distribution obtained from the c_p-comparison, $c_{p,\mathrm{MSES}}\left(\alpha_{\mathrm{best}}\right)$, is the same as the pressure distribution of the best matching transition polar at that angle of attack, which is $c_{p,\mathrm{MSES}}\left(\alpha = \alpha_{\mathrm{best}}; N_{\mathrm{cr,best}}\right)$. If this is not the case, the c_p-comparison is repeated with the calculated polar obtained using the current $N_{\mathrm{cr,best}}$. In fact, after two to three iterations the loop converged for the polars at all of the conditions tested. This means that the pressure distributions used to obtain α_{best} are obtained at that value of N_{cr} which also delivers the best fit of numerically obtained transition positions to experimental data.

The data assimilation results for all data points are presented in Fig. 3.29a-d. The angles of attack α_{MSES} corresponding to the best fitting pressure distributions are plotted in Fig. 3.29a against the corresponding experimentally adjusted root pitch angle β_{root}. A linear dependency can be deduced for all test conditions as expected. Whereas the lines for the two higher Reynolds numbers nearly coincide, a small offset towards higher α is distinguishable for the lowest $Re_{0.77R}$. Because α can be regarded as the effective angle of attack at $r/R = 0.77$, one can conclude that the induced velocity by the rotor at $Re_{0.77R} = 3.74 \times 10^5$ is slightly lower than in the other two cases. The exact reason for this observation remains unclear, especially since the relative blade loading is very similar and does not differ in the same manner (see Fig. 3.2), meaning that it is not comparatively lower at $Re_{0.77R} = 3.74 \times 10^5$.

In Fig. 3.29b the effective differences between numerical and experimental surface pressures $\Delta c_{p,\mathrm{RMS}}$ (see Eq. 3.8) are plotted for the validated cases. The assimilated pressure distributions exhibit RMS deltas of generally less than 0.02 with increasing deviations at higher $Re_{0.77R}$. Comparatively high $\Delta c_{p,\mathrm{RMS}}$ values can be deduced for high values of β_{root} at $Re_{0.77R} = 5.65$ and
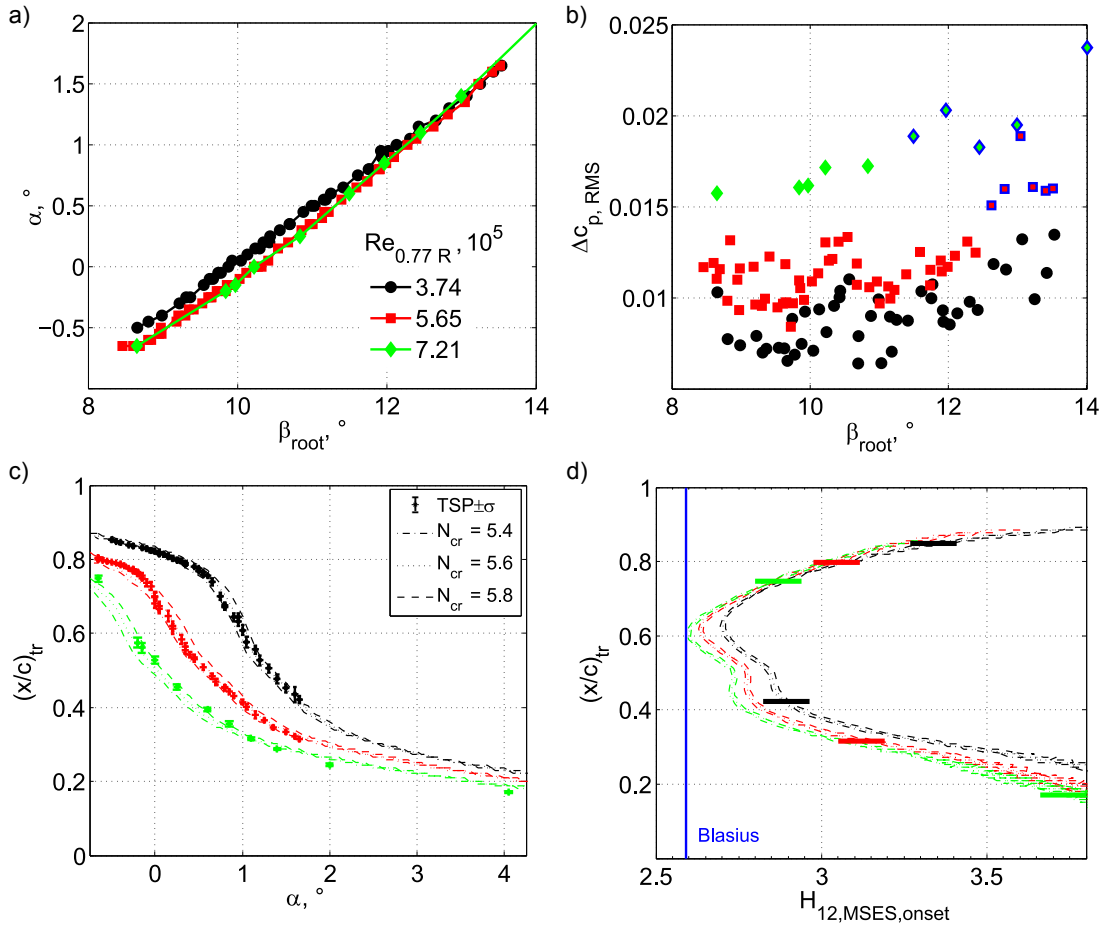
Figure 3.29: Data assimilation results obtained from MSES computations. Color coding is the same in all graphs.

a) Angle of attack α corresponding to best fitting c_p-distribution against root collective pitch β_{root}

b) Effective difference between numerical and experimental surface pressures $\Delta c_{p,RMS}$ vs. root collective pitch. Data points with comparatively bad fits within a series are highlighted in blue

c) Measured and simulated transition positions $(x/c)_{tr}$ at $N_{cr} = 5.4, 5.6$ and 5.8 against angle of attack α

d) $(x/c)_{tr}$ against shape factor at corresponding transition onset location $H_{12,MSES,onset}$ for calculated polars presented in $c)$. The chordwise range where transition is experimentally detected is confined by color coded horizontal bars, respectively.

7.21×10^5. The corresponding data points are marked in blue. It is assumed that the poor fit quality is due to a reduced ability of MSES to compute these data points accurately. As they are high thrust points, it is probable that the Euler-/boundary-layer code is less accurate for points where a non-linear boundary-layer thickening prior to stall is present. Other than that the assimilation procedure worked similarly accurate for all other data points at same $Re_{0.77R}$.

The measured transition positions are compared to simulations at $N_{cr} = 5.4, 5.6$ and 5.8 and plotted against angle of attack in Fig. 3.29c. Nearly all measured data points are within the calculated band spanned by the polars obtained when using the transition N-factor range of $N_{cr} = 5.6 \pm 0.2$. In other words, MSES simulations at $N_{cr} = 5.6$ predict the measured boundary-layer transition positions to an accuracy of better than $\Delta(x/c)_{tr} = \pm 0.04$. The overall best matching transition N-factor of 5.6 deviates slightly from the suggestion of $N_{cr} = 6$ by Lang et al. [77]. They conducted transition measurements in the same test facility but on a different rotor equipped with a modified NACA0015 airfoil and N_{cr} was also obtained by comparison to MSES computations. In their study transition was triggered by a laminar separation bubble where the streamwise N-factor gradient is especially large and thus compromises the calibration capability for N_{cr} [103]. In this study an indication on the transition mechanism can only be deduced from the assimilated MSES solutions which show overall positive values for c_f at almost all data points indicating natural Tollmien-Schlichting (TS) transition and no occurrence of a laminar separation bubble. The only exception to this is the data point acquired at $Re_{0.77R} = 7.21 \times 10^5$ at $\beta_{root} = 17°$ corresponding to $\alpha = 4°$, where MSES predicts a laminar separation bubble.

In order to characterize the boundary-layer state of the cases where transition to turbulence is measured, the shape factor $H_{12,MSES,onset}$ (see Eq. 1.11) is extracted at the position of the corresponding simulated transition onset. The onset position, as immediately provided by MSES, is considered for this purpose because it characterizes the laminar boundary-layer which is about to become turbulent. When plotted against the transition position, defined by the strongest gradient in c_f (see Fig. 3.29d), the range of shape factors can be identified in which transition was measured for each $Re_{0.77\,R}$. This is done by comparing the graph to Fig. 3.29c and confining the chordwise ranges, in which experimental data is available by bold horizontal lines as depicted in Fig. 3.29d, respectively. For comparison, the shape factor of a Blasius boundary-layer is added to the graph. All extracted shape factors correspond to decelerated boundary-layers $\left(H_{12,MSES,onset} > 2.6\right)$ with especially strong adverse pressure gradients $\left(H_{12,MSES,onset} > 3\right)$ where transition was detected upstream of $(x/c)_{tr} = 0.4$ and downstream of $(x/c)_{tr} = 0.75$. There is a link between the shape factor distribution in Fig. 3.29d and the change of the transition position with changing angle of attack (i.e. $\delta(x/c)_{tr}/\delta\alpha$) in Fig. 3.29c. Relatively high values of the shape factor at the measured transition onset position mean that transition occurred in a chordwise region where the adverse pressure gradient is comparatively large. It is known that the change in transition position relative to the change of the pressure gradient on an airfoil, which corresponds to $\delta(x/c)_{tr}/\delta\alpha$, is smaller in regimes where adverse pressure gradients are high, as compared to areas with more moderate adverse pressure gradients or in accelerated flow regimes [47, 161]. This is confirmed by the slope of the transition positions in Fig. 3.29c, which is comparatively small in chordwise regions where the shape parameter is high and vice versa.

3.4.2   Linear stability analysis

Based on the best fitting pressure distribution at known Mach and Reynolds number from MSES and assuming both adiabatic and non-adiabatic wall surface temperatures (see Sec. 3.3.5), the boundary-layer solver COCO [133] is used to compute velocity and temperature profiles. These solutions serve as input for the linear stability equations solver LILO [134].

The *original e^N* **- method employing COCO and LILO**   In COCO the boundary-layer equations are formulated in cylindrical coordinates for compressible flow around a conical swept wing (see [133]). In this work the boundary layer is investigated assuming 2D and compressible flow. The corresponding governing equations in COCO result as the limit for an infinitely swept wing which in turn are a specialization of the conical wing equations with zero sweep angle. When expressed in cartesian coordinates with x and y denoting the streamwise and wall normal directions, the governing equations reduce to the 2D compressible boundary-layer equations as defined in Eq. 1.3-1.6. Computations are performed based on the adiabatic and non-adiabatic wall temperatures as obtained according to the description in Sec. 3.3.5. Velocity profiles and, for non-adiabatic flows, also temperature profiles are calculated using a system of differential equations with an approach as detailed in [133].

Amplification rates are calculated using the stability analysis tool LILO. This is done according to 2D local LST assuming parallel flow as described in Sec. 1.2.1. The differential equations for the disturbances are formulated for compressible flow as derived by Schrauf [130–132]. The code is processed using the disturbance approach in Eq. 1.15 according to spatial theory for real values of Tollmien-Schlichting frequencies and also allowing waves in chordwise direction only. The effect of compressibility on calculated stability characteristics can be suppressed by setting the Mach number in the stability equations to zero, whereby the disturbance relations reduce to the Orr-Sommerfeld equation. Recall from Sec. 1.2.1 that this is the underlying relation for stability analysis inherent to the above mentioned approximate e^N-method. For better comparability, the stability analysis tool LILO is used to perform both compressible and incompressible stability analysis. Integral disturbance growth rates are obtained using the implemented and fully automated "prescribed frequency/ prescribed propagation direction integration strategy" [134]. In this context the propagation direction is forced in streamwise direction and growth rates are computed for in total 40 different frequencies. The relevant band comprising the amplified spectrum was predetermined using an implemented frequency estimator. The growth rates are integrated for each frequency along the streamwise coordinate and the maximum logarithmic amplification ratios are obtained according to the procedure outlined in Sec. 1.2.1 and sketched in Fig. 1.8. LILO is also capable of accounting for non-adiabatic surface temperature effects on the stability characteristics by considering the temperature profiles as calculated in COCO for the non-adiabatic condition.

Stability analysis is performed employing both the compressible and incompressible set of stability equations as well as assuming adiabatic and non-adiabatic wall temperatures (see section 3.3.5), respectively. Unless otherwise stated, the presented results correspond to compressible calculations under non-adiabatic wall temperature conditions.

Results Integral growth rates are plotted as N-factor in Fig. 3.30a and Fig. 3.30b along with the corresponding pressure distributions against the chordwise coordinate for several unstable TS frequencies at sample data points corresponding to $Re_{0.77\,R} = 3.73 \times 10^5$ and 7.22×10^5, respectively. As expected from linear stability theory higher frequencies are amplified further upstream, reach a maximum and begin to be damped while lower frequencies continue to be amplified. The red curve denotes the envelope, which combines the integral growth rates of the most amplified frequency at each chordwise position. The transition N-factor is found by extracting the value of the envelope curve at the chordwise position of the measured transition onset (see Fig. 3.8). A corresponding behaviour between the chordwise slope of the N-factor, i.e. the local disturbance growth rates, and the pressure gradient can be distinguished. As expected from boundary-layer theory [129, 152] and known from experimental validation [83, 136], higher adverse pressure gradients cause increased amplification of disturbances. Moreover, and also in accordance with theory, the amplified frequencies are higher for the larger Reynolds number in Fig. 3.30b as compared to the amplified frequencies in the lower Reynolds number case, plotted in Fig. 3.30a.

Transition N-factors could not be found for all data points. The correlation failed for those cases (not shown), where the measured transition onset lies downstream of the last chordwise position where N-factors are calculated in LILO. Note in Fig. 3.30 that the N-factor curves stop either downstream of their maximum in a region where the corresponding frequency is already damped or in the vicinity of the chordwise position where the kink is distinguishable in the corresponding pressure distribution. In the former case the stability analysis tool LILO automatically stopped to calculate growth rates of already damped TS frequencies as they are not expected to be amplified again. In the latter case the boundary-layer equation solver COCO could not find a boundary-layer solution which could be used in LILO to perform stability analysis. This is because COCO indicates laminar separation which is triggered by the visible pressure increase, i.e. the kink. Recall that the pressure distribution, which is used as boundary condition in the boundary-layer solver COCO, results from the best fitting MSES solution including transition prediction (at $N_{\mathrm{cr,MSES}} = 5.6$). As the MSES solution switches from a laminar to a turbulent boundary-layer the resulting pressure distribution experiences a pressure increase, denoted as kink, which is due to the thickening of the boundary layer [114]. Hence, only the pressure distribution upstream of the kink corresponds to a laminar boundary-layer. Practically only this part is a valid boundary-condition for the laminar boundary-layer solution obtained by COCO. So, if critical N-factors cannot be correlated in LILO, it actually means that the measured position of transition onset (used for the correlation) is downstream of the calculated transition onset in MSES, which eventually causes the kink in the pressure distribution and in turn COCO to indicate alleged laminar separation. However, due to the following reasoning it would be misleading to conclude that transition was triggered by laminar separation bubbles in the cases where the correlation failed. For reasons of robust detectability, the measured transition onset $(x/c)_{\mathrm{tr,onset}}$ is defined in the vicinity of the maximum curvature of the TSP result (see Fig. 3.8). However, according to the studies by Schubauer and Klebanoff [135] as well as the work of Owen [107], the actual onset of turbulent intermittency, as measurable by hot-film sensors, occurs slightly further upstream as compared to the position where a deviation from laminar flow behaviour is detectable by thermographic methods as TSP. Therefore, the flow cannot
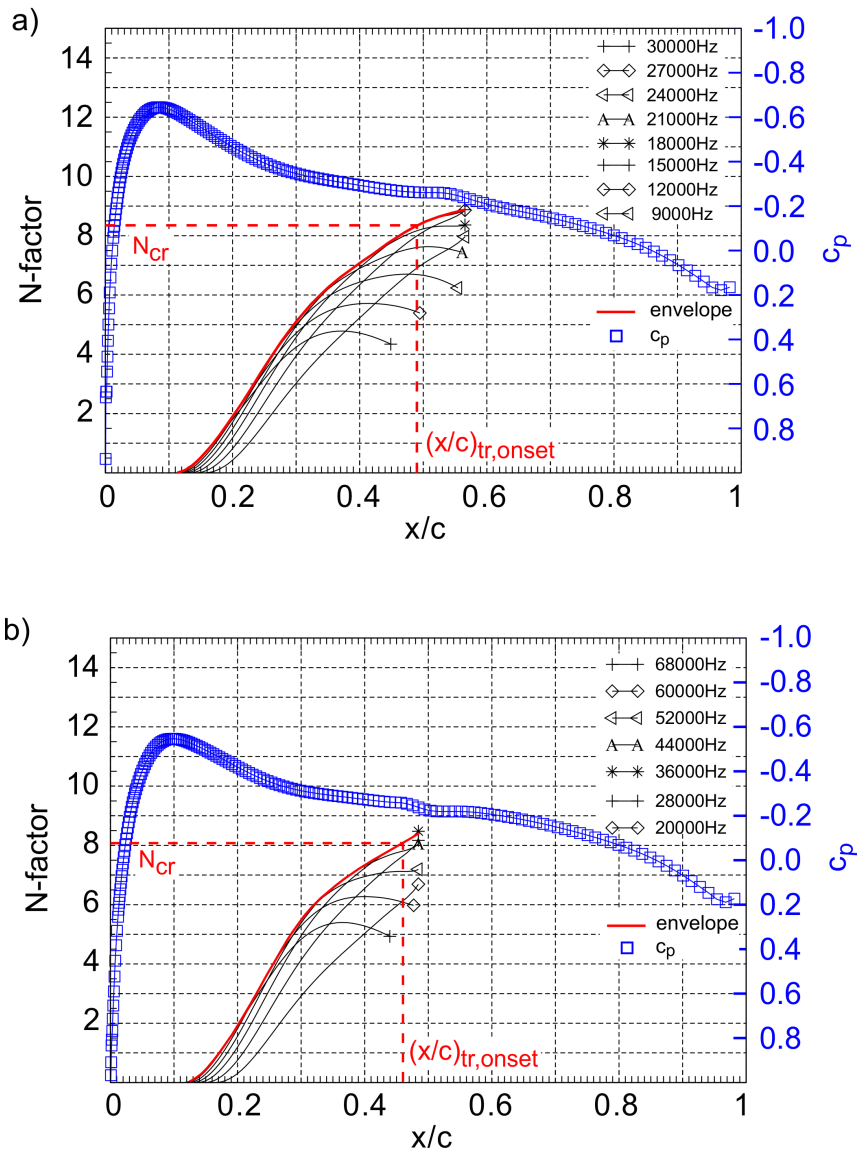
Figure 3.30: Natural logarithm of integral growth rates as N-factor for several amplified TS-frequencies and corresponding pressure distribution against chordwise coordinate at $Re_{0.77\,R} = 3.73 \times 10^5$; $\beta_{root} = 12.3°$ in a) and at $Re_{0.77\,R} = 7.22 \times 10^5$; $\beta_{root} = 10.2°$ in b). Transition N-factors N_{cr} are correlated at the experimentally deduced transition onset $(x/c)_{tr,onset}$.

be assumed to be fully laminar anymore at $(x/c)_{\text{tr,onset}}$, which is why the available information does not allow to deduce the existence of a laminar separation bubble although COCO denotes laminar separated flow at this position.

All correlated transition N-factors are plotted against the collective pitch angle in Fig. 3.31a and against the incompressible shape factor as calculated with COCO at the measured transition onset in Fig. 3.31b. The obtained range of shape factors at transition onset agrees with those computed by MSES (see Fig. 3.29d). Further analysis of the transition N-factors shows that most data correlate at $N_{\text{cr}} = 8.4 \pm 0.5$ not showing any dependence on Reynolds number. Note the few exceptions marked in blue. They correspond to the cases mentioned above in Fig. 3.29b and should be neglected as the corresponding best matching numerical c_p-distributions exhibit large differences when compared to the other cases of the series at similar Reynolds number. In view of the N-factor envelopes shown in Fig. 3.30 an uncertainty of $\Delta N_{\text{cr}} = \pm 0.5$ translates to an uncertainty in a predicted transition onset of $\Delta (x/c)_{\text{tr,onset}} \approx \pm 0.05$. This estimation corresponds to the worst case where the slope of N with respect to x/c is the flattest.

An estimate of the absolute wall-heating effect can be derived by comparing the data corresponding to non-adiabatic wall temperatures (filled circles) to the data obtained assuming adiabatic wall temperatures (open circles). The effect is shown for the lowest Reynolds number, where it is the strongest as the corresponding level of non-adiabatic wall temperature is the highest (see Fig. 3.24). The transition N−factors correlate systematically at higher N_{cr} if non-adiabatic conditions are presumed with differences in the range of $\Delta N_{\text{cr}} = 0.2 - 0.4$. This is expected and can be attributed to the increased amplification of Tollmien-Schlichting waves on heated surfaces in air [129]. Note also that the deviations in terms of ΔN_{cr} are higher at lower collective pitch angles where transition occurs further downstream when compared to higher collective pitch settings. This is plausible since the laminar boundary-layer is heated up over a larger streamwise distance at low β_{root}. In contrast, no detectable trend in N_{cr} can be observed with respect to variations of the shape factor at transition onset.

For the sake of completeness it should be mentioned that correlations for N_{cr} based on incompressible LST (not shown) are independent of both Reynolds number and collective pitch angle, similarly as the compressible values for N_{cr}. According to Arnal [4] higher maximum integral growth rates are expected for incompressible correlations than if compressibility was considered. This is because of the damping effect of compressibility on the amplification of TS waves in transitional boundary-layers. This hypothesis could be confirmed in the present study and the mean of the incompressible transition N-factors was observed to be larger than the compressible value by approximately $\Delta N_{\text{cr}} \approx +0.5$. Although the effect of compressibility is comparatively larger at higher rotating speeds all correlated incompressible transition N-factors are within a band of similar scatter ($\Delta N_{\text{cr}} \approx \pm 0.5$) when compared to the compressible values.

3.4.3 Comparison and discussion of correlated transition N-factors

For a better overview the transition N-factors found in this study and the assumptions inherent to the employed methods are summarized in Tab. 3.3.
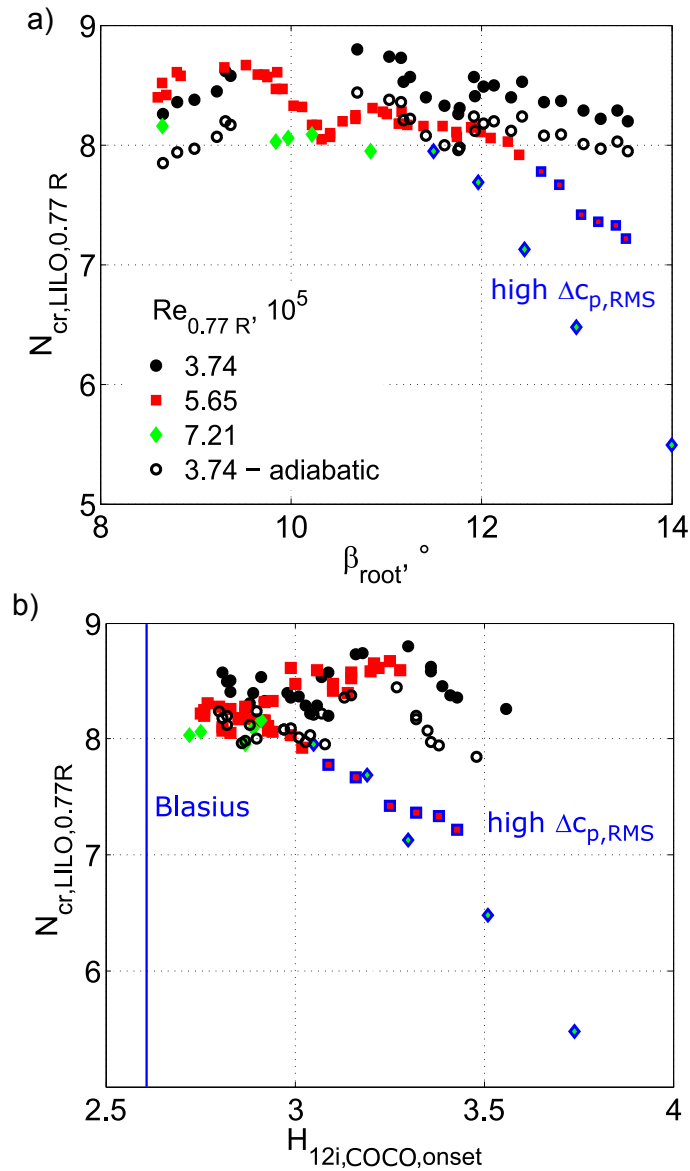
Figure 3.31: Transition *N*-factors obtained from 2D compressible local linear stability theory against collective pitch in a) and against incompressible shape factor from COCO at measured transition onset position in b). Full symbols denote results of boundary-layer computations employing the measured non-adiabatic wall temperatures as boundary condition. Data points in blue correspond to cases with comparatively bad matching numerical and experimental pressure distributions (compare to Fig. 3.29b)

Table 3.3: Comparison of critical N-factors and inherent assumptions of the methods used

	approximate e^N-method	*original e^N*-method
laminar boundary-layer solution	from MSES (see [26]): • 2D compressible • integral solution based on Falkner-Skan profiles • adiabatic	from COCO (see [133]): • 2D compressible • differential solution for velocity and temperature profiles • adiabatic vs. non-adiabatic
stability characteristics	from MSES (see [26]): • Orr-Sommerfeld solutions of locally prescribed Falkner-Skan profiles (data base) • 2D parallel local LST, waves in chordwise direction only • incompressible • adiabatic	from LILO (see [134]): • growth rate calculation of boundary-layer profiles along streamwise direction • 2D parallel local LST, waves in chordwise direction only • compressible vs. incompressible • non-adiabatic vs. adiabatic
growth rate integration/ -correlation	• linear approx. of envelopes for Falkner Skan profiles $\rightarrow$ max. integral N-factor **is independent of** f_{TS}	• as originally proposed in [60, 143] $\rightarrow$ max. integral N-factor **depends on** f_{TS}
critical N-factor	• $N_{cr,MSES} = 5.6 \pm 0.2$	• $N_{cr,LILO} = 8.4 \pm 0.5$ (compressible, non-adiabatic) • Δ adiabatic ≈ -0.2 to -0.4 • Δ incompressible $\approx +0.5$
prediction accuracy	• $\Delta N_{cr,MSES} = \pm 0.2$ $\rightarrow \Delta(x/c)_{tr} = $ max. ± 0.04	• $\Delta N_{cr,LILO} = \pm 0.5$ $\rightarrow \Delta(x/c)_{tr} = $ max. ± 0.05

Note that the values for N_{cr}, which are calculated with LILO, are significantly higher than the best value found with MSES. Recall that the measured transition positions are always downstream of the suction peak and that the shape factors at the detected transition onset denote decelerated flow in all cases (see Fig. 3.29d and Fig. 3.31b). Moreover, the boundary-layer flow on the convex-shaped DSA-9A airfoil is not self-similar. Instead, it can be inferred for all data points that in total the shape factor has increased downstream of the indifference point, which is in the vicinity of the

suction peak at $x/c \approx 0.12$ (see Fig. 3.26), up to the locations where transition was measured (see Fig. 3.14). Because the approximate e^N-method underestimates the critical N-factor in such cases, the lower value for $N_{cr,MSES}$ is plausible. Moreover, in view of the above stated shortcomings of the approximate e^N-method (see Sec. 3.4.1 or [20]), one should be aware that an additional uncertainty in $N_{cr,MSES}$ is introduced when considering the applicability of $N_{cr,MSES} = 5.6$ for transition prediction on other airfoils than the DSA-9A airfoil.

Strictly speaking, all denoted critical N-factors hold true within the limits of the stated assumptions. The assumptions expressing the actual measurement conditions with the least simplifications are resembled by $N_{cr,LILO} = 8.4 \pm 0.5$ which is based on compressible linear stability theory under consideration of the present non-adiabatic wall temperature conditions. Moreover, all denoted critical N-factors pose limiting amplification ratios of disturbances until transition to turbulence is expected. Therefore, the values have to be considered in view of the corresponding test conditions in the RTG (see Sec. 3.1), since for instance the initial disturbance amplitude spectrum and the underlying receptivity mechanisms (influence of model vibrations, noise etc.) are unknown.

The independence from the correlated transition N-factors of Reynolds number, i.e. the rotating speed, is not necessarily expected. Assuming that the disturbance velocity field of the flow hitting the blade surface was not altered significantly as the rotation speed is increased, the resulting turbulence intensity with respect to the speed of the blade would decrease at higher rotation rates. According to Mack's findings [92] the transition N-factors would then be expected to increase with the blade relative Reynolds numbers. Instead, the results suggest that as the rotation speed is increased, both the incoming turbulence and the receptivity process are altered such that the correlated N-factors remain roughly constant. A possible reason for the observed behavior might originate from increased blade vibrations at higher rotation rates, eventually causing higher velocity fluctuations which are coupled into the boundary-layer and which lead to increased initial disturbance amplitudes. In this respect more detailed investigations of both the actual velocity disturbances close to the rotating blade surface and in proximity to the rotor disc would be useful. Though challenging to obtain, it would foster the understanding of the underlying mechanisms. However, presuming that 2D LST holds true for the investigated configurations, the transition N-factor can be utilized to estimate a relative turbulence intensity at $0.77R$ using Mack's relation [92] according to Eq. 1.19.

$$Tu_{0.77\,R} = e^{(8.43 + N_{cr,LILO})/-2.4} \tag{3.9}$$

With $N_{cr} = 8.4 \pm 0.5$ the turbulence intensity turns out to be $Tu_{0.77\,R} = 0.09 \pm 0.02\,\%$.

4 Concluding remarks

4.1 Summary and conclusion

In this thesis air loads and boundary-layer transition are investigated on a Mach-scaled helicopter rotor blade configuration in climb. Spatially highly resolved surface pressures and boundary-layer transition regions were measured on the suction side of the outer $60\,\%$ of the rotor blades, equipped with a DSA-9A airfoil, by means of advanced optical measurement techniques. An optimized pressure-sensitive paint (PSP) measurement system was applied for surface pressure measurements and boundary-layer transition was measured mainly by means of temperature-sensitive paint (TSP) and for comparison also via infrared (IR) thermography. The experiments were conducted in the rotor test facility of the DLR Göttingen (RTG) and were complemented by pressure tap measurements on blade sections at two different radii as well as by integral thrust measurements. The investigated parameter range comprises extensive variations of the collective root pitch angle at three different rotating speeds spanning tip chord Reynolds and Mach numbers of $Re_{\mathrm{tip}} = 4.6 - 9.3 \times 10^{5}$ and $M_{\mathrm{tip}} = 0.29 - 0.57$, respectively. Measured boundary-layer transition data are specifically evaluated with respect to an influence of rotating forces and experimental results at selected radial sections are compared to two-dimensional (2D) numerical simulations, using a coupled Euler/ boundary-layer solver. Finally, the transition prediction capabilities of 2D local linear stability theory (LST) methods are assessed by correlating transition N-factors with measured boundary-layer transition data.

The major outcomes are summarized as follows:

1. The optimized PSP measurement system for global surface pressure measurements on fast rotating blades is presented. The system characteristics are assessed and the technique is demonstrated to solve the problem of image blur when applied to fast rotating blades. An optimized image acquisition technique, directly implemented in the camera employed, allows omitting error-prone post-processing routines or laborious setups to eliminate artifacts originating from rotational blur. Moreover, the employed single-shot lifetime technique additionally enables the capture of instationary flow phenomena such as stalled flow regimes.

2. The PSP system was successfully applied to the helicopter blade configuration. The measured surface pressure distributions yield plausible trends at varying rotation rates and collective pitch angles and the results reveal flow features such as the footprint of the tip-vortex and the suction peak parallel to the leading edge. A best-practice comparison between ensemble-averaged PSP data and fast-response pressure tap readings on the same blade reveals a RMS level of residual deltas of $\sim 250\,\mathrm{Pa}$. Surface pressures computed by the 2D coupled Euler/ boundary-layer code MSES are compared to the results measured by PSP at an example tangential blade section and agree within $\Delta c_p \sim 0.1$, supporting the plausibility of the experimental findings.

3. Partially stalled flow is detected by means of fast response pressure transducers and integral thrust measurements for a particular data point. The application of the single-shot

PSP lifetime technique additionally allowed the identification of stall-related flow regions comprising relatively increased low-frequent pressure fluctuations.

4. Sample PSP results reveal a chordwise pressure discontinuity just downstream of the suction peak. Detailed analysis and comparison to results of the separately conducted TSP boundary-layer transition experiment show the correlation between the observed kink in the PSP results and the abrupt pressure increase indicative for laminar-turbulent transition on the airfoil investigated. To the author's knowledge this is the first published work where boundary-layer transition could be distinguished in PSP data on fast rotating blades emphasizing the capability of the optimized measurement technique to capture spatial pressure gradients in a precise manner.

5. The boundary-layer transition results obtained by TSP and IR are comparable in those regions of the blade surface where free transition is observed. IR results were obtained on the blade equipped with pressure sensors and revealed turbulent wedges emanating downstream of the wall tappings. TSP results turned out to be beneficial for further processing due to the homogeneously polished surface. In contrast a visible effect of boundary-layer receptivity to surface roughness appears in the IR results of a partly worn out and uncoated blade surface.

6. An algorithm is presented, capable of detecting the transition position as well as onset and end of the transition zone. It is applied for all data points and at various radial positions across the blade. The quality of the results allows the detection of the transition position with a precision of better than 1 % chord (i.e. $\approx 0.7\,\text{mm}$) at varying collective pitch. Together with corresponding pressure tap data at two radial blade sections and the associated integral thrust measurements, post-processed transition data has been collected to establish a data base ready to use for validation purposes of advanced three-dimensional flow solvers of rotor flows including transition prediction capabilities.

7. Analyses of the boundary-layer transition measurements show expected trends of the transition position moving upstream at both higher collective pitch and increasing tip chord Reynolds number. Detailed analyses reveal a correlation between the change in chordwise transition location with collective pitch and the pressure distribution on the investigated DSA-9A airfoil. An effect of the tip vortex on boundary layer transition was identified as a function of both blade loading coefficient and tip chord Reynolds number.

8. Boundary-layer transition data are specifically analyzed with respect to the influence of rotating forces at $Re = 3.74 \times 10^5$ and $M = 0.22$ by variation of Rossby number Ro between the two values $Ro = 6.95$ and $Ro = 4.76$. The lower number denotes a relatively higher contribution of centrifugal and centripetal accelerations to the quasi-steady equilibrium of the investigated flow. The variation of Ro in this study reveals no measurable effect of rotating forces on the detected transition positions. Bias effects due to non-similar chord Reynolds numbers and relatively different non-adiabatic blade surface temperatures could be excluded when comparing data at the stated Rossby numbers. It is therefore concluded that a stabilizing effect of rotational forces on boundary-layer transition is insignificant on the DSA-9A airfoil suction side and within the stated parameter range.

9. The experimental data obtained at 77 % radius is compared to solutions of a coupled two-dimensional (2D) Euler- / boundary-layer solver and used to obtain transition N-factors based on different approaches to the e^N-method for transition prediction. For the N-factor analyses 2D local linear stability theory (LST) is employed allowing disturbance wave propagation in chordwise direction only. Numerical c_p-distributions are found which agree to surface pressure tab measurements within a difference of $\Delta c_p \approx 0.02$ when considering the RMS values of the differences. The critical N-factor which reflects the actual measurement conditions best is $N_{cr} = 8.4 \pm 0.5$. It is based on compressible LST and considers the measured non-adiabatic wall temperature conditions. The scatter of correlated N-factors translates to a prediction capability of the transition position of better than $\Delta(x/c)_{tr} \approx \pm 0.05$.

   Taking into account the insignificant effect of rotational forces on the measured transition positions and the good comparability to 2D computations employing 2D LST, it is concluded that boundary-layer transition can be reduced to a 2D problem for the investigated configuration, presuming that the pressure distribution or effective angle of attack is known. Since rotational effects are weaker at higher Re, a stabilizing effect of rotational forces on boundary-layer transition on the suction side of a DSA-9A rotor blade is not expected at higher Reynolds numbers either.

10. The obtained transition N-factors for data extracted at $r/R = 0.77$ correlate independently of the boundary-layer shape factor at the measured position of transition onset and especially independently of the chord Reynolds number, which is based on rotation speed. It is inferred that the relative turbulence intensity of the incoming flow at the respective radial position remains unchanged despite the change of rotation speed. Following Mack's relation between the transition N-factor and turbulence intensity and considering $N_{cr} = 8.4 \pm 0.5$, the corresponding turbulence intensity turns out to be $Tu_{0.77\,R} = 0.09 \pm 0.02$ %.

4.2 Outlook

The biggest challenge for future PSP measurements on fast rotating blades originates from the temperature sensitivity of the PSP employed. The reported difficulties with respect to the correction of temperature effects are believed to be tackled most efficiently by measuring the temperature of the PSP coated blade surface directly. This could be realized by infrared imaging, yet facing the challenges to capture sufficient signal and to avoid image blur. A different solution is the use of a dual-type sensor dye allowing to capture pressure- and temperature-sensitive signals in parallel. This could be realized by incorporating both the pressure and temperature sensor in the same coating (see [112]) or by separating the sensors physically on the model using a painted grid pattern with exclusively temperature-sensitive areas (see [111]). However, both methods need further development to be suitable for lifetime measurements on fast rotating blades.

In the presented investigation with respect to the effect of rotational forces on boundary-layer transition it is not distinguished between an effect on the boundary-layer flow itself (e.g. the magnitude of radial velocity components inside the boundary-layer due to rotation) and the influence of rotation on the resulting stability characteristics. A numerical study comprising a three-dimensional

flow solution of the problem and an additional stability analysis of the resulting boundary-layer profiles with optional consideration of the rotational terms would firstly allow the validation of the present finding and secondly to quantify and distinguish the present effect of rotational forces on the whole blade. For instance, the tool developed by Dechamps and Hein [18] allows this kind of stability analysis.

More experimental information on the boundary-layer flow could be obtained by applying the post-processing algorithm proposed by Liu and Woodiga [86] on the TSP data as it was done e.g. by Miozzi et al. [100] or by applying an equivalent method on the pressure gradient field acquired by PSP [87]. The techniques allow to detect the relative magnitude and direction of the corresponding wall skin friction and the detection of possible laminar separation. A different approach to this information is the oil-film interferometry method for rotating blades as proposed by Schülein [138].

The presented work shows a negligible effect of rotational forces on the suction side of the investigated Mach-scaled DSA-9A rotor blade at $Ro > 4.76$ and at $Re > 3.74 \times 10^5$, only. However, rotational effects on boundary-layer transition also depend on the apparent pressure gradients and they are more pronounced at moderate adverse or favorable pressure gradients [95]. The presented study on rotational effects should therefore be extended to the blade pressure side and to other airfoils and blade geometries of interest. In this context, also blade geometries which provoke radial flow, e.g. by geometric sweep angles, are of interest. This is because it is the radial velocity component which causes the stabilizing action of the Coriolis force with respect to boundary-layer transition. For these purposes, a parameter study analyzing boundary-layer stability under consideration of rotational forces would be helpful to confine a range in terms of Rossby number, Reynolds and Mach number as well as pressure gradient and flow angles under which rotational effects need to be considered for accurate prediction of boundary-layer transition on rotating blades.

In this study a single transition N-factor appears to predict reasonable transition positions at the investigated tangential section for all rotating speeds and collective pitch settings tested. Further studies should investigate how the critical N-factor behaves along the entire blade span. Moreover, a characterization of the incoming velocity and pressure fluctuations depending on blade radius and axial distance to the rotor plane would foster the understanding of boundary-layer receptivity on rotating blades. It would also allow to define the boundary-conditions necessary for reliable numerical predictions more precisely.

Appendix

A   Selected experimental data

In the following, test conditions and measurement results of example test cases are listed in order to serve as a data base for validation of advanced numerical codes. The summarized data are in principle discussed in Sec. 3.3 and chosen according to the following pattern:

- Cases 1-5 represent a variation of collective pitch at $f_{\text{rotor}} = 23.6\,\text{Hz}$. Similar cases are plotted in Fig. 3.17 and discussed in Sec. 3.3.3.

- Cases 2, 6 and 7 demonstrate a variation of Re_{tip} at a constant blade loading of $C_T/\sigma = 0.010$. The cases are plotted in Fig. 3.18 and discussed in Sec. 3.3.3.

- Cases 8 and 9 are an example for a "c_p-pair" as it is used for the investigation of an effect of rotational forces on boundary-layer transition. The cases are plotted in Fig. 3.22 and discussed in Sec. 3.3.4.

A.1 Test conditions

Table A.1: Test conditions and integral thrust data for nine test cases

Case	β_{root}, °	f_{rotor}, Hz	p_∞, hPa	T_∞, °C	ρ_∞, kg/m^3	Re_{tip}, 10^5	M_{tip}	v_∞, m/s	$F_{thrust} \pm \sigma_{F_{thrust}}$, N
1	8.7	23.6	998	8.9	1.230	4.81	0.286	2.0	1 ± 19
2	10.1	23.6	998	8.9	1.228	4.80	0.286	2.1	11 ± 20
3	11.0	23.6	998	8.9	1.230	4.82	0.286	2.0	17 ± 20
4	12.0	23.6	998	8.9	1.232	4.83	0.286	2.1	27 ± 20
5	13.1	23.6	999	8.9	1.236	4.85	0.287	2.1	37 ± 22
6	10.1	35.4	998	8.9	1.233	7.25	0.430	3.1	24 ± 37
7	10.0	47.2	987	12.7	1.198	9.29	0.568	4.1	43 ± 85
8	12.1	23.6	998	8.6	1.233	4.83	0.286	2.0	28 ± 21
9	10.2	35.4	987	12.7	1.198	6.97	0.426	3.1	27 ± 32

A.2 Surface pressure data

Table A.2: Surface pressures from *Kulite LQ-062* sensors in c_p (Eq. 2.5) for cases in Tab. A.1. *top*: mean *bottom*: standard deviation

r/R		0.53 ($r = 0.3425$ m)				0.77 ($r = 0.5$ m)					
side		lower	upper			lower			upper		
x/c		0.764	0.110	0.194	0.620	0.063	0.110	0.194	0.310	0.620	0.806
1		-0.0489	-0.5435	-0.4504	-0.2521	-0.3026	-0.4213	-0.3387	-0.2357	-0.1920	-0.0740
		0.0263	0.0265	0.0260	0.0449	0.0126	0.0125	0.0127	0.0116	0.0261	0.0825
2		-0.0417	-0.6426	-0.5171	-0.2648	-0.2104	-0.4936	-0.3879	-0.2661	-0.2005	-0.0647
		0.0269	0.0269	0.0258	0.0422	0.0128	0.0126	0.0127	0.0120	0.0302	0.0190
3		-0.0293	-0.6813	-0.5402	-0.2655	-0.1549	-0.5395	-0.4147	-0.2842	-0.1980	-0.0607
		0.0264	0.0271	0.0261	0.0350	0.0138	0.0133	0.0131	0.0131	0.0181	0.0165
4		-0.0327	-0.7518	-0.5881	-0.2708	-0.0842	-0.6040	-0.4573	-0.3142	-0.2059	-0.0636
		0.0272	0.0272	0.0266	0.0330	0.0148	0.0134	0.0131	0.0182	0.0138	0.0159
5		-0.0249	-0.7963	-0.6123	-0.2486	-0.0144	-0.6727	-0.4938	-0.3473	-0.2017	-0.0602
		0.0258	0.0274	0.0265	0.0326	0.0155	0.0140	0.0133	0.0362	0.0128	0.0156
6		-0.0567	-0.6065	-0.4766	-0.2022	-0.2389	-0.4990	-0.3817	-0.2749	-0.1824	-0.0461
		0.0124	0.0124	0.0115	0.0152	0.0056	0.0056	0.0057	0.0050	0.0115	0.0079
7		-0.0684	-0.5975	-0.4617	-0.1846	-0.2654	-0.5218	-0.3915	-0.2882	-0.1792	-0.0407
		0.0069	0.0074	0.0066	0.0082	0.0040	0.0041	0.0034	0.0028	0.0074	0.0046
8		-0.0305	-0.7513	-0.5913	-0.2638	-0.0746	-0.6098	-0.4620	-0.3180	-0.2039	-0.0607
		0.0272	0.0273	0.0261	0.0329	0.0147	0.0135	0.0132	0.0193	0.0137	0.0159
9		-0.0578	-0.6085	-0.4700	-0.2071	-0.2277	-0.5059	-0.3759	-0.2558	-0.1872	-0.0457
		0.0129	0.0128	0.0115	0.0145	0.0057	0.0057	0.0056	0.0049	0.0113	0.0080

A.3 Transition data
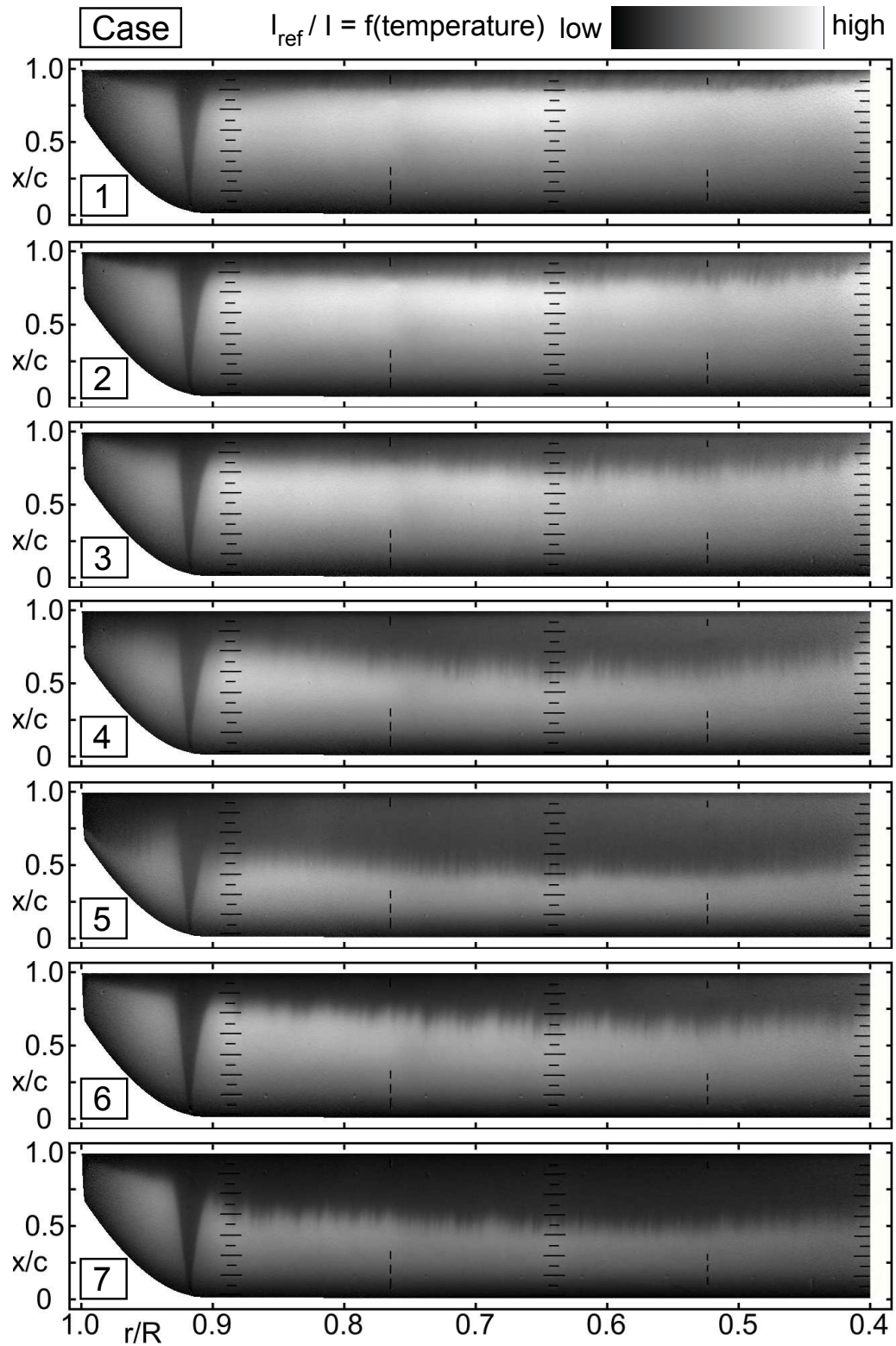
Figure A.1: TSP results for cases 1-7 in Tab A.1.
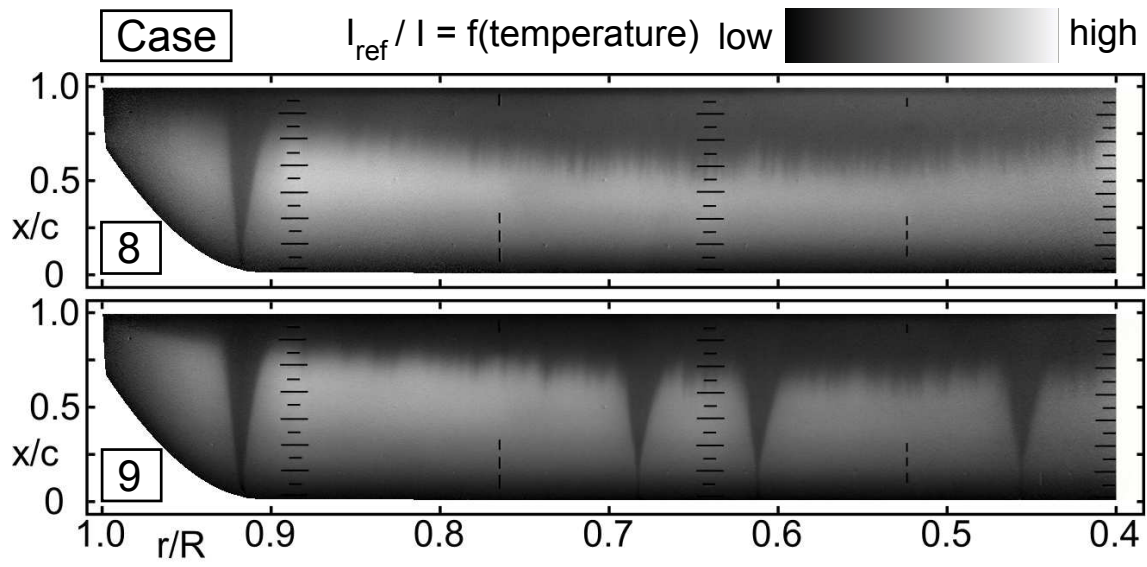
Figure A.2: TSP results for cases 8 and 9 in Tab A.1.

Table A.3: Measured transition onset positions $(x/c)_{\text{tr,onset}}$ for cases in Tab. A.1. *top:* mean value; *bottom:* standard deviation

r/R	0.42	0.48	0.53	0.57	0.63	0.66	0.72	0.77	0.82	0.88	0.94	0.97
r, m	0.270	0.310	0.343	0.370	0.410	0.430	0.470	0.500	0.530	0.570	0.610	0.630
1	0.857	0.820	0.810	0.813	0.804	0.802	0.802	0.785	0.782	0.728	0.766	0.826
	0.003	0.005	0.004	0.002	0.002	0.001	0.002	0.003	0.002	0.005	0.022	0.013
2	0.820	0.740	0.733	0.743	0.730	0.736	0.756	0.761	0.759	0.757	0.782	0.826
	0.011	0.009	0.008	0.006	0.005	0.004	0.003	0.002	0.002	0.002	0.016	0.009
3	0.763	0.673	0.658	0.659	0.650	0.656	0.677	0.705	0.701	0.705	0.728	0.773
	0.021	0.005	0.009	0.007	0.007	0.005	0.006	0.002	0.003	0.004	0.006	0.021
4	0.632	0.536	0.493	0.489	0.491	0.488	0.510	0.541	0.575	0.616	0.627	0.641
	0.037	0.013	0.011	0.008	0.010	0.012	0.014	0.005	0.004	0.004	0.014	0.017
5	0.438	0.389	0.370	0.375	0.376	0.378	0.378	0.404	0.438	0.442	0.530	0.399
	0.024	0.007	0.005	0.006	0.007	0.007	0.004	0.008	0.006	0.007	0.015	0.020
6	0.598	0.586	0.555	0.558	0.587	0.573	0.609	0.646	0.671	0.684	0.761	0.804
	0.023	0.009	0.006	0.011	0.007	0.023	0.011	0.011	0.006	0.010	0.022	0.006
7	0.462	0.447	0.422	0.414	0.431	0.431	0.456	0.493	0.502	0.508	0.724	0.771
	0.009	0.006	0.007	0.007	0.008	0.012	0.014	0.013	0.010	0.011	0.026	0.005
8	0.609	0.516	0.476	0.473	0.473	0.472	0.493	0.522	0.559	0.599	0.623	0.635
	0.043	0.011	0.011	0.008	0.009	0.010	0.015	0.005	0.006	0.005	0.011	0.025
9	0.592	0.581	0.549	0.564	0.560	0.577	0.613	0.650	0.674	0.684	0.750	0.791
	0.023	0.025	0.007	0.008	0.035	0.019	0.010	0.009	0.006	0.004	0.020	0.008

Table A.4: Measured transition positions $(x/c)_{tr}$ for cases in Tab. A.1. *top*: mean value; *bottom*: standard deviation

r/R	r, m	0.42	0.48	0.53	0.57	0.63	0.66	0.72	0.77	0.82	0.88	0.94	0.97
		0.270	0.310	0.343	0.370	0.410	0.430	0.470	0.500	0.530	0.570	0.610	0.630
1		0.879	0.865	0.857	0.861	0.857	0.854	0.861	0.854	0.856	0.820	0.861	0.878
		0.000	0.007	0.004	0.003	0.002	0.003	0.003	0.004	0.003	0.012	0.013	0.004
2		0.866	0.799	0.786	0.805	0.791	0.799	0.820	0.811	0.828	0.836	0.870	0.878
		0.010	0.009	0.012	0.006	0.002	0.003	0.003	0.007	0.003	0.003	0.008	0.002
3		0.830	0.744	0.745	0.734	0.726	0.731	0.751	0.775	0.784	0.800	0.838	0.866
		0.021	0.018	0.019	0.013	0.011	0.009	0.008	0.003	0.008	0.009	0.014	0.015
4		0.703	0.617	0.576	0.567	0.575	0.578	0.591	0.633	0.674	0.721	0.807	0.749
		0.038	0.031	0.028	0.020	0.013	0.029	0.027	0.015	0.014	0.013	0.040	0.045
5		0.500	0.443	0.423	0.426	0.428	0.430	0.433	0.472	0.505	0.515	0.664	0.478
		0.042	0.009	0.007	0.008	0.009	0.008	0.014	0.018	0.015	0.016	0.048	0.047
6		0.673	0.664	0.634	0.636	0.661	0.654	0.686	0.729	0.745	0.763	0.837	0.866
		0.025	0.018	0.009	0.015	0.008	0.022	0.014	0.017	0.009	0.010	0.011	0.008
7		0.535	0.521	0.481	0.473	0.500	0.496	0.524	0.561	0.567	0.582	0.802	0.832
		0.023	0.013	0.012	0.013	0.013	0.019	0.016	0.016	0.009	0.019	0.014	0.009
8		0.687	0.597	0.554	0.545	0.552	0.551	0.582	0.609	0.656	0.708	0.819	0.746
		0.051	0.033	0.025	0.015	0.024	0.027	0.032	0.021	0.016	0.019	0.027	0.057
9		0.678	0.678	0.628	0.641	0.651	0.655	0.689	0.739	0.751	0.768	0.833	0.863
		0.030	0.022	0.011	0.013	0.025	0.024	0.012	0.014	0.008	0.006	0.008	0.008

Table A.5: Measured transition end positions $(x/c)_{\mathrm{tr,end}}$ for cases in Tab. A.1. *top*: mean value; *bottom*: standard deviation

r/R	0.42	0.48	0.53	0.57	0.63	0.66	0.72	0.77	0.82	0.88	0.94	0.97
r, m	0.270	0.310	0.343	0.370	0.410	0.430	0.470	0.500	0.530	0.570	0.610	0.630
1	0.905	0.894	0.886	0.892	0.888	0.887	0.895	0.893	0.898	0.878	0.915	0.886
	0.015	0.007	0.004	0.004	0.002	0.002	0.003	0.007	0.005	0.016	0.043	0.019
2	0.894	0.852	0.839	0.854	0.845	0.850	0.864	0.860	0.872	0.881	0.907	0.891
	0.008	0.014	0.015	0.004	0.006	0.008	0.002	0.006	0.003	0.003	0.026	0.014
3	0.864	0.810	0.800	0.812	0.801	0.808	0.819	0.828	0.840	0.859	0.897	0.886
	0.022	0.022	0.031	0.006	0.006	0.008	0.004	0.007	0.013	0.005	0.034	0.030
4	0.742	0.667	0.635	0.645	0.664	0.654	0.676	0.715	0.755	0.805	0.851	0.776
	0.043	0.055	0.050	0.032	0.026	0.048	0.039	0.034	0.032	0.024	0.060	0.051
5	0.532	0.513	0.499	0.498	0.507	0.513	0.517	0.559	0.583	0.608	0.690	0.506
	0.047	0.011	0.009	0.004	0.008	0.009	0.034	0.025	0.030	0.036	0.051	0.050
6	0.712	0.733	0.715	0.713	0.738	0.730	0.763	0.793	0.812	0.828	0.925	0.926
	0.035	0.038	0.009	0.021	0.014	0.030	0.008	0.021	0.010	0.006	0.045	0.018
7	0.583	0.595	0.565	0.548	0.569	0.565	0.592	0.631	0.643	0.660	0.863	0.875
	0.039	0.025	0.010	0.011	0.013	0.013	0.018	0.012	0.016	0.022	0.007	0.010
8	0.720	0.654	0.621	0.621	0.631	0.617	0.659	0.690	0.719	0.778	0.850	0.772
	0.052	0.058	0.042	0.040	0.038	0.050	0.037	0.045	0.042	0.036	0.032	0.065
9	0.732	0.745	0.717	0.729	0.728	0.735	0.770	0.803	0.819	0.832	0.888	0.919
	0.043	0.034	0.011	0.010	0.037	0.032	0.006	0.007	0.007	0.006	0.025	0.036

References

[1] J. D. Anderson. *Fundamentals of Aerodynamics*. McGraw-Hill, 2007. ISBN 978-0-071-25408-3.

[2] D. Arnal. Laminar-turbulent transition problems in supersonic and hypersonic flows. In *Special Course on Aerothermodynamics of Hypersonic Vehicles*, number AGARD-R-761, chapter 8, pages 8–1 – 8–45. AGARD, 1989. presented at VKI in Rhode-Saint-Genèse, Belgium, May 30 - June 3, 1988.

[3] D. Arnal. Boundary layer transition: Predictions based on linear theory. In *Special Course on Progress in Transition Modelling*, number AGARD-R-793, chapter 2, pages 2–1 – 2–63. AGARD, 1994. presented at VKI in Rhode-Saint-Genèse, Belgium, March 29 - April 1.

[4] D. Arnal and O. Vermeersch. Compressibility effects on laminar-turbulent boundary layer transition. *International Journal of Engineering Systems Modelling and Simulation*, 3(1-2):26–35, 2011. doi: 10.1504/IJESMS.2011.038747.

[5] P. Ashill, C. Betts, and I. Gaudet. A wind tunnel study of transition flows on a swept panel wing at high subsonic speeds. In *CEAS 2nd European Forum on Laminar Flow Technology*, pages 10.1–10.17, Bordeaux, France, June 10-12 1996.

[6] D. T. Balch and J. Lombardi. Experimental study of main rotor tip geometry and tail rotor interaction in hover. Vol I - Text and figures. Contractor Report 177336, NASA, February 1985.

[7] W. H. H. Banks and G. E. Gadd. Delaying effect of rotation on laminar separation. *AIAA Journal*, 1 (4):941–942, 1963. doi: 10.2514/3.1687.

[8] R. M. Bass. Small scale wind tunnel testing of model propellers. In *24th Aerospace and Sciences Meeting*, Reno, NV, USA, January 6-9 1986. doi: 10.2514/6.1986-392.

[9] P. Beaumier, C. Castellin, and G. Arnau. Performance prediction and flowfield analysis of rotors in hover, using a coupled Euler/ boundary layer method. *Aerospace Science and Technology*, 3(8): 473–484, 1999. doi: 10.1016/S1270-9638(99)00106-6.

[10] B. J. Bellhouse and D. L. Schultz. Determination of skin friction, separation and transition with a thin film-heated element. *Journal of Fluid Mechanics*, 24(2):379–400, 1966. doi: 10.1017/ S0022112066000715.

[11] T. Bencic. Rotating pressure measurements on a scale model high-by-pass ratio fan using PSP at NASA LeRC. In *Proceedings of the 5th Annual Pressure Sensitive Paint Workshop*, Tullahoma, TN, USA, May 14-16 1997.

[12] G. Bickel, G. Häusler, and M. Maul. Triangulation with expanded range of depth. *Optical Engineering*, 24(6):975–977, 1985. doi: 10.1117/12.7973610.

[13] D. A. Blaser and H. R. Velkoff. A preliminary analytical and experimental investigatin of helicopter rotor boundary layers. *AIAA Journal*, 11(12):1660–1664, 1973. doi: 10.2514/3.50666.

[14] A. Carpenter, W. Saric, and H. Reed. Laminar flow control on a swept wing with distributed roughness. In *26th AIAA Applied Aerodynamics Conference*, Honolulu, HI, USA, August 18-21 2008. doi: 10.2514/6.2008-7335.

[15] J. G. Coder. Enhancement of the amplification factor transport transition modeling framework. In *55th AIAA Aerospace Sciences Meeting*, number AIAA 2017-1709, Grapevine, TX, USA, January 9-13 2017. doi: 10.2514/6.2017-1709.

[16] J. G. Coder and M. D. Maughmer. Computational fluid dynamics compatible transition modeling using an amplification factor transport equation. *AIAA Journal*, 52(11):2506–2512, 2014. doi: 10.2514/1.J052905.

[17] M. Costantini, U. Fey, U. Henne, and C. Klein. Nonadiabatic surface effects on transition measurements using temperature-sensitive paints. *AIAA Journal*, 53(5):1172–1187, 2015. doi: 10.2514/1.J053155.

[18] X. Dechamps and S. Hein. Extension of the PSE code NOLOT for transition analysis in rotating reference frames. In A. Dillmann, G. Heller, E. Krämer, C. Wagner, S. Bansmer, R. Radespiel, and R. Semaan, editors, *New Results in Numerical and Experimental Fluid Mechanics XI*, pages 179–188, Cham, 2018. Springer International Publishing. ISBN 978-3-319-64519-3. doi: 10.1007/978-3-319-64519-3_16.

[19] P. Dini. *A Computational Efficient Model of Laminar Separation Bubbles*. PhD thesis, Pennsylvania State University, Department of Aerospace Engineering, University Park, PA, USA, 1990.

[20] P. Dini, M. S. Selig, and M. D. Maughmer. Simplified linear stability transition prediction method for separated boundary layers. *AIAA Journal*, 30(8):1953–1961, August 1992. doi: 10.2514/3.11165.

[21] K. J. Disotell, D. Peng, T. J. Juliano, J. W. Gregory, J. W. Crafton, and N. M. Komerath. Single-shot temperature- and pressure-sensitive paint measurements on an unsteady helicopter blade. *Experiments in Fluids*, 55(2):1671, 2014. doi: 10.1007/s00348-014-1671-2.

[22] A. V. Dovgal, V. V. Kozlov, and A. Michalke. Laminar boundary layer separation: Instability and associated phenomena. *Progress in Aerospace Sciences*, 30(1):61–94, 1994. doi: 10.1016/0376-0421(94)90003-5.

[23] M. Drela. *Two-dimensional transonic aerodynamic design and analysis using the Euler equations*. PhD thesis, Massachusetts Institute of Technology, Dept. of Aeronautics and Astronautics, 1986. URL http://hdl.handle.net/1721.1/14974.

[24] M. Drela. Newton solution of coupled viscous/inviscid multielement airfoil flows. In *21st Fluid Dynamics, Plasma Dynamics and Lasers Conference*, Seattle, WA, USA, June 18-20 1990. doi: 10.2514/6.1990-1470.

[25] M. Drela. A user's guide to MSES 3.05. User guide, Massachusetts Institute of Technology, Cambridge, MA, 2007. URL http://web.mit.edu/drela/Public/web/mses/mses.pdf.

[26] M. Drela and M. B. Giles. Viscous-inviscid analysis of transonic and low Reynolds number airfoils. *AIAA Journal*, 25(10):1347–1355, 1987. doi: 10.2514/3.9789.

[27] Z. Du and M. S. Selig. The effect of rotation on the boundary layer of a wind turbine blade. *Renewable Energy*, 20(2):167–181, 2000. doi: 10.1016/S0960-1481(99)00109-3.

[28] H. Dumitrescu and V. Cardos. Rotational effects on the boundary-layer flow in wind turbines. *AIAA Journal*, 42(2):408–411, 2003. doi: 10.2514/1.9103.

[29] H. A. Dwyer and W. J. McCroskey. Crossflow and unsteady boundary-layer effects on rotating blades. *AIAA Journal*, 9(8):1498–1505, 1971. doi: 10.2514/3.49952.

[30] E. R. G. Eckert. Survey on heat transfer at high speeds. Technical Report ARL 189, Aeronautical Research Laboratory, US Air Force, April 1962.

[31] E. R. G. Eckert and R. M. J. Drake. *Heat and Mass Transfer*. McGraw-Hill, New York, 2nd edition, 1959. ISBN 978-0-070-18924-9.

[32] H. W. Emmons. The laminar-turbulent transition in a boundary layer-part I. *Journal of the Aeronautical Sciences*, 18(7):490–498, 1951. doi: 10.2514/8.2010.

[33] R. H. Engler, K. Hartmann, and B. Schulze. Aerodynamic assessment of an optical pressure measurement system (OPMS) by comparison with conventional pressure measurements in a high speed wind tunnel. In *ICIASF '91 Record. International Congress on Instrumentation in Aerospace Simulation Facilities*, pages 17–24, Rockville, MD, USA, October 27-31 1991. doi: 10.1109/ICIASF.1991.186220.

[34] V. M. Falkner and S. W. Skan. Some approximate solution of the boundary layer equations. *Philosophical Magazine*, 12:865–896, 1931.

[35] F. F. Felker, M. D. Maisel, and M. D. Betzina. Full scale tilt rotor hover performance. In *41st Annual Forum of the American Helicopter Society*, Ft. Worth, TX, USA, May 15-17 1985.

[36] U. Fey and Y. Egami. *Transition Detection by Temperature-Sensitive Paint*, chapter 7.4, pages 537–552. Springer Handbook of Experimental Fluid Mechanics. Springer-Verlag Berlin Heidelberg, 2007.

[37] D. F. Fisher and N. S. Dougherty Jr. In-flight transition measurement on a $10°$ cone at Mach numbers from 0.5 to 2.0. Technical Report NASA TP 1971, NASA, June 1982.

[38] L. E. Fogarty. The laminar boundary layer on a rotating blade. *Journal of the Aeronautical Sciences*, 17(4):247–252, 1951. doi: 10.2514/8.1921.

[39] A. D. Gardner and K. Richter. Boundary layer transition determination for periodic and static flows using phase-averaged pressure data. *Experiments in Fluids*, 56(6):119, 2015. doi: 10.1007/s00348-015-1992-9.

[40] A. D. Gardner, C. C. Wolf, and M. Raffel. A new method of dynamic and static stall detection using infrared thermography. *Experiments in Fluids*, 57(9):149, 2016. doi: 10.1007/s00348-016-2235-4.

[41] R. Geisler. A fast double shutter system for CCD image sensors. *Measurement Science and Technology*, 25(2):025404, 2014. doi: 10.1088/0957-0233/25/2/025404.

[42] R. Geisler. A fast double shutter for CCD-based metrology. In H. Shiraga and T. G. Etoh, editors, *Selected Papers from the 31st International Congress on High-Speed Imaging and Photonics*, volume 10328, page 1032809, Osaka, Japan, 2017. SPIE. doi: 10.1117/12.2269099. event on November 7-10, 2016.

[43] R. Geisler. A fast multiple shutter for luminescence lifetime imaging. *Measurement Science and Technology*, 28(9):095403, 2017. doi: 10.1088/1361-6501/aa7aca.

[44] M. B. Giles and M. Drela. A two-dimensional transonic aerodynamic design method. *AIAA Journal*, 25(9):1199–1206, September 1987. doi: 10.2514/3.9768.

[45] M. B. Giles, M. Drela, and W. T. Thompson. Newton solution of direct and inverse transonic Euler equations. In *7th Computational Physics Conference*, number 85-1530, Cincinnati, OH, USA, July 15-17 1985. doi: 10.2514/6.1985-1530.

[46] C. Gleyzes, J. Cousteix, and J. L. Bonnet. *A Calculation Method of Leading Edge Separation Bubbles*, volume II of *Numerical and Physical Aspects of Aerodynamic Flows*, chapter 8, pages 173–192. Springer-Verlag Berlin Heidelberg, 1984. doi: 10.1007/978-3-662-09014-5_10.

[47] P. S. Granville. The calculation of viscous drag of bodies of revolution. Technical Report 849, Navy Department. The David W. Taylor Model Basin, Washington D.C., July 1953.

[48] W. Gray. The nature of the boundary layer flow at the nose of a swept wing. Technical Memorandum RAE TM Aero 256, RAE, 1952.

[49] J. W. Gregory. Porous pressure-sensitive paint for measurement of unsteady pressures in turbomachinery. In *42nd AIAA Aerospace Sciences Meeting and Exhibit*, number AIAA 2004-294, Reno, NV, USA, January 5-8 2004. doi: 10.2514/6.2004-294.

[50] J. W. Gregory, P. Kumar, D. Peng, S. Fonov, J. Crafton, and T. Liu. Integrated optical measurement techniques for investigation of fluid-structure interactions. In *39th AIAA Fluid Dynamics Conference*, number AIAA 2009-4044, San Antonio, TX, USA, June 22-25 2009. doi: 10.2514/6.2009-4044.

[51] J. W. Gregory, K. J. Disotell, D. Peng, T. J. Juliano, J. Crafton, and N. M. Komerath. Inverse methods for deblurring pressure-sensitive paint images of rotating surfaces. *AIAA Journal*, 52(9):2045–2061, April 2014. doi: 10.2514/1.J052793.

[52] J. W. Gregory, H. Sakaue, T. Liu, and J. P. Sullivan. Fast pressure-sensitive paint for flow and acoustic diagnostics. *Annual Review of Fluid Mechanics*, 46(1):303–330, 2014. doi: 10.1146/annurev-fluid-010313-141304.

[53] S. Hein, F. Bertolotti, M. Simen, A. Hanifi, and D. Henningson. Linear non-local instability analysis - the linear NOLOT code. Technical Report DLR IB 223-94, German Aerospace Center, 1995.

[54] J. T. Heineck, E. Schülein, and M. Raffel. Boundary layer transition detection on a rotor blade using rotating mirror thermography. In *Fifth Decennial AHS Aeromechanics Specialists' Conference*, San Francisco, CA, USA, January 22-24 2014.

[55] C. Heister. Laminar-turbulent transition prediction for helicopter rotors in hover and forward flight - a RANS based investigation of transition mechanisms using empirical criteria. In *38th European Rotorcraft Forum*, Amsterdam, Netherlands, September 4-7 2012. URL `http://hdl.handle.net/20.500.11881/667`.

[56] C. C. Heister. Numerical investigation of laminar-turbulent transition modeling methods in rotorcraft simulations. In *American Helicopter Society 69th Annual Forum*, Phoenix, AZ, USA, May 21-23 2013.

[57] C. C. Heister. *Methodik zur näherungsweisen Vorhersage des laminar-turbulenten Umschlags an Hubschrauberrotoren*. Dissertation, Universität Stuttgart, 2016. In German.

[58] *Infrared Emitters for Industrial Processes*. Heraeus. URL `https://apps.heraeus.com/IR_Products_EN/mobile/index.html#p=4`.

[59] H. Himmelskamp. *Profile investigations on a rotating airscrew*, volume 832 of *Reports and translations / MAP Völkenrode*. MAP, September 1947. Translated from "Profiluntersuchungen an einem umlaufenden Propeller", Dissertation, Göttingen, 1945; Mitt. Max-Planck-Institut für Strömungsforschung Göttingen Nr. 2, 1950.

[60] J. L. v. Ingen. A suggested semi-empirical method for the calculation of the boundary layer transition region. Technical Report VTH-74, TU Delft, Delft, September 1956.

[61] J. L. v. Ingen. The e^n method for transition prediction. historical review of work at TU Delft. In *38th Fluid Dynamics Conference and Exhibit*, number AIAA 2008-3830, Seattle, WA, USA, June 23-26 2008. doi: 10.2514/6.2008-3830.

[62] R. Jain. CFD performance and turbulence transition predictions on an installed model-scale rotor in hover. In *55th AIAA Aerospace Sciences Meeting*, number AIAA 2017-1871, Grapevine, TX, USA, January 9-13 2017. doi: 10.2514/6.2017-1871.

[63] T. J. Juliano, P. Kumar, D. Peng, J. W. Gregory, J. Crafton, and S. Fonov. Single-shot, lifetime-based pressure-sensitive paint for rotating blades. *Measurement Science and Technology*, 22(8):085403, 2011. doi: 10.1088/0957-0233/22/8/085403.

[64] T. J. Juliano, K. J. Disotell, J. W. Gregory, J. Crafton, and S. Fonov. Motion-deblurred, fast-response pressure-sensitive paint on a rotor in forward flight. *Measurement Science and Technology*, 23(4): 045303, 2012. doi: 10.1088/0957-0233/23/4/045303.

[65] Y. S. Kachanov. Physical mechanisms of laminar-boundary-layer transition. *Annual Review of Fluid Mechanics*, 26(1):411–482, 1994. doi: 10.1146/annurev.fl.26.010194.002211.

[66] Y. S. Kachanov, V. V. Kozlov, and V. Y. Levchenko. Beginning of turbulence in boundary layers. Technical report, Nauka, Siberian Div., Novosibirsk, 1982. 152 pages (in Russian).

[67] H. Kautsky and A. Hirsch. Nachweis geringster Sauerstoffmengen durch Phosphoreszenztilgung. *Zeitschrift füer anorganische und allgemeine Chemie*, 222:126–134, 1935. URL `https://onlinelibrary.wiley.com/doi/pdf/10.1002/zaac.19352220203`.

[68] C. Klein. *Einsatz einer druckempfindlichen Beschichtung (PSP) zur Bestimmung des momentanen Druckfeldes von Modellen im Windkanal*. Dissertation, Georg-August-Universität zu Göttingen, 1997. In German.

[69] C. Klein, R. H. Engler, U. Henne, and W. E. Sachs. Application of pressure-sensitive paint for determination of the pressure field and calculation of the forces and moments of models in a wind tunnel. *Experiments in Fluids*, 39(2):475–483, 2005. doi: 10.1007/s00348-005-1010-8.

[70] C. Klein, U. Henne, W. Sachs, S. Hock, N. Falk, U. Beifuss, V. Ondrus, and S. Schaber. Pressure measurement on rotating propeller blades by means of the pressure-sensitive paint lifetime method. In *51st AIAA Aerospace Sciences Meeting including the New Horizons Forum and Aerospace Exposition*, number AIAA 2013-0483, Grapevine, TX, USA, January 7-10 2013. doi: 10.2514/6.2013-483.

[71] Y. Kohama. Study on boundary layer transition of a rotating disk. *Acta Mechanica*, 50(3-4):193–199, September 1984. doi: 10.1007/BF01170959.

[72] H.-P. Kreplin and G. Höhler. Application of the surface hot film technique for laminar flow investigations. In *First European Forum on Laminar Flow Technology*, number 92-01-017, pages 123–131, Hamburg, Germany, March 16-18 1992.

[73] N. Krimmelbein. *Industrialization of the Automatic Transition Prediction in the DLR TAU Code*, pages 89–98. Springer Berlin Heidelberg, Berlin, Heidelberg, 2013. ISBN 978-3-642-38877-4. doi: 10.1007/978-3-642-38877-4_7.

[74] N. Krimmelbein and R. Radespiel. Transition prediction for three-dimensional flows using parallel computation. *Computers & Fluids*, 38(1):121–136, January 2009. doi: 10.1016/j.compfluid.2008. 01.004.

[75] A. Krumbein, N. Krimmelbein, and G. Schrauf. Automatic transition prediction in a hybrid flow solver - part 1: Methodology and sensitivities. *Journal of Aircraft*, 46(4):1176–1190, 2009. doi: 10.2514/1.39736.

[76] M. Lang, U. Rist, and S. Wagner. Investigation on disturbance amplification in a laminar separation bubble by means of LDA and PIV. In *Proceedings of the 11th Symposium on Applied Laser Technology to Fluid Dynamics*, Lisbon, Portugal, July 8-11 2002.

[77] W. Lang, A. D. Gardner, S. Mariappan, C. Klein, and M. Raffel. Boundary-layer transition on a rotor blade measured by temperature-sensitive paint, thermal imaging and image derotation. *Experiments in Fluids*, 56(6):118, 2015. doi: 10.1007/s00348-015-1988-5.

[78] R. B. Langtry and F. R. Menter. Correlation-based transition modeling for unstructured parallelized computational fluid dynamics codes. *AIAA Journal*, 47(12):2894–2906, 2009. doi: 10.2514/1.42362.

[79] J. G. Leishman. *Principles of Helicopter Aerodynamics*. Cambridge University Press, 2006. ISBN 978-1-107-01335-3.

[80] D. Lentink and M. H. Dickinson. Biofluiddynamic scaling of flapping, spinning and translating fins and wings. *Journal of Experimental Biology*, 212:2691–2704, 2009. doi: 10.1242/jeb.022251.

[81] J. Letzgus, M. Keßler, and E. Krämer. CFD-simulation of three-dimensional dynamic stall on a rotor with cyclic pitch control. In *41th European Rotorcraft Forum 2015*, Munich, Germany, September 1-4 2016.

[82] T. L. Lewis and R. D. Banner. Boundary layer transition detection on the X-15 vertical fin using surface pressure fluctuation measurements. Technical Report NASA-TM-X-2466, NASA, 1971. URL https://ntrs.nasa.gov/search.jsp?R=19720005345.

[83] H. W. Liepmann. Investigations on laminar boundary-layer stability and transition on curved boundaries. Technical Report NACA Wartime Report W-107, NACA, August 1943.

[84] S.-W. Liu. The laminar boundary-layer flow on rotating cylinders. Technical Report TN 57-298, Air Force Office of Scientific Research, June 1957. Part I (Flat Plate) and II (Thin Cylinders).

[85] T. Liu and J. P. Sullivan. *Pressure and Temperature Sensitive Paints*. Springer-Verlag Berlin Heidelberg, 2005. doi: 10.1007/b137841.

[86] T. Liu and S. Woodiga. Feasibility of global skin friction diagnostics using temperature sensitive paint. *Measurement Science and Technology*, 22(11):115402, 2011. doi: 10.1088/0957-0233/22/11/115402.

[87] T. Liu, T. Misaka, K. Asai, S. Obayashi, and J.-Z. Wu. Feasibility of skin-friction diagnostics based on surface pressure gradient field. *Measurement Science and Technology*, 27(12):125304, 2016. doi: 10.1088/0957-0233/27/12/125304.

[88] P. F. Lorber and F. O. Carta. Airfoil dynamic stall at constant pitch rate and high Reynolds number. *Journal of Aircraft*, 25(6):548–556, 1988. doi: 10.2514/3.45621.

[89] P. F. Lorber, R. C. Stauter, and A. J. Landgrebe. A comprehensive hover test of the airloads and airflow of an extensively instrumented model helicopter rotor. In *45th Annual Forum of the American Helicopter Society*, Boston, MA, USA, May 22-24 1989.

[90] T. Lutz. *Berechnung und Optimierung subsonisch umströmter Profile und Rotationskörper*, volume 7 of *Fortschritt-Berichte VDI*. VDI Verlag GmbH Düsseldorf, 2000. Dissertation, Universität Stuttgart.

[91] L. M. Mack. Linear stability and the problem of supersonic boundary layer transition. *AIAA Journal*, 13(3):278–289, 1975. doi: 10.2514/3.49693.

[92] L. M. Mack. Transition prediction and linear stability theory. In *AGARD Laminar-Turbulent Transition*, number AGARD-CP-224, pages 1.1–1.22, Lyngby, Denmark, May 2-4 1977.

[93] L. M. Mack. Boundary-layer linear stability theory. In *Special Course on Stability and Transition of Laminar Flow*, number AGARD-R-709, chapter 3, pages 3–1 – 3–81. AGARD, Neuilly sur Seine, France, 1984. Presented at VKI in Rhode-Saint-Genèse, Belgium, March 26-30.

[94] R. Mahalingam, O. Wong, and N. Komerath. Experiments on the origin of tip-vortices. In *38th Aerospace Sciences Meeting and Exhibit*, Reno, NV, USA, January 10-13 2000. doi: 10.2514/6. 2000-278.

[95] G. G. Martinez Hernandez, J. N. Sørensen, and W. Z. Shen. *Laminar-Turbulent Transition on Wind Turbines*. PhD thesis, Technical University of Denmark, Kgs. Lyngby, 2012.

[96] W. J. McCroskey. Measurements of boundary layer transition, separation and streamline direction on rotating blades. Technical Report TN D-6321, NASA, May 1971.

[97] W. J. McCroskey and P. F. Yaggy. Laminar boundary layers on helicopter rotors in forward flight. *AIAA Journal*, 6(10):1919–1926, 1968. doi: 10.2514/3.4901.

[98] B. McLachlan and J. Bell. Pressure-sensitive paint in aerodynamic testing. *Experimental Thermal and Fluid Science*, 10(4):470 – 485, 1995. doi: 10.1016/0894-1777(94)00123-P.

[99] Y. Mebarki and A. Benmeddour. Pressure-sensitive paint measurements on a moving store in the NRC 1.5 m blowdown wind tunnel. In *32nd AIAA Aerodynamic Measurement Technology and Ground Testing Conference*, AIAA 2016-4161, Washington, DC, USA, June 13-17 2016. doi: 10.2514/6.2016-4161.

[100] M. Miozzi, A. Capone, F. Di Felice, C. Klein, and T. Liu. Global and local skin friction diagnostics from TSP surface patterns on an underwater cylinder in crossflow. *Physics of Fluids*, 28(12):124101, 2016. doi: 10.1063/1.4968525.

[101] M. V. Morkovin. Critical evaluation of transition from laminar to turbulent shear layer with emphasis of hypersonic travelling bodies. Technical Report 68-149, AFFDL, 1968.

[102] M. V. Morkovin. *Bypass-Transition Research: Issues and Philosophy*, volume 16, pages 3–30. Springer Netherlands, Dordrecht, 1993. ISBN 978-94-011-1743-2. doi: 10.1007/ 978-94-011-1743-2_1.

[103] C. J. Obara and B. J. Holmes. Flight-measured laminar boundary-layer transition phenomena including stability theory analysis. Technical Report NASA-TP-2417, NASA, Hampton, VA, USA, April 1985.

[104] W. M. Orr. The stability or instability of the steady motions of a perfect liquid and of a viscous liquid. *Proceedings of the Royal Irish Academy. Section A: Mathematical and Physical Sciences*, 27:9–68, 1907-1909.

[105] A. D. Overmeyer and P. B. Martin. Measured boundary layer transition and rotor hover performance at model scale. In *55th AIAA Aerospace Sciences Meeting*, Grapevine, TX, USA, January 9-13 2017. doi: 10.2514/6.2017-1872.

[106] A. D. Overmeyer and P. B. Martin. The effect of laminar flow on rotor hover performance. In *AHS 73rd Annual Forum*, Fort Worth, TX, USA, May 9-11 2017.

[107] F. K. Owen. Transition experiments on a flat plate at subsonic and supersonic speeds. *AIAA Journal*, 8(3):518–523, 1970. doi: 10.2514/3.5699.

[108] F. K. Owen and C. C. Horstman. Hypersonic transitional boundary layers. *AIAA Journal*, 10(6): 769–775, June 1972. doi: 10.2514/3.50209.

[109] A. Pandey, J. W. Gregory, S. Stanfield, and J. W. Crafton. Comparison of blur elimination techniques for PSP images of rotating surfaces. In *54th AIAA Aerospace Sciences Meeting*, AIAA 2016-2019, San Diego, CA, USA, January 4-8 2016. doi: 10.2514/6.2016-2019.

[110] D. J. Peake, A. J. Bowker, S. J. Lockyear, and F. Ellis. Non-obtrusive detection of transition region using an infra-red camera. In *AGARD Laminar-Turbulent Transition*, number AGARD-CP-224, Lyngby, Denmark, May 2-4 1977.

[111] D. Peng and Y. Liu. A grid-pattern PSP/TSP system for simultaneous pressure and temperature measurements. *Sensors and Actuators B: Chemical*, 222(Supplement C):141 – 150, 2016. doi: https://doi.org/10.1016/j.snb.2015.08.070.

[112] D. Peng, C. D. Jensen, T. J. Juliano, J. W. Gregory, J. Crafton, S. Palluconi, and T. Liu. Temperature-compensated fast pressure-sensitive paint. *AIAA Journal*, 51(10):2420–2431, 2013. doi: 10.2514/1.J052318.

[113] D. Peng, L. Jiao, Y. Yu, Y. Liu, T. Oshio, T. Kawakubo, and A. Yakushiji. Single-shot lifetime-based PSP and TSP measurements on turbocharger compressor blades. *Experiments in Fluids*, 58(9):127, 2017. doi: 10.1007/s00348-017-2416-9.

[114] A. V. Popov, R. M. Botez, and M. Labib. Transition point detection from the surface pressure distribution for controller design. *Journal of Aircraft*, 45(1):23–28, 2008. doi: 10.2514/1.31488.

[115] L. Prandtl. Über Flüssigkeitsbewegung bei sehr kleiner Reibung. In *3rd International Congress of Mathematicians (ICM)*, Heidelberg, Germany, August 8-13 1904. Engl. translation in NACA-TM-452.

[116] E. Puklin, B. Carlson, S. Gouin, C. Costin, E. Green, S. Ponomarev, H. Tanji, and M. Gouterman. Ideality of pressure-sensitive paint. i. platinum tetra(pentafluorophenyl)porphine in fluoroacrylic polymer. *Journal of Applied Polymer Science*, 77(13):2795–2804, 9 2000. ISSN 1097-4628. doi: 10.1002/1097-4628(20000923)77:13<2795::AID-APP1>3.0.CO;2-K.

[117] M. Raffel and J. T. Heineck. Mirror-based image derotation for aerodynamic rotor measurements. *AIAA Journal*, 52(6):1337–1341, 2014. doi: 10.2514/1.J052836.

[118] M. Raffel, F. De Gregorio, K. de Groot, O. Schneider, W. Sheng, G. Gibertini, and A. Seraudie. On the generation of a helicopter aerodynamic database. *The Aeronautical Journal*, 115(1164):103–112, 2011. doi: 10.1017/S0001924000005492.

[119] M. Raffel, A. D. Gardner, T. Schwermer, C. B. Merz, A. Weiss, J. Braukmann, and C. C. Wolf. Rotating blade stall maps measured by differential infrared thermography. *AIAA Journal*, 55(5): 1753–1756, 2017. doi: 10.2514/1.J055452.

[120] V. Raghav and N. Komerath. An exploration of radial flow on a rotating blade in retreating blade stall. *Journal of the American Helicopter Society*, 58(2):1–10, 2013. doi: 10.4050/JAHS.58.022005.

[121] K. Richter and E. Schülein. Boundary-layer transition measurements on hovering helicopter rotors by infrared thermography. *Experiments in Fluids*, 55(7):1755, 2014. doi: 10.1007/s00348-014-1755-z.

[122] K. Richter, E. Schülein, B. Ewers, J. Raddatz, and A. Klein. Boundary layer transition characteristics of a full-scale helicopter rotor in hover. In *AHS 72nd Annual Forum*, West Palm Beach, FL, USA, May 17-19 2016.

[123] U. Rist. Instability and transition mechanisms in laminar separation bubbles. VKI/RTO-LS, von Karman Institute for Fluid Dynamics, Rhode-Saint-Genese, Belgium, November 24-28 2003. URL https://www.iag.uni-stuttgart.de/mitarbeiter/ulrich_rist/Literaturverzeichnis/papers/VKI_URi_1.pdf.

[124] C. H. Rohardt. Flow visualization on a helicopter rotor in hover using acenaphthen. In *13th European Rotorcraft Forum*, Arles, France, September 8-11 1987.

[125] N. Rott and W. E. Smith. Some examples of laminar boundary-layer flow on rotating blades. *Journal of the Aeronautical Sciences*, 23(11):991–996, 1956. doi: 10.2514/8.3710.

[126] W. Ruyten and M. Sellers. Improved data processing for pressure-sensitive paint measurements in an industrial facility. In *44th AIAA Aerospace Sciences Meeting and Exhibit*, number AIAA 2006-1042, Reno, NV, USA, January 9-12 2006. doi: 10.2514/6.2006-1042.

[127] W. S. Saric. Physical description of boundary-layer transition: Experimental evidence. Technical Report AGARD-R-793, NATO AGARD, 1993.

[128] H. Schlichting. Berechnung der Anfachung kleiner Störungen bei der Plattenanströmung. *ZAMM - Zeitschrift für angewandte Mathematik und Mechanik*, 13, 1933.

[129] H. Schlichting and K. Gersten. *Boundary-Layer Theory*. Springer-Verlag Berlin Heidelberg, 9 edition, 2017. doi: 10.1007/978-3-662-52919-5.

[130] G. Schrauf. Die dreidimensionalen, kompressiblen Stördifferentialgleichungen bei nicht-paralleler grundströmung. Technical Report MBB TE 2-1616, MBB-ERNO, 1987.

[131] G. Schrauf. An efficient solver of the Eigenvalue problem of the linear stability equations for three dimensional, compressible boundary-layer flows. In *6. DGLR Fach-Symposium*, number 88-05, Braunschweig, Germany, November 8-10 1988.

[132] G. Schrauf. The three-dimensional, compressible, linear stability equations for boundary-layer flows along curved surfaces. Technical Report ELFIN 1, Deutsche Aerospace Airbus, 1990.

[133] G. Schrauf. COCO - a program to compute velocity and temperature profiles for local and nonlocal stability analysis of compresible, conical boundary layers with suction. Technical report, ZARM, 1998.

[134] G. Schrauf. LILO 2.1 - users guide and tutorial. Technical Report 6, GSSC, 2006.

[135] G. B. Schubauer and P. Klebanoff. Contributions on the mechanics of boundary-layer transition. Technical Report NACA-TR-1289, National Bureau of Standards, Washington, D. C., February 28 1956.

[136] G. B. Schubauer and H. K. Skramstad. Laminar boundary-layer oscillations and transition on a flat plate. *Journal of Research*, 38:251–292, February 1947. URL https://nvlpubs.nist.gov/nistpubs/jres/38/jresv38n2p251_A1b.pdf.

[137] E. Schülein. Experimental investigation of laminar flow control on a supersonic swept wing by suction. In *4th Flow Control Conference*, Seattle, WA, USA, June 23-26 2008. doi: 10.2514/6.2008-4208.

[138] E. Schülein. Optical method for skin-friction measurements on fast-rotating blades. *Experiments in Fluids*, 55(2):1672, 2014. doi: 10.1007/s00348-014-1672-1.

[139] D. Schwamborn, T. Gerhold, and R. Heinrich. The DLR TAU-code: Recent applications in research and industry. In *European Conference on Computational Fluid Dynamics. ECCOMAS CFD 2006*, Crete, Greece, June 5-10 2006.

[140] T. Schwarz and K. Pahlke. CFD code validation for complete hhelicopter - the european GOAHEAD project. In *American Helicopter Society 67th Annual Forum*, Virginia Beach, VA, USA, May 3-5 2011.

[141] T. Schwermer, K. Richter, and M. Raffel. Development of a rotor test facility for the investigation of dynamic stall. In A. Dillmann, G. Heller, E. Krämer, C. Wagner, and C. Breitsamter, editors, *New Results in Numerical and Experimental Fluid Mechanics X. Notes on Numerical Fluid Mechanics and Multidisciplinary Design*, volume 132, pages 663–673, Cham, 2016. Springer Int. Publishing. ISBN 978-3-319-27279-5. doi: 10.1007/978-3-319-27279-5_58.

[142] T. Schwermer, A. D. Gardner, and M. Raffel. Dynamic stall experiments on a rotor with high cyclic setting in axial inflow. In *AHS International's 73rd Annual Forum & Technology Display*, Fort Worth, TX, USA, Mai 9-11 2017.

[143] A. M. O. Smith and N. Gamberoni. Transition, pressure gradient and stability theory. Technical Report ES 26388, Douglas Aircraft Company, August 31 1956.

[144] M. J. Smith, T.-C. Wong, M. Potsdam, J. Baeder, and P. Sujee. Evaluation of CFD to determine two-dimensional airfoil characteristics for rotorcraft applications. In *AHS 60th Annual Forum*, Baltimore, MD, USA, June 7-10 2004.

[145] A. Sommerfeld. Ein Beitrag zur hydrodynamischen Erklärung der turbulenten Flüssigkeitsbewegungen. In *4th International Congress of Mathematicians (ICM)*, Rome, Italy, April 6-11 1908.

[146] H. B. Squire. On the stability for three-dimensional disturbances of viscous fluid flow between parallel walls. In *Proceedings of the Royal Society A. Mathematical, Physical and Engineering Sciences*, volume 142, November 1 1933.

[147] J. H. Stanfield and C. J. Betts. Transition detection technique in use in the DRA Bedford wind tunnels. In *Proceedings of the 7th International Symposium on Flow Visualization*, pages 929–934, Seattle, WA, USA, September 11-14 1995.

[148] A. Suryanarayanan, B. Ozturk, M. T. Schobeiri, and J. C. Han. Film-cooling effectiveness on a rotating turbine platform using pressure sensitive paint technique. *Journal of Turbomachinery*, 132 (4):041001–041001–13, Apr. 2010. doi: 10.1115/1.3142860.

[149] J. L. Tangler. Insight into wind turbine stall and post-stall aerodynamics. *Wind Energy*, 7:247–260, 2004. doi: 10.1002/we.122.

[150] L. H. Tanner and L. G. Blows. A study of the motion of oil film on surface in air flow, with application to the measurement of skin friction. *Journal of Physics E: Scientific Intruments*, 9(3):194–202, 1976. doi: 10.1088/0022-3735/9/3/015.

[151] W. H. Tanner and P. F. Yaggy. Experimental boundary layer study on hovering rotors. *Journal of the American Helicopter Society*, 11(13):22–37, 1966. doi: 10.4050/JAHS.11.22.

[152] W. Tollmien. Über die Entstehung der Turbulenz. *Nachrichten von der Gesellschaft der Wissenschaften zu Göttingen, Mathematisch-Physikalische Klasse*, pages 21–44, March 1929. Engl. translation in NACA-TM-609 (1931).

[153] C. Tropea, A. L. Yarin, and J. F. Foss, editors. *Springer Handbook of Experimental Fluid Mechanics*, chapter Temperature, Concentration and Heat Flux. Springer, New York, 2007.

[154] C. Tung and L. Branum. Model tilt-rotor hover performance and surface pressure measurement. In *46th Annual Forum of the American Helicopter Society*, Washington, DC, USA, May 21-23 1990.

[155] B. F. A. van Hest. *Laminar-turbulent transition in boundary layers with adverse pressure gradient*. PhD thesis, Delft University of Technology, 1996.

[156] H. R. Velkoff, D. A. Blaser, and K. M. Jones. Boundary layer discontinuity on a helicopter rotor blade in hovering. *Journal of Aircraft*, 8(2):101–107, 1971. doi: 10.2514/3.44236.

[157] B. A. O. Vieira, M. P. Kinzel, and M. D. Maughmer. CFD hover prediction including boundary-layer transition. In *55th AIAA Aerospace Sciences Meeting*, Grapevine, TX, USA, January 9-13 2017. doi: 10.2514/6.2017-1665.

[158] A. Vollan and L. Alati. A new optical pressure measurement system (OPMS). In *ICIASF '91 Record. International Congress on Instrumentation in Aerospace Simulation Facilities*, pages 10–16, Rockville, MD, USA, October 27-31 1991. doi: 10.1109/ICIASF.1991.186220.

[159] A. Vuillet, M. Allongue, J. J. Philippe, and A. Desopper. Performance and aerodynamic development of the Super Puma MK II main rotor with new SPP 8 blade tip design. In *15th European Rotorcraft Forum*, Amsterdam, Netherlands, September 12-15 1989.

[160] A. J. Wadcock, G. K. Yamauchi, and D. M. Driver. Skin friction measurements on a hovering full-scale tilt rotor. *Journal of the American Helicopter Society*, 44(4):312–319, 1999. doi: 10.4050/JAHS.44.312.

[161] G. J. Walker and J. P. Gostelow. Effects of adverse pressure gradients on the nature and length of boundary layer transition. *Journal of Turbomachinery*, 112(2):196–205, 1990. doi: 10.1115/1.2927633.

[162] A. N. Watkins, B. D. Leighty, W. E. Lipford, K. Z. Goodman, J. Crafton, and J. W. Gregory. Measuring surface pressures on rotor blades using pressure-sensitive paint. *AIAA Journal*, 54(1):206–215, 2016. doi: 10.2514/1.J054191.

[163] N. A. Winslow, B. F. Carrol, and F. M. Setzer. Frequency response of pressure sensitive paints. In *27th AIAA Fluid Dynamics Conference*, number AIAA 96-1967, New Orleans, LA, USA, June 17-20 1996. doi: 10.2514/6.1996-1967.

[164] C. C. Wolf, C. B. Merz, K. Richter, and M. Raffel. Tip-vortex dynamics of a pitching rotor blade-tip model. *AIAA Journal*, 54(10):2947–2960, August 2016. doi: 10.2514/1.J054656.

[165] O. D. Wong, A. N. Watkins, and J. L. Ingram. Pressure sensitive paint measurements on 15% scale rotor blades in hover. In *35th AIAA Fluid Dynamics Conference and Exhibit*, AIAA 2005-5008, Toronto, ON, Canada, June 6-9 2005. doi: 10.2514/6.2005-5008.

[166] O. D. Wong, K. W. Noonan, A. N. Watkins, L. N. Jenkins, and C.-S. Yao. Non-intrusive measurements of a four-bladed rotor in hover - a first look. In *AHS Aeromechanics Specialists' Conference*, San Francisco, CA, USA, January 20-22 2010.

[167] O. D. Wong, A. N. Watkins, K. Z. Goodman, J. Crafton, A. Forlines, L. Goss, J. W. Gregory, and T. J. Juliano. Blade tip pressure measurements using pressure sensitive paint. In *American Helicopter Society 68th Annual Forum*, Fort Worth, TX, USA, May 1-3 2012.

[168] W. Würz. *Hitzdrahtmessungen zum laminar-turbulenten Strömungsumschlag in anliegenden Grenzschichten und Ablöseblasen sowie Vergleich mit der linearen Stabilitätstheorie und empirischen Umschlagskriterien*. Dissertation, Universität Stuttgart, 1995. In German.

[169] G. K. Yamauchi and W. Johnson. Flow field analysis of a model prop rotor in hover. In *Proceedings of the 21st European Rotorcraft Forum*, St Petersburg, Russia, August 30 - September 1 1995.

[170] D. Yorita, K. Asai, C. Klein, U. Henne, and S. Schaber. Transition detection on rotating propeller blades by means of temperature sensitive paint. In *50th AIAA Aerospace Sciences Meeting Including the New Horizons Forum and Aerospace Exposition*, number AIAA 2012-1187, Grapevine, TX, USA, January 7-9 2012. doi: 10.2514/6.2012-1187.

[171] D. Yorita, U. Henne, and C. Klein. Improvement of lifetime-based PSP technique for industrial wind tunnel tests. In *55th AIAA Aerospace Sciences Meeting*, number AIAA 2017-0703, Grapevine, TX, USA, January 9-13 2017. doi: 10.2514/6.2017-0703.

[172] D. Yorita, A. Weiss, R. Geisler, U. Henne, and C. Klein. Comparison of LED and LASER based lifetime pressure-sensitive paint measurement techniques. In *2018 AIAA Aerospace Sciences Meeting*, number AIAA 2018-1029, Kissimmee, FL, USA, January 8-12 2018. doi: 10.2514/6.2018-1029.

Publications

Peer-reviewed publications

1. A. Weiss, A. D. Gardner, C. Klein, and M. Raffel. Boundary-layer transition measurements on Mach-scaled helicopter rotor blades in climb. *CEAS Aeronautical Journal*, 8(4):613–623, December 2017. doi: 10.1007/s13272-017-0263-2.

2. A. Weiss, R. Geisler, T. Schwermer, D. Yorita, U. Henne, C. Klein, and M. Raffel. Single-shot pressure-sensitive paint lifetime measurements on fast rotating blades using an optimized double-shutter technique. *Experiments in Fluids*, 58(9):120–140, August 2017. doi: 10.1007/s00348-017-2400-4.

3. M. Raffel, A. D. Gardner, T. Schwermer, C. B. Merz, A. Weiss, J. Braukmann, and C. C. Wolf. Rotating blade stall maps measured by differential infrared thermography. *AIAA Journal*, 55(5):1753–1756, 2017. doi: 10.2514/1.J055452.

4. H. Kroll, A. Weiss, and W. Nitsche. Experimental Investigation of Periodically Generated Vortex Rings in Crossflow Impinging on a Flat Plate. In A. Dillmann, G. Heller, E. Krämer, C. Wagner, and C. Breitsamter, editors, *New Results in Numerical and Experimental Fluid Mechanics X. Notes on Numerical Fluid Mechanics and Multidisciplinary Design*, volume 132, pages 639–649, Cham, 2016. Springer Int. Publishing. doi: 10.1007/978-3-319-27279-5_56.

Conference proceedings

1. V. Ondrus, M. Hilfer, U. Henne, M. Costantini, A. Weiss, C. Klein, and U. Beifuss. Development of sensors for ambient temperature measurement. In *5th International Conference on Experimental Fluid Mechanics*, Munich, Germany, July 2-4 2018.

2. A. Weiss, A. D. Gardner, T. Schwermer, C. Klein, and M. Raffel. On the effect of rotational forces on rotor blade boundary-layer transition. In *2018 AIAA Aerospace Sciences Meeting*, number AIAA 2018-0309, Kissimmee, FL, USA, January 8-12 2018. doi: 10.2514/6.2018-0309, submitted to *AIAA Journal*.

3. D. Yorita, A. Weiss, R. Geisler, U. Henne, C. Klein. Comparison of LED and LASER based lifetime pressure-sensitive paint measurement techniques. In *2018 AIAA Aerospace Sciences Meeting*, number AIAA 2018-1029, Kissimmee, FL, USA, January 8-12 2018. doi: 10.2514/6.2018-1029.

4. A. Weiss, A. D. Gardner, and C. Klein. Boundary-layer transition measurements on Mach-scaled helicopter rotor blades in the rotating test facility Göttingen. In *17th ONERA-DLR Aerospace Symposium*, Aussois, France, June 7-9 2017.

5. M. Raffel, A. D. Gardner, T. Schwermer, C. B. Merz, A. Weiss, J. Braukmann, C. C. Wolf, and B. Ewers. Differential Infrared Thermography (DIT) for Dynamic Stall Detection. In *18th International Symposium on Applications of Laser Techniques to Fluid Mechanics*, Lisbon, Portugal, July 4-7 2016.

Curriculum vitae

Armin Weiss
Born on November 22nd 1986 in Sibiu (Hermannstadt), Romania
Armin.Weiss@dlr.de

SCIENTIFIC ACTIVITIES

Since 06/2014	Research associate at the Institute of Aerodynamics and Flow Technology, German Aerospace Center (DLR), Göttingen
06/2014-08/2018	Dissertation at Gottfried Wilhelm Leibniz University Hannover: "Investigations of boundary-layer transition and airloads on rotating blades"
09/2013-04/2014	Master thesis at the Institute for Aeronautics and Astronautics, Technical University Berlin (in German): "Characterization and dynamics of ring vortices in transverse flow and their interaction on a baffle plate"
03-08/2011	Bachelor thesis at Wind Tunnel Operations, Airbus Operations GmbH, Bremen: "Enhanced methodology for turbofan propulsion simulator calibration"

EDUCATION

10/2011-04/2014	M. Sc. in Aeronautics and Astronautics, Technical University Berlin
03-06/2013	Study visit and project work at *Lunds Tekniska Högskola (LTH), Division of Fluid Mechanics*, Lund, Sweden
09/2007-08/2011	B. Eng. in Aeronautical Engineering, dual study program, Hamburg University of Applied Sciences (HAW) and Airbus Operations GmbH
02-06/2010	Study visit at *École Supérieure des Technique Aéronautiques et de Construction Automobile (ESTACA)*, Paris, France
08/1997-07/2006	Abitur at *Gymnasium auf der Morgenröthe*, Siegen
08/2003-07/2004	High School Year at Homer Central High School, Homer, NY, USA

SCHOLARSHIPS AND AWARDS

Since 12/2012	Scholar at Airbus Operations GmbH
11/2008-04/2014	Scholar at *Studienstiftung des deutschen Volkes* (German National Academic Foundation)
02/2012	*Fritz Kirchberg Prize* of the 2011 graduates in the "B. Eng. in Aeronautical Engineering" degree program at HAW Hamburg for outstanding achievements